THE UNIVERSITY OF CHICAGO

UNCOVERING CELLULAR STRUCTURES AND DYNAMICS WITH QUANTITATIVE IMAGE ANALYSIS AND MODELING

A DISSERTATION SUBMITTED TO

THE FACULTY OF THE DIVISION OF THE PHYSICAL SCIENCES

AND

THE FACULTY OF THE DIVISION OF THE BIOLOGICAL SCIENCES

AND THE PRITZKER SCHOOL OF MEDICINE

IN CANDIDACY FOR THE DEGREE OF

DOCTOR OF PHILOSOPHY

GRADUATE PROGRAM IN BIOPHYSICAL SCIENCES

BY

ELIZABETH WHITE

CHICAGO, ILLINOIS

MARCH 2023

TABLE OF CONTENTS

LIST OF FIGURES

LIST OF TABLES

ACKNOWLEDGEMENTS

Throughout my PhD I have received incredible support from many people around me. First I have to thank my advisors, Ed Munro and Aaron Dinner for their unwavering support and guidance. The Biophysical Sciences Program administration, especially Michele Wittels and Adam Hammond were a constant source of encouragement and reassurance. I especially have to thank my family and friends who surrounded me and supported me through the highs and lows of my degree. To my collaborators, unofficial mentors, and sources of inspiration, thank you for your kindness and wisdom over the years.

ABSTRACT

Uncovering cellular structures and dynamics with quantitative image analysis and modeling

Fluorescence microscopy is a powerful method to observe cellular structures, functions, and processes. Image analysis can quantitatively characterize cellular structures and dynamics. In this work, I use different approaches to microscopy and image analysis to extract specific information of cellular structures and dynamics. I use this approach to explore two distinct topics. First, I study the cell cortex, which is an actin-rich layer directly beneath the plasma membrane of animal cells. The cortex exerts forces that control changes in cell shape, intracellular motion, and the movement of cells within their environments. I specifically examine how the expression of specific microscopic components of the cortex tune cortical flows in polarized one-cell *C. elegans* zygotes. I use TIRF microscopy combined with PIV and single particle tracking to characterize the microscopic components of the *C. elegans* cortex and macroscopic cortical flows, and I then use these measurements to tightly constrain agent-based simulations. These simulations successfully reproduce cortical flows characterized *in vivo* and accurately predict how cortical flows respond to perturbations of microscopic properties of the cortex. This work demonstrates that the components that I characterized are sufficient to generate macroscopic cortical flows and provides a platform for further studies. My second topic of study is extracellular vesicles (EVs), which are vesicles that are produced within cells, exported, and can then be taken up by other cells. The two primary classes of EVs are defined in terms of their origins: exosomes are derived from the endosomal pathway while microvesicles (ectosomes) bud from the cell membrane. However, it remains unclear whether the contents, sizes, and localizations of subpopulations of EVs can be used to associate them with the two primary classes. Most studies consider EVs after they have

been secreted, which makes it impossible to determine their origin with certainty. In contrast, I use confocal microscopy and high-resolution volumetric imaging to study intracellular localization of the EV markers CD9 and CD63 prior to EV export from cells. I observe spatially distinct populations of CD9 and CD63, which suggests that CD9 and CD63 can be used a biomarkers for the two primary classes of EVs. Interestingly, I also observe structures in which CD63 forms a shell that encapsulates CD9. These structures are likely multivesicular bodies (MVBs), from which CD9 and CD63 may be sorted differently. Put together, my studies show how microscopy, quantitative image analysis, and modeling can be combined to elucidate the microscopic origins of cellular phenomena.

CHAPTER 1

INTRODUCTION

1.1 Using the cell cortex to study actomyosin networks and the relationship between microscopic properties and macroscopic network behaviors

The cell cortex is a thin layer of actin, myosin, and crosslinkers that lies directly beneath the plasma membrane of animal cells[1]. The cortex produces forces that control changes in cell shape, intracellular motions, and the movement of cells within their environments[1,2]. Here I will focus on one class of movement called cortical flows, which are a common phenomenon across different organisms, cell types, and phases of the cell cycle[3]. They are critical for a variety of biological processes, such as cell motility and cell polarization. This thesis seeks to understand cortical flows in polarized *C. elegans* zygotes.

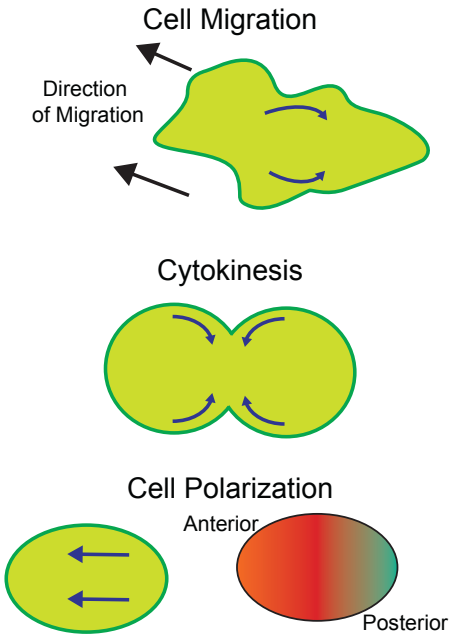

Figure 1.1: Cortical flows drive multiple cellular processes. Figure 1.1 Continued (pg. 2).

Figure 1.1 Continued. The cell cortex (dark green) is comprised of actin, myosin, and crosslinkers. Gradients in cortical tension drive cortical flows (dark blue arrows). Cortical flows drive cell motility, cytokinesis, and cell polarization. Adapted from Chugh and Paluch, "The actin cortex at a glance." *J Cell Sci*, 2018. [Ref 1]

Cortical flows drive a variety of cellular processes, including cell motility, cytokinesis, and cell polarization (see Figure 1.1). Adhesion-independent cell motility is a form of motility characterized by cortical flows[1,4,5]. Gradients of non-muscle myosin II drive these cortical flows to the rear of the cell, and the flows couple to external substrates through non-specific friction to propel the cell forward[4–8]. This is generally described as amoeboid-like motility and has been observed in a variety of cell types, including dendritic and cancer cells[5–7].

As mentioned above, another cellular phenomenon characterized by cortical flows is cell polarization. Cell polarization is critical for many processes, including asymmetric cell division, which generates diversity in daughter cells and establishes differentiated cell types[9]. One of the best examples of cortical flows in cell polarization is the single cell *C. elegans* zygote[10–12]. Immediately after fertilization, the *C. elegans* zygote undergoes symmetry breaking, which depends on non-muscle myosin II activity[12,13]. Next the zygote undergoes polarity establishment, during which cortical flows and pulsed contractions drive the redistribution of anterior PAR proteins (aPARs) and posterior PAR proteins (pPARs) to their respective poles[10,11,13]. During polarity maintenance, slow cortical flows directed to the anterior of the embryo enforce the asymmetric distribution of PAR proteins[13,14]. Next the cortical flows drive cytokinesis and the cell is asymmetrical divided into AB and P_1 daughter cells[12,13].

Cortical flows are critical throughout multiple stages in single-cell *C. elegans* development[10]. These flows are caused by anisotropies in cortical tension across the embryo[15] which are determined by spatial gradients of myosin II activity. During cytokinesis, cortical flows

contribute to aligning actin filaments to form a well-organized contractile ring[16]. Cortical flows are essential for polarization in many other systems, such as Drosophila neuroblast stem cells[17,18].

At macroscopic spatial scales (tens of microns) and long temporal scales (minutes or longer) cortical flows can often be described as driven by active cortical tension which is passively resisted by an effective viscosity[1,2,19]. Cortical flows are thought to emerge from microscopic interactions among actin filaments, crosslinkers, and motors[1,14]. Each component of the cortex can contribute to the cortical tension, the passive resistance, or both in complex ways.

Actin filaments are semi-flexible polymers of monomeric subunits[20]. Filaments have pointed and barbed ends, and elongation is significantly faster at the barbed end than the pointed[21]. The contractile cortex is primarily composed of long, unbranched actin filaments. Their assembly into contractile networks is controlled by assembly factors called formin, which promotes filament nucleation, and profilin, which promotes elongation[1,19]. Actin filament elongation occurs at a rate of 1-5 μm/s[22–24]. The lifetime of actin filaments varies across cell types, but it is on the scale of tens of seconds[19]. Capping proteins contribute to halting actin filament elongation, and cofilin promotes disassembly and severing of actin filaments[19,21,25]. In non-branched networks, a balance of formin, profilin, and cofilin work together to modulate actin assembly and density in cells[24]. Thus, actin filaments cannot be thought of as static fibers; actin filaments undergo constant assembly and disassembly. The turnover of actin filaments is critical for establishing flows in the cortex; the density of actin controls cortical thickness and is directly related to cortical tension, and the time scale of the turnover affects the viscous regime of the cortex[1,2,26,27]. Actin turnover therefore affects how force is propagated across the cortex and resistance to said forces.

There are a variety of crosslinkers found within the cortex, and each crosslinker's stiffness and binding/unbinding rates affect the architecture a crosslinker promotes. Some crosslinkers,

notably plastin and α-actinin, tightly bind actin filaments into bundles[1,28–30]. Other crosslinkers, such as filamin, promote the formation of networks in which filaments are more randomly oriented relative to one another[20,31]. When actin filaments are bundled together, they effectively become more rigid. Crosslinkers can contribute to stiffness in system, but they can also exert forces or aid in propagating force across actin filaments[2,28,32–34]. Furthermore, the timescale of the crosslinkers binding/unbinding rates can affect stress relaxation in the cortex[35].

Myosin motors are responsible for generating the majority of contractile forces in the cortex[1,2,36]. Myosin assembles into minifilaments with approximately tens of heads[19,36]. These myosin minifilaments process along, and exert force on, actin filaments. The speed of myosin varies between organisms, but it is generally one the order of several hundred nanometers per second[37,38]. Myosin exerts a stall force as it processes along the actin filaments; this stall force is proportional to the force a single head is able to exert and the number of myosin heads in the minifilament[19]. Additionally, myosin crosslinks actin filaments while processing along them[1].

One major question in the field is: how does microscopic control of actin filaments, crosslinkers, and motors lead to changes in macroscopic properties such as active tension or effective viscosity? Bridging the scale of microscopic properties to macroscopic behaviors presents some interesting questions. Cortical flows are on the scale of tens of microns while the molecular interactions that govern actin filament assembly/disassembly and crosslinking produce force very locally, at nanometer scales[1]. While cortical flows occur on the scale of minutes or longer, molecular interactions within the cortex happen at a much faster time scale. For instance, actin filaments have a lifetime on the scale of seconds to tens of seconds[1,2]. Similarly, myosin minifilaments undergo constant turnover on the scale of seconds, and crosslinkers constantly bind and unbind from actin filaments[2,19].

Here, I describe some general trends in the relationships between individual cortical components and the macroscopic view of the cortex. The myosin density and activity are largely responsible for the amount of active force in the system[1,2,19]. Cortical tension increases with myosin density and activity, while decreasing myosin density decreases cortical tension[1,2,19]. This was noted in bleb growth, in which decreasing the cortical tension decreased bleb size[39], and in cytokinesis[40], in which decreasing myosin activity decreases cortical flows immediately prior to cytokinesis.

The density of actin filaments and crosslinkers affects the effective resistance of the cortex. Increasing actin filament density decreases the mesh size of the cortex, and thus increases the stiffness[1,19]. The density of crosslinkers controls the level of bundling and connectivity in the network, which affects the effective rigidity of actin bundles and thus the overall the stiffness of the cortex[19,41]. Crosslinkers also play a role in force transmission, so depleting crosslinkers has a more complex effect than simply decreasing the overall stiffness. Several studies found that intermediate levels of connectivity of the cortex optimize rates of cortical flows. For instance, Tinevez *et al.* found that actin binding proteins that regulate actin turnover affect cortical tension and bleb size and growth dynamics[39]. Ding *et al.* found that decreasing plastin abundance decreases the overall velocity of cortical flows in *C. elegans* polarity establishment and increased random movements[28]. Both studies found that an intermediate level of connectivity, controlled by properties of actin or crosslinker density, optimize rates of cortical flow.

The components of the cortex undergo constant turnover which can affect viscoelastic properties and contraction dynamics in the cortex[1,2,19]. Increasing the turnover of crosslinkers or actin filaments can decrease the effective resistance of the cortex[1,2,19,42,43]. Additionally, spatial differences in turnover dynamics influence the macroscopic behaviors in a system. For instance,

in *Dictyostelium* cytokinesis, the turnover in the equator is slower than at the poles[44]. The effect of turnover of components on macroscopic properties is not yet fully understood, and an area of active investigation[1,19].

While there have been some foundational studies investigating the relationship between microscopic characteristics of the cell cortex and macroscopic behaviors, this is still an area of active research. Many studies investigating this use loss-of-function mutants to eliminate the function of specific cortex components[28,40]. However, the cortex is a complicated system and completely knocking out a protein may not reveal the intricacies of its role in producing cortical flows. For instance, the relationships between motor activity or crosslinker density and contractile tension is complex and non-linear. It is not enough to say that removing a crosslinker blocks force production or even that it reduces force production, because the relationship could be non-linear or even biphasic. The only way to assess this is to systematically assess how properties vary over a range of different levels of perturbations. Quantifying the strength of the perturbations is critical to truly understand the range of responses.

Cortical flows are a promising system to investigate the relationship between microscopic properties of the cortex and cell-wide behaviors. Microscopic interactions in the cortex drive cortical flows, and cortical flows produce observable cell-wide behaviors such as polarization or cell motility. Here, I use the polarized *C. elegans* zygote as a model system to investigate cortical flows. I specifically focus on polarity maintenance phase, during which there are coherent macroscopic flows from the posterior to anterior pole. There are several key advantages to using the *C. elegans* zygote as a model system. First, the *C. elegans* zygote is a single, large cell so it can be viewed in a single focal plane with high spatial and temporal resolution[10]. Second, the components of the cortex have been well characterized (see Figure 1.2), and it is easy to deplete

the expression of proteins using RNAi[45]. This allows me to perturb microscopic properties of the cortex (such as proteins regulating actin filament assembly and lifetime and crosslinkers) and directly observe the effects on cortical flows. This provides a useful way to investigate the relationship between microscopic properties of the cortex and macroscopic behaviors.

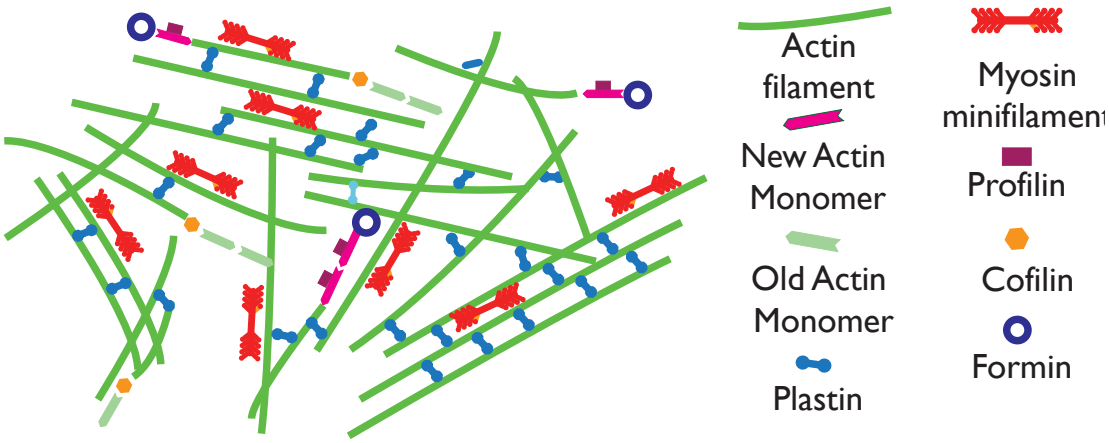

Figure 1.2: Schematic of *C. elegans* cortex. Actin filaments (green) are bundled together by crosslinkers plastin and annilin. Formin nucleates actin filaments, and profilin aids in actin filament elongation. Myosin minifilaments (red) bind to and process along actin filaments.

1.2 Detailed image analysis provides information on biological systems at multiple scales

Digital images are essentially grids of photon counts recorded by sensors. By treating images as distributions of signals, one can use statistical methods to extract different properties of the image. For instance, analysis of a single image can quantify the distribution of signal, which correspond to specific structures in the image. When using timelapse imaging, one must connect the signal in consecutive frames to extract temporal data. Microscopy is clearly a powerful tool to gain insight into biological systems, and there are many forms of image analysis that allow insight

into different features of images. Different analysis tools are suited for insights to dynamics over the entire image, dynamics of individual particles, and subcellular structures and co-localization. I chose different tools that allowed us to quantify cortical flows, actin elongation rates, and subcellular structures to extract detailed information about our system.

One of my primary goals, as described in Chapter 2, was to quantify the cortical flows of the *C. elegans* zygotes during maintenance phase. To do so, I labeled myosin II and recorded the positions of the myosin minifilaments over time. I needed to select a method to connect the signal of the myosin between frames to calculate the velocity field, which is a direct measurement of cortical flows. Here I will describe my chosen analysis method, Particle Image Velocimetry (PIV), and the rationale for doing so.

PIV was originally used to investigate fluid dynamics but has been adapted to biological systems as well[46]. PIV relies on tracer particles whose movement represents the underlying flow field in the system. PIV software identifies interrogation regions (generally in the range 16x16 – 64x64 pixels) and calculates the cross correlation of the interrogation region at t_1 with interrogation regions of the same size at t_2[47]. The location at t_2 which produces the maximum correlation with the reference location at time t_1 is the most likely location of the interrogation region at t_2. This provides a direct estimate of the displacement of the tracer particles over that time period. By doing this for many interrogation regions, it is possible to construct an instantaneous displacement field[48].

Many PIV software packages calculate the displacement field in a grid system. This is not ideal for biological systems, where variations in particle density and illumination are common. Consequently, in the present thesis, I use Quantitative Fluorescent Speckle Microscopy (QFSM), which addresses this issue by identifying candidate speckles that are above the threshold of noise in a video, and only calculating the displacement for these candidate speckles[49].

In order for PIV to produce robust results, several criteria must be met. The simplest criteria is that the image has to be large enough to allow for many interrogation windows[46,47]. There also must be a sufficiently high "image density", or average number of particle image pairs per interrogation volume[50]. For instance, if the interrogation region is too small, there may not be any particles at time t_2. The results velocity vector would then be between a particle at time t_1 and the noise signal at time t_2. Finally, the signal to noise ratio must be sufficiently high so the cross correlation between two particles is significantly higher than the cross correlation between a particle at $t_1$and noise at t_2[50].

PIV quantifies the instantaneous velocity field at each frame, which makes it a powerful method to quantify the macroscopic dynamics of a system. In Chapter 2, I use PIV to quantify the cortical flows in the *C. elegans* zygote. I only considered videos in which the signal to noise ratio was sufficiently high (>2.4). The myosin signal was quite dense, so the image density was high enough for PIV to function well. By comparing how the velocity fields change frame to frame, I was able to quantify how the patterns of cortical flow changed spatially and temporally. Since I was only interested in quantifying the cortical flows, I did not need detailed information on individual myosin minifilaments.

Later in Chapter 2, I wanted to quantify the rates of actin elongation under different conditions. For our imaging setup, I collected timelapse images of fluorescently labeled formin, which is associated with the barbed ends of actin filaments during periods of elongation[1,22,23]. Previous studies have tracked formin motion over time to calculate the actin elongation rate[23]. There are two populations of formin observed in the *C. elegans* cortex; the first is a pool of formin that is not associated with a growing filament and the second is a pool of formin that is associated with elongating actin filaments[23].

I sought to find an analysis method that would provide the trajectories of individual formin speckles over time so I could then isolate the pool of formin that was associated with elongating actin filaments. PIV does not provide information on specific speckles, so it would not be sufficient for this goal. In contrast to PIV, Single Particle Tracking (SPT) can be used to track the displacement of individual microscopic particles (fluorescent proteins, quantum dots, or other markers that appear as puncta in images)[51,52]. SPT precisely locates each particle and measures its individual dynamics over time[51]. Therefore, I chose SPT to calculate the actin elongation rate.

SPT relies on two steps: localization and linking. During localization, the precise location (generally the centroid of the puncta) must be found. Some methods calculate the intensity-weighted centroid of the intensity signal to refine the calculation of the exact particle location[53]. Other methods fit a Gaussian distribution to the intensities of the pixels containing each candidate particle, which is accurate but computationally expensive[54]. During the linking step, the particles' locations are linked together frame to frame to form trajectories. In particle linking, some methods minimize the distance from all particles at t_1 to t_2[53,55]. Others use motion models to refine estimates of particle displacement[51,55,56].

For SPT to work, the speckles need to be punctate and sufficiently bright to identify[51,52]. If the speckles are not punctate, one cannot find the center of the particle with high enough accuracy. Additionally, the speckles must be sufficiently sparse. If the puncta are overlapping, particle localization will be skewed. Furthermore, high particle density causes linking errors so the particle trajectories will not be accurate[51,52,55].

One benefit of SPT is the ability to consider the dynamics of individual trajectories and sort trajectories based on their dynamics. SPT can provide several key insights to the properties of microscopic particles. Most obviously, the velocity of particles can be directly calculated from

trajectories, specifically particles undergoing directed motion. If one is only interested in particles undergoing motion about a certain speed, one could calculate the speed of each trajectory and only consider those with a velocity in the range of interest. Additionally, calculating the mean squared displacement and fitting it allows one to calculate the diffusion coefficient, D, and anomalous exponent, α[51,52]. The value of α provides key information into the underlying motion of the particles. For instance, $\alpha = 0$ means the particle is confined. When α is greater than zero but less than one, the particle is undergoing subdiffusive motion. When $\alpha = 1$ the particle is undergoing Brownian motion. An $\alpha > 1$ means that the particle is superdiffusive, while an $\alpha = 2$ means that the particle is undergoing ballistic or directed motion[51].

I sought to distinguish formin particles that were associated with actively elongating actin filaments, which undergo ballistic motion, from formin that are in the pool of filaments that are not associated with actively elongating filaments, which undergo Brownian motion. I then wanted to calculate the velocity of only the particles that were associated with actively elongating filaments. When collecting images, I ensured that the density of formin speckles was low enough that they could be easily distinguished. I tracked formin speckles using SPT, and then used α to select the subpopulation undergoing ballistic motions which corresponds to the subpopulation associated with actively elongating actin filaments. This allowed us to directly calculate the actin elongation rate in our system.

One obvious question is: why did I choose different methods to quantify cortical flows and the actin elongation rates? I was essentially measuring velocity in both cases, so why not choose the same method? I made the decision based on two considerations: the level of detail the analysis provided and the requirements for the analysis method to produce robust results. When calculating cortical flows, I did not need information on individual myosin speckles, I was simply interested

in the overall velocity field, so SPT would have provided more detail than necessary. Additionally, my videos of myosin during maintenance phase were quite dense, which is useful for PIV but a hindrance in SPT. In contrast, I needed detailed information on the dynamics of each formin speckle when measuring the actin elongation rate. Therefore, PIV would not have provided enough detail while SPT provided enough. I adjusted my image collection methods to achieve the correct particle density for SPT to produce clear results.

Thus far, I have focused on how image analysis can quantify the dynamics of a system. Image analysis can also be used to characterize subcellular structures. I used approaches to quantify subcellular structures in Sections 2.3, when looking at the actomyosin architecture in cells. In Chapter 4, I relied heavily on statistical methods to quantify the co-localization of different proteins and cellular structures. In multi-channel imaging, one can directly see where the signals are co-expressed. It is also straightforward to quantify the co-localization of two channels. The Pearson correlation coefficient is used to quantify correlation between channels and can give clear results for strong correlation or anti-correlation[57]. However, at intermediate levels of correlation, it can be difficult to interpret the Pearson correlation coefficient[57,58]. The Manders coefficient can be used to quantify co-localization between two channels by quantifying the percent of channel A that is co-localized with channel B and vice versa, producing two measurements[58–60].

While the methods described above characterize the relations between two channels, there are many other image analysis tools that are readily available to analyze specific structures. For instance, to analyze linear structures, one can take transects across a single location and look at the distribution of pixel intensities across that transect. One can then compare these transects by looking at the integrated intensity. Or, one can compare differences in the distributions of the transects of two different signals by calculating the Kolmogorov-Smirnov test[61].

Understanding images as matrices of convolved point spread functions makes it simple to create visual representations of idealized data[62]. The diffraction limit of light is approximately 200 nm, so diffraction limited particles produce point spread functions (usually Gaussian) that are convolved with other objects, producing detailed images. If the point spread function of the imaging system is known, it is possible to create synthetic images of the structures[62]. If one specifies the location of particles, it is simple to create a point spread function at that location that matches the imaging conditions used in experiments. For instance, one could make synthetic images of overlapping structures, or structures that are simply in close proximity, and determine if the chosen analysis methods pick up on these differences. In Chapter 2, I created synthetic images of crosslinkers and actin filament from simulations I ran (simulations are discussed in more detail in Section 1.3 and Chapter 2).

1.3 Models provide detailed insights into actomyosin networks at macroscopic and microscopic scales

Models can be a powerful tool to understand the cell cortex, particularly when paired with experiments. There are many approaches to modeling the cell cortex, but models generally fall into two categories: hydrodynamic active gel models and agent-based models (see Figure 1.3 for a comparison of agent-based and active gel models).

Active gel models describe the macroscopic properties of the cortex without directly depending on any microscopic information[63]. Active gel models only apply for systems larger than the mesh size of the actin network. The cortex is essentially viewed as a viscoelastic system. At short time scales (shorter than the turnover of the cortex), the system is dominated by elastic behavior[63–65]. At long time scales (greater than the turnover of the cortex), the system behaves as

a liquid with a given viscosity[64,65]. "Turnover of the cortex" is a vague term – actin filaments and myosin minifilaments undergo constant turnover, and crosslinkers bind and unbind, which is generally referred to as turnover in the context of active gel models. The lifetime of crosslinkers is generally used at the turnover time[63–65], but the turnover of actin filaments is occasionally used instead[6,39,66]. The turnover of actin, motors, and crosslinkers can all affect the viscoelastic regimes of active gel models[2,15,63,65,67].

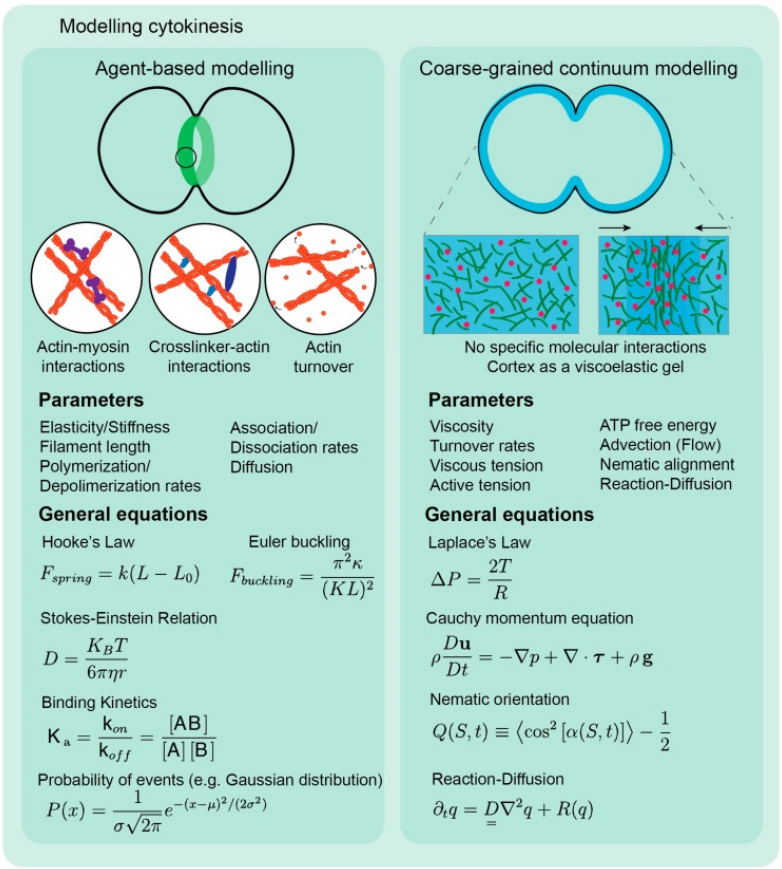

Figure 1.3: Comparison of agent-based and active gel (continuum based) models. From Leite *et al*., "Network contractility during cytokinesis – from molecular to global views." *Biomolecules*. 2019.[29]

Contraction and expansion can be caused in active gel models through various means. Introducing certain boundary conditions can cause contraction or expansion of the system[65]. Or, changing physical aspects of the system – such as changing the system thickness, or introducing a chemical gradient in the space – can promote contraction or expansion[65].

Active gel models provide some clear insights into the conditions under which cortical flows can emerge. Cortical flows emerge when the cortex is in the viscous regime[2,15,67]. Since the viscous regime is set by cortex turnover, this means that turnover must occur and that cortical flows must be on a longer time scale than the turnover of the cortex[15,66,67]. As one would expect, introducing gradients of cortical tension can cause flows to emerge. Interestingly, introducing anisotropies in cortical tension can also cause flows to emerge[6,15].

Active gel models can characterize flows observed in the cortex. For instance, active gel models provide a simple means to calculate the hydrodynamic length scale, which is a characteristic of how long-ranged flows are. Mayer *et al.* investigated cortical flows in the polarity establishment in the single-cell *C. elegans* zygote and modeled flows as an active gel. They perturbed actin and myosin turnover to test the effects on the hydrodynamic length scale of these cortical flows. Increasing myosin turnover and decreasing actin depolymerization greatly increased the hydrodynamic length scale. This corresponds with increasing the effective viscosity in the system. In contrast, decreasing actin polymerization decreased the hydrodynamic length scale and eventually eliminated cortical flows altogether, which corresponds with reducing the effective viscosity.

Agent-based models explicitly simulate and track the dynamics of individual components of cytoskeletal systems[68]. These models will define a set of rules that governs how a component will stochastically move and interact with other components in its environment[68]. Models define

the chemistry, mechanics, diffusion and transport, and mechanochemical feedback objects undergo[69]. There are many open-source agent-based simulation software packages available to use, each with benefits and drawbacks[69]. Popov *et al.* provide a comparison of many of the most popular software packages[69].

Agent-based models require the user to input microscopic information about their system of interest. Users define the stiffness, length, and binding/unbinding rates of crosslinkers and motors[69–71]. In most software packages, users also define the unloaded speed of myosin. The microscopic behavior of actin filaments can also be defined. Depending on the capabilities of the software, users can define whether the actin filaments are fixed in length, undergoing assembly/disassembly, or if they are treadmilling[69–71]. One of the most powerful benefits of using agent-based simulations is the direct link between microscopic and macroscopic scales they provide. Freedman *et al.* varied the density of crosslinkers and motors in the system and observed different behaviors (bundling, contracting, and polarity sorting) emerge from the different conditions[70]. Agent-based simulations produce detailed information on the position and activity of the actin filaments, crosslinkers, and motors in the system. This provides a level of detailed information about the system inaccessible in experiments and active gel models.

Some agent-based simulations incorporate actin turnover by using a "treadmilling" fiber that undergoes constant assembly from the barbed end and disassembly from the pointed end at the same rate[26,42,72,73]. When actin filaments undergo treadmilling, the fibers must be sufficiently crosslinked, and myosin must be sufficiently processive, to produce contractility[26,73]. If these conditions are not met, the simulation may produce network extension rather than contraction[73]. Agent-based simulations provide a look into what sets of microscopic network characteristics are required to produce contractility.

1.4 Approaches to study cortical flows via paired experiments and simulations

One fundamental challenge of studying cortical flows is that components of the cortex can play roles in force generation and resistance to deformations. Crosslinkers affect the stiffness of the cortex, but they can also affect force generation and propagation[2,36]. Myosin acts as both a crosslinker and a motor[1,2,19]. Similarly, changing actin polymerization/depolymerization affects both the overall actin density as well as the connectivity of the cortex[15,39]. Given the complex nature of the cortex, it is impossible to reduce a single component of the cortex to have only one effect in establishing cortical dynamics. However, looking across experimental evidence, active gel simulations, and agent-based simulations, some trends do emerge.

Intermediate levels of connectivity, controlled by crosslinker activity and actin binding proteins, optimize rate of cortical flows. Several studies focused specifically on the connectivity of the cortex and macroscopic behaviors. Chugh *et al.* investigated the connection between actin filament length (corresponding to cortex thickness) and cortical tension[41]. In both simulations and experiments, they found that increasing the actin filament length initially increases the cortical tension, but past a critical point, increasing the actin filament length decreases cortical tension[41]. Similarly, Ding *et al.* investigated the effect of plastin density on polarization and cytokinesis in *C. elegans*[28]. They completed simulations in which they varied the number of crosslinkers in the system and found that when the crosslinker density was very low, contraction did not occur. Increasing crosslinker density increased the rate of contraction until a critical point at which the rate of contraction decreased again[28].

While Chugh *et al.* focus on actin filament length and Ding *et al.* focus on crosslinker density, they are both essentially perturbing the level of connectivity in the cortex. In both studies,

an intermediate level of connectivity is necessary to optimize macroscopic behaviors (cortical tension, or the rate of cortical flow). This implies that when the network is under-connected, it is more prone to collapsing. At the intermediate level of connectivity, the network is connected and deformable. At high levels of connectivity, the network is overly connected and rigid. Since actin turnover and crosslinker density affect the connectivity of the cortex, both properties are critical for producing macroscopic behaviors. The connectivity of the network is determined by actin binding proteins that affect actin filament assembly dynamics, and crosslinkers.

Turnover of components of the cortex, particularly turnover of actin filaments, alters cortical tension and flows. The role of actin turnover in the cortex has been studied through experiments, active gel models, and agent-based models. Active gel models provide a very clear understanding of the importance of turnover; at time scales shorter than the turnover of the cortex, the cortex behaves as an elastic solid[2,15]. Flows only emerge at timescales longer than the rate of turnover[2,15]. Altering the turnover thus changes viscoelastic properties, such as the hydrodynamic length scale[15]. Agent-based simulations investigate actin filament turnover via "treadmilling." These simulations are able to precisely identify which conditions – including crosslinker and motor binding properties and dynamics – are necessary for treadmilling to lead to contraction or cortical flows[26,27,42,72,73]. Experimentally, inhibiting proteins that regulate actin filament turnover disrupts cortical flow[15,39]. Inhibiting actin depolymerization increases cortical flow, while inhibiting actin polymerization decreases cortical flow. Of course, these are not definitive rules. Perturbing actin filament turnover may cause a range of responses at different levels of perturbation.

Pairing experiments and agent-based simulations has many advantages for investigating the link between microscopic details of the cell cortex and macroscopic behavior[28,41,74–76]. Experiments ground the investigation in true biological systems. Based on the experimental and

data analysis techniques used, it is possible to gain information about both the macroscopic and microscopic behavior of the system *in vivo*. Agent-based simulations allow users to directly incorporate known information about the microscopic characteristics of the system and observe what macroscopic behaviors arise. One of the biggest benefits to using simulations is the precise control simulations offer. In experiments, crosslinker and myosin activity can affect the turnover of actin filaments and that cannot be controlled for[1,19,69,77]. In simulations, the user has the power to alter a single component of the system and see how everything else responds. Agent-based simulations also provide more information about the precise behavior of system components than is accessible in experiments. If simulations accurately reflect the experimental system, simulations can provide a more simple, detailed characterization of the system.

While pairing simulations and experiments is promising in theory, in practice it falls short of the ideal. Most studies use approximations of the experimental system rather than quantitatively pairing simulations and experiments. However, as I've previously stated, the cortex is a complex system, and it is difficult to draw conclusions when comparing different systems. While trends may qualitatively match, the ability to quantitatively compare simulations and experiments is not accessible.

In Chapter 2, I focus on pairing experiments with agent-based simulations to explore the connection between the microscopic properties of the cortex on cortical flows in *C. elegans* embryos. To my knowledge, there are no studies that quantitatively ground simulations in experimental data and provide quantitative comparisons between simulated and experimental conditions. In our work, I look to fill this niche.

1.5 Thesis Topics

This body of work details the two major projects I completed as a PhD researcher. In Chapter 2, I present research I completed investigating cortical flows in *C. elegans* during maintenance phase. In this work, I aim to provide quantitative links between simulations and experiments, which has not been previously achieved. I customize agent-based simulations to represent experimentally measured characteristics of the cell cortex. This includes creating a customized fiber class in Cytosim[71,78], which creates filaments that undergo a period of assembly followed by disassembly. These encoded lifetime and dynamics represent actin filament lifetime/assembly dynamics quantified *in vivo*. Additionally, I detail how I found the ideal range of crosslinker binding rates and overall actin density to reproduce the overall actin architecture quantified of *C. elegans* embryos.

I then tested how to impose a myosin gradient in the simulations to produce macroscopic flows. I was able to control the rate of flow by adjusting the steepness of the myosin gradient. Reproducing the actin assembly/disassembly dynamics, actin architecture, and myosin gradient in simulations reproduced flows observed *in vivo*. This was a significant accomplishment; I am not aware of other studies that ground simulations in experimental data as firmly as ours. Next, I investigate perturbing microscopic characteristics of the cell cortex to observe the effect on macroscopic behavior. I quantify the strength of perturbations in experiments and simulations to provide quantitative links between the two.

In the second half of my thesis, I focus on another major project that I completed, studying extracellular vesicles (EVs) in breast cancer cells. EVs are vesicles that are produced within the cell and then secreted through various processes. They play critical roles in cell-to-cell communication, particularly in cancer metastasis. In Chapter 3, I provide background on EVs and

remaining questions in the field. I motivate using microscopy to image EVs *in situ* to learn more about their origin and export pathways.

In Chapter 4, I detail the work I completed studying EVs in triple-negative breast cancer cells. I used volumetric imaging to visualize candidate EV biomarkers *in situ*, prior to export. I use detailed image analysis to quantify the spatial distribution and co-localization of EV proteins that are candidate biomarkers.

1.6 Chapter 1 References

1. Chugh, P. & Paluch, E. K. The actin cortex at a glance. *J. Cell Sci.* **131**, jcs186254 (2018).

2. Salbreux, G., Charras, G. & Paluch, E. Actin cortex mechanics and cellular morphogenesis. *Trends Cell Biol.* **22**, 536–545 (2012).

3. Bray, D. & White, J. G. Cortical Flow in Animal Cells. *Science* **239**, 883–888 (1988).

4. Chabaud, M. *et al.* Cell migration and antigen capture are antagonistic processes coupled by myosin II in dendritic cells. *Nat. Commun.* **6**, 7526 (2015).

5. Liu, Y.-J. *et al.* Confinement and low adhesion induce fast amoeboid migration of slow mesenchymal cells. *Cell* **160**, 659–672 (2015).

6. Ruprecht, V. *et al.* Cortical contractility triggers a stochastic switch to fast amoeboid cell motility. *Cell* **160**, 673–685 (2015).

7. Bergert, M. *et al.* Force transmission during adhesion-independent migration. *Nat. Cell Biol.* **17**, 524–529 (2015).

8. Lämmermann, T. *et al.* Rapid leukocyte migration by integrin-independent flowing and squeezing. *Nature* **453**, 51–55 (2008).

9. Cuenca, A. A., Schetter, A., Aceto, D., Kemphues, K. & Seydoux, G. Polarization of the C. elegans zygote proceeds via distinct establishment and maintenance phases. *Development* **130**, 1255–1265 (2003).

10. Munro, E., Nance, J. & Priess, J. R. Cortical Flows Powered by Asymmetrical Contraction Transport PAR Proteins to Establish and Maintain Anterior-Posterior Polarity in the Early C. elegans Embryo. *Dev. Cell* **7**, 413–424 (2004).

11. Lang, C. F. & Munro, E. The PAR proteins: from molecular circuits to dynamic self-stabilizing cell polarity. *Development* **144**, 3405–3416 (2017).

12. Hird, S. N. & White, J. G. Cortical and cytoplasmic flow polarity in early embryonic cells of Caenorhabditis elegans. *J. Cell Biol.* **121**, 1343–1355 (1993).

13. Department of Molecular & Cellular Biology, University of California, Davis, Davis, CA 95616, USA., Rose, L. & Gonczy, P. Polarity establishment, asymmetric division and segregation of fate determinants in early C. elegans embryos. *WormBook* 1–43 (2014) doi:10.1895/wormbook.1.30.2.

14. Munro, E., Nance, J. & Priess, J. R. Cortical Flows Powered by Asymmetrical Contraction Transport PAR Proteins to Establish and Maintain Anterior-Posterior Polarity in the Early C. elegans Embryo. *Dev. Cell* **7**, 413–424 (2004).

15. Mayer, M., Depken, M., Bois, J. S., Jülicher, F. & Grill, S. W. Anisotropies in cortical tension reveal the physical basis of polarizing cortical flows. *Nature* **467**, 617–621 (2010).

16. Reymann, A.-C., Staniscia, F., Erzberger, A., Salbreux, G. & Grill, S. W. Cortical flow aligns actin filaments to form a furrow. *eLife* **5**, e17807 (2016).

17. Oon, C. H. & Prehoda, K. E. Asymmetric recruitment and actin-dependent cortical flows drive the neuroblast polarity cycle. *eLife* **8**, e45815 (2019).

18. Roubinet, C. *et al.* Spatio-temporally separated cortical flows and spindle geometry establish physical asymmetry in fly neural stem cells. *Nat. Commun.* **8**, 1383 (2017).

19. Blanchoin, L., Boujemaa-Paterski, R., Sykes, C. & Plastino, J. Actin Dynamics, Architecture, and Mechanics in Cell Motility. *Physiol. Rev.* **94**, 235–263 (2014).

20. Kasza, K. E. *et al.* Actin Filament Length Tunes Elasticity of Flexibly Cross-Linked Actin Networks. *Biophys. J.* **99**, 1091–1100 (2010).

21. Fritzsche, M., Lewalle, A., Duke, T., Kruse, K. & Charras, G. Analysis of turnover dynamics of the submembranous actin cortex. *Mol. Biol. Cell* **24**, 757–767 (2013).

22. Funk, J. *et al.* Profilin and formin constitute a pacemaker system for robust actin filament growth. *eLife* **8**, e50963 (2019).

23. Li, Y. & Munro, E. Filament-guided filament assembly provides structural memory of filament alignment during cytokinesis. *Dev. Cell* **56**, 2486-2500.e6 (2021).

24. Higashida, C. *et al.* Actin Polymerization-Driven Molecular Movement of mDia1 in Living Cells. *Science* **303**, 2007–2010 (2004).

25. Carlier, M. F. *et al.* Actin depolymerizing factor (ADF/cofilin) enhances the rate of filament turnover: implication in actin-based motility. *J. Cell Biol.* **136**, 1307–1322 (1997).

26. Hiraiwa, T. & Salbreux, G. Role of Turnover in Active Stress Generation in a Filament Network. *Phys. Rev. Lett.* **116**, 188101 (2016).

27. Carlier, M.-F. & Shekhar, S. Global treadmilling coordinates actin turnover and controls the size of actin networks. *Nat. Rev. Mol. Cell Biol.* **18**, 389–401 (2017).

28. Ding, W. Y. *et al.* Plastin increases cortical connectivity to facilitate robust polarization and timely cytokinesis. *J. Cell Biol.* **216**, 1371–1386 (2017).

29. Leite, J., Osorio, D. S., Sobral, A. F., Silva, A. M. & Carvalho, A. X. Network Contractility during Cytokinesis—From Molecular to Global Views. *Biomolecules* **9**, 194 (2019).

30. Falzone, T. T., Lenz, M., Kovar, D. R. & Gardel, M. L. Assembly kinetics determine the architecture of α-actinin crosslinked F-actin networks. *Nat. Commun.* **3**, 861 (2012).

31. Flanagan, L. A. *et al.* Filamin A, the Arp2/3 complex, and the morphology and function of cortical actin filaments in human melanoma cells. *J. Cell Biol.* **155**, 511–518 (2001).

32. Yamashiro, S., Yamakita, Y., Ono, S. & Matsumura, F. Fascin, an Actin-bundling Protein, Induces Membrane Protrusions and Increases Cell Motility of Epithelial Cells. *Mol. Biol. Cell* **9**, 993–1006 (1998).

33. Courson, D. S. & Rock, R. S. Actin Cross-link Assembly and Disassembly Mechanics for α-Actinin and Fascin. *J. Biol. Chem.* **285**, 26350–26357 (2010).

34. Gardel, M. L. *et al.* Elastic Behavior of Cross-Linked and Bundled Actin Networks. *Science* **304**, 1301–1305 (2004).

35. Kim, T., Gardel, M. L. & Munro, E. Determinants of Fluidlike Behavior and Effective Viscosity in Cross-Linked Actin Networks. *Biophys. J.* **106**, 526–534 (2014).

36. Dasanayake, N. L. & Carlsson, A. E. Stress generation by myosin minifilaments in actin bundles. *Phys. Biol.* **10**, 036006 (2013).

37. Hundt, N., Steffen, W., Pathan-Chhatbar, S., Taft, M. H. & Manstein, D. J. Load-dependent modulation of non-muscle myosin-2A function by tropomyosin 4.2. *Sci. Rep.* **6**, 20554 (2016).

38. Barua, B., Nagy, A., Sellers, J. R. & Hitchcock-DeGregori, S. E. Regulation of Nonmuscle Myosin II by Tropomyosin. *Biochemistry* **53**, 4015–4024 (2014).

39. Tinevez, J.-Y. *et al.* Role of cortical tension in bleb growth. *Proc. Natl. Acad. Sci.* **106**, 18581–18586 (2009).

40. Sedzinski, J. *et al.* Polar actomyosin contractility destabilizes the position of the cytokinetic furrow. *Nature* **476**, 462–466 (2011).

41. Chugh, P. *et al.* Actin cortex architecture regulates cell surface tension. *Nat. Cell Biol.* **19**, 689–697 (2017).

42. Mak, M., Zaman, M. H., Kamm, R. D. & Kim, T. Interplay of active processes modulates tension and drives phase transition in self-renewing, motor-driven cytoskeletal networks. *Nat. Commun.* **7**, 1–12 (2016).

43. McFadden, W. M., McCall, P. M., Gardel, M. L. & Munro, E. M. Filament turnover tunes both force generation and dissipation to control long-range flows in a model actomyosin cortex. *PLOS Comput. Biol.* **13**, e1005811 (2017).

44. Srivastava, V. & Robinson, D. N. Mechanical Stress and Network Structure Drive Protein Dynamics during Cytokinesis. *Curr. Biol.* **25**, 663–670 (2015).

45. Timmons, L., Court, D. L. & Fire, A. Ingestion of bacterially expressed dsRNAs can produce specific and potent genetic interference in Caenorhabditis elegans. *Gene* **263**, 103–112 (2001).

46. Raffel, M. *et al. Particle Image Velocimetry: A Practical Guide*. (Springer, 2018).

47. Westerweel, J. Fundamentals of digital particle image velocimetry. *Meas. Sci. Technol.* **8**, 1379 (1997).

48. R, M. Instantaneous velocity field measurements in unsteady gas flow by speckle velocimetry. *Appl. Opt.* **22**, (1983).

49. Danuser, G. & Waterman-Storer, C. M. Quantitative fluorescent speckle microscopy of cytoskeleton dynamics. *Annu. Rev. Biophys. Biomol. Struct.* **35**, 361–387 (2006).

50. Adrian, R. J. Twenty years of particle image velocimetry. *Exp. Fluids* **39**, 159–169 (2005).

51. Manzo, C. & Garcia-Parajo, M. F. A review of progress in single particle tracking: from methods to biophysical insights. *Rep. Prog. Phys. Phys. Soc. G. B.* **78**, 124601 (2015).

52. Wirtz, D. Particle-Tracking Microrheology of Living Cells: Principles and Applications. *Annu. Rev. Biophys.* **38**, 301–326 (2009).

53. Crocker, J. C. & Grier, D. G. Methods of Digital Video Microscopy for Colloidal Studies. *J. Colloid Interface Sci.* **179**, 298–310 (1996).

54. Zhang, B., Zerubia, J. & Olivo-Marin, J.-C. Gaussian approximations of fluorescence microscope point-spread function models. *Appl. Opt.* **46**, 1819–1829 (2007).

55. Chenouard, N. *et al.* Objective comparison of particle tracking methods. *Nat. Methods* **11**, 281–289 (2014).

56. Jaqaman, K. *et al.* Robust single-particle tracking in live-cell time-lapse sequences. *Nat. Methods* **5**, 695–702 (2008).

57. Dunn, K. W., Kamocka, M. M. & McDonald, J. H. A practical guide to evaluating colocalization in biological microscopy. *Am. J. Physiol. Cell Physiol.* **300**, C723-742 (2011).

58. Lagache, T., Sauvonnet, N., Danglot, L. & Olivo-Marin, J.-C. Statistical analysis of molecule colocalization in bioimaging. *Cytom. Part J. Int. Soc. Anal. Cytol.* **87**, 568–579 (2015).

59. Dunn, K. W., Kamocka, M. M. & McDonald, J. H. A practical guide to evaluating colocalization in biological microscopy. *Am. J. Physiol. Cell Physiol.* **300**, C723-742 (2011).

60. Manders, E. M. M., Verbeek, F. J. & Aten, J. A. Measurement of co-localization of objects in dual-colour confocal images. *J. Microsc.* **169**, 375–382 (1993).

61. Jr, F. J. M. The Kolmogorov-Smirnov Test for Goodness of Fit. *J. Am. Stat. Assoc.* **46**, 68–78 (1951).

62. Dmitrieff, S. & Nédélec, F. ConfocalGN: A minimalistic confocal image generator. *SoftwareX* **6**, 243–247 (2017).

63. Joanny, J.-F. & Prost, J. Active gels as a description of the actin-myosin cytoskeleton. *HFSP J.* **3**, 94–104 (2009).

64. Prost, J., Jülicher, F. & Joanny, J.-F. Active gel physics. *Nat. Phys.* **11**, 111–117 (2015).

65. Jülicher, F., Kruse, K., Prost, J. & Joanny, J.-F. Active behavior of the Cytoskeleton. *Phys. Rep.* **449**, 3–28 (2007).

66. Saha, A. *et al.* Determining Physical Properties of the Cell Cortex. *Biophys. J.* **110**, 1421–1429 (2016).

67. Levayer, R. & Lecuit, T. Biomechanical regulation of contractility: spatial control and dynamics. *Trends Cell Biol.* **22**, 61–81 (2012).

68. Cortes, D. B. *et al.* Unite to divide – how models and biological experimentation have come together to reveal mechanisms of cytokinesis. *J. Cell Sci.* **131**, jcs203570 (2018).

69. Popov, K., Komianos, J. & Papoian, G. A. MEDYAN: Mechanochemical Simulations of Contraction and Polarity Alignment in Actomyosin Networks. *PLOS Comput. Biol.* **12**, e1004877 (2016).

70. Freedman, S. L. *et al.* Mechanical and kinetic factors drive sorting of F-actin cross-linkers on bundles. *Proc. Natl. Acad. Sci.* **116**, 16192–16197 (2019).

71. Belmonte, J. M., Leptin, M. & Nédélec, F. A theory that predicts behaviors of disordered cytoskeletal networks. *Mol. Syst. Biol.* **13**, 941 (2017).

72. Oelz, D. B., Rubinstein, B. Y. & Mogilner, A. A Combination of Actin Treadmilling and Cross-Linking Drives Contraction of Random Actomyosin Arrays. *Biophys. J.* **109**, 1818–1829 (2015).

73. Lenz, M. Reversal of contractility as a signature of self-organization in cytoskeletal bundles. *eLife* **9**, e51751 (2020).

74. Kruse, K. & Jülicher, F. Actively Contracting Bundles of Polar Filaments. *Phys. Rev. Lett.* **85**, 1778–1781 (2000).

75. Liverpool, T. B. & Marchetti, M. C. Bridging the microscopic and the hydrodynamic in active filament solutions. *Europhys. Lett.* **69**, 846–852 (2005).

76. Aranson, I. S. & Tsimring, L. S. Patterns and collective behavior in granular media: Theoretical concepts. *Rev. Mod. Phys.* **78**, 641–692 (2006).

77. Guha, M., Zhou, M. & Wang, Y.-L. Cortical actin turnover during cytokinesis requires myosin II. *Curr. Biol. CB* **15**, 732–736 (2005).

78. Nedelec, F. & Foethke, D. Collective Langevin dynamics of flexible cytoskeletal fibers. *New J. Phys.* **9**, 427–427 (2007).

CHAPTER 2

MICROSCOPIC CONTROL OF CORTICAL FLOWS IN POLARIZED *C. ELEGANS* ZYGOTES

2.1 Abstract

The cell cortex produces forces that control changes in cell shape, intracellular motion, and the movement of cells within their environments. These forces—cortical tension—drive flows over length scales of tens of microns and time scales of minutes or longer. Cortical flows are thought to emerge from microscopic interactions between actin filaments, crosslinkers, and motors. These interactions are regulated by actin binding proteins that control filament assembly, crosslinking, and motor activity, but how the regulation of microscopic properties and interactions tune macroscopic cortical flows remains poorly understood. Here, I address this question through studies of steady-state flows in polarized one-cell *C. elegans* embryos. I combine microscopy and quantitative image analysis to characterize the microscopic properties of the *C. elegans* cortex. I use these and other previously published measurements to tightly constrain agent-based simulations and show that these simulations accurately reproduce macroscopic flows quantified *in vivo*. I then use these simulations to predict how varying the levels of key regulators of actin filament assembly and crosslinking tune the magnitude and coherence of cortical flows, and I perform corresponding manipulations *in vivo*. I find close agreement between my simulations and the corresponding experiments. This demonstrates that the microscopic interactions that I consider are sufficient to drive cortical flows and account for tunable variation in macroscopic flow dynamics. This work establishes a computational platform for further mechanistic studies and for

understanding how variations in microscopic properties and interactions shape the emergent dynamics of the cell cortex.

2.2 Introduction

The cell cortex is an actin rich layer directly beneath the plasma membrane of animal cells[1]. The main components of the cell cortex are actin filaments, crosslinkers, and bipolar filaments formed by non-muscle myosin II (hereon myosin), as well as other proteins that control assembly and disassembly of actin filaments[1–3]. The cell cortex produces active contractile forces, and at the same time it resists deformation. This balance of active force and internal resistance leads to local deformations. Spatiotemporal control of cortical deformations drives changes in cell shape, cell movements, and intracellular transport[1,4–6].

One class of motion produced by the cell cortex are cortical flows, which underlie a variety of mesoscopic behaviors, including amoeboid cell motility, cell polarization, and cell division[7]. For example, in amoeboid cells, cortical flows couple to external substrates to produce directional motility[4,8–11]. In early *C. elegans* embryos and *Drosophila* neuroblasts, cortical flows transport polarity proteins to break symmetry and establish cell polarity[10,12–15]. During cytokinesis, cortical flows transport cortical actin filaments, myosin II, and other materials towards the equator where the contractile ring forms. During asymmetric cell division, cortical flows position the cleavage furrow to set the asymmetry in sizes of daughter cells[12,16,17].

On a macroscopic scale, the cortex can be described as an active gel in which cortical flows are driven by spatial gradients of cortical tension working against an effectively viscous resistance[1,18,19]. Microscopic interactions of actin filaments, myosin, and crosslinkers determine the cortical tension and effective viscosity[1,2,20]. However, it is not fully understood how cortical

flows are shaped by these microscopic properties and dynamics. On the microscopic scale, cortical tension is produced by motors interacting with filaments, and the magnitude of tension depends on the density of motors and filaments[2,18,19,21]. In addition, the ability to build and transmit force over larger distances depends on the connectivity of the cortex, and thus on the densities of motors, actin filaments, and crosslinkers[1,2,20]. The elasticity is largely determined by the crosslinker binding properties, while the effective viscosity is set by the resistance of cortical actin filaments and crosslinkers to deformation, which is dissipated over time by crosslinker unbinding and filament turnover[1,2,18,19]. Therefore, the magnitude of the effective viscosity depends on the density of actin and crosslinkers, as well as the rates at which they turnover[2,18]. Altogether, this is a complicated system; the microscopic characteristics of actin filaments, myosin, and crosslinkers contribute to both force generation and transmission, as well as resistance to deformations caused by these forces[2,18,19,22]. The relationship between cortical flow and microscopic parameters of the cortex is inherently complex.

There have been many studies investigating how cortical flows arise from microscopic interactions using experiments and simulations[4,16,23–25]. These studies have provided some key qualitative insights into how cortical flows depend on microscopic parameters. For example, both experiments and models highlight the necessity for intermediate levels of connectivity to produce cortical flows. However, the utility of comparing the models and experiments has been limited by the fact that the models are typically not well-grounded by microscopic measurements in the same experimental system. Even similar systems can have different behaviors depending on how the properties are tuned. Thus, simulations parameterized based on qualitative observations may not accurately represent the biological system of interest.

Here I use a combination of agent-based simulations and experiments to investigate how microscopic dynamics of filament assembly and crosslinking shape cortical flows in the polarized one-cell *C. elegans* embryo. I achieve a tight integration of models and experiments in two ways: First, I use quantitative microscopy and image analysis in *C. elegans* to constrain key parameters in simulations that govern the dynamics of actin filaments, crosslinkers and motors. Second, I focus on the quasi-steady-state flows that occur during mitosis in polarized embryos, which allows the use of well-defined boundary conditions and facilitates direct comparison between simulated and experimentally observed rates and patterns of cortical flow.

I first establish that the resulting simulations are sufficient to reproduce the rates and patterns of flow observed in polarized embryos. I then use these simulations as a foundation to explore how specific actin binding proteins shape cortical flows, focusing on three highly conserved factors that control actin filament nucleation (formin/CYK-1), elongation (profilin/PFN-1) and bundling (plastin/PLST-1). Each of these proteins help establish the macroscopic properties of the cortex, so altering the expression of these proteins is expected to have a significant effect on cortical flows. I use simulations to predict how varying the levels of these factors affects the rates and patterns of macroscopic contractility and flow. Then I perform the corresponding experiments *in vivo* and compare the results to model predictions.

For all three perturbations I observe strong agreement between model predictions and experiments, further confirming the ability of my simulations to capture microscopic origins of cortical flow in this system. There is a biphasic dependence of flow speeds based on the expression of these proteins. My analysis suggests that this is because all three perturbations affect the connectivity of the cortex, which in turn affects both force transmission and resistance to deformation. For mild depletions, reduced resistance leads to increased flows. For more extreme

depletions, connectivity is reduced to the point that force transmission, and thus cortical flows, ultimately fail. Cortical flows have different sensitivities to these three perturbations, which is likely because these affect the resistance to deformation and force transmission in distinct ways.

2.3 Results

In this work, I use polarized single-cell *C. elegans* embryos as a model system. During this period of time, the cortex is composed largely of long, unbranched actin filaments assembled by formin/CYK-1[10,12,17]. These filaments are organized into small bundles that are decorated by the crosslinking protein plastin/PLST-1[10,12,16]. Contractile forces are produced by a single motor protein myosin II which is organized into bipolar minifilaments with a few dozen motors each[10,26]. A spatial gradient of myosin drives a pattern of steady-state cortical flow from the posterior pole to the anterior pole[10].

2.3.1 Actin filaments undergo distinct phases of assembly and disassembly

I first sought to quantify the microscopic properties of the *C. elegans* cortex and use them to tightly constrain my simulations. The most fundamental component of the cell cortex is actin, so I first focused on capturing a quantitative microscopic description of actin filament assembly and disassembly dynamics to incorporate into my model. By tracking individual formin molecules, Li and Munro showed that linear actin filaments assemble in the *C. elegans* cortex at ~1.5 μm/s[17]. Using single-molecule imaging of labeled actin subunits, they showed that, due to disassembly, actin filaments at the cortex have a mean lifetime of ~8 seconds[5].

These single-molecule observations did not reveal the pattern of disassembly of individual filaments, e.g., whether filaments disassemble from their pointed ends to produce treadmilling

dynamics or stochastically through severing and disassembly along the entire filament. These different modes of disassembly could produce different emergent dynamics of contractility and flow. To distinguish these possibilities, I used embryos expressing a GFP-tagged form of plastin to visualize actin filament turnover dynamics *in vivo* (Figure 2.1A; in this figure and all others, the anterior pole of the zygote is oriented to the left). In these embryos, GFP::plastin decorates actin bundles, and dynamic assembly and disassembly of individual filaments within bundles gives rise to changes in patterns of fluorescence intensity. However, with some frequency, I could observe bright streaks of GFP::plastin that undergo rapid elongation from one end, and with a delay, undergo rapid disappearance at the other end (Figure 2.1B, 2.1C). Using kymography, I determined that these streaks elongate at the same rate as individual growing filaments, as measured with GFP::formin[17]. Because plastin presumably binds with higher avidity to bundled filaments than isolated ones, I assumed that these streaks reflect bundles formed *de novo* by two or more filaments growing simultaneously in parallel (see Supplementary Video 2.1). Kymography also revealed a characteristic delay of ~9 seconds from the appearance of the plastin signal at a given position and its subsequent disappearance (Figure 2.1B, 2.1C). Because this delay is similar to the mean lifetime of polymerized actin measured by other methods[17], I infer that the disappearance of GFP::plastin signal reflects the disassembly of actin filaments from their pointed ends.

From these observations, I inferred a simple microscopic model for turnover of actin filaments in the *C. elegans* cortex, which I call "dynamic treadmilling," and I created a custom fiber class to implement this in Cytosim (see Methods for details). In the dynamic treadmilling model, actin filaments are nucleated at a fixed rate (actin nucleation rate), they grow at a fixed rate (actin elongation rate) for a variable period of time (filament lifetime) before terminating growth,

and individual actin subunits leave the pointed end with a fixed delay (disassembly rate) after their addition to the barbed end (see Supplementary Video 2.2). Based on my experimental measurements, I set the actin elongation rate to 1.5 μm/s, and average filament lifetime to 8.5 sec. I then tuned the values of the other two parameters to reproduce the overall density and mean lengths of filaments in simulations (see below).

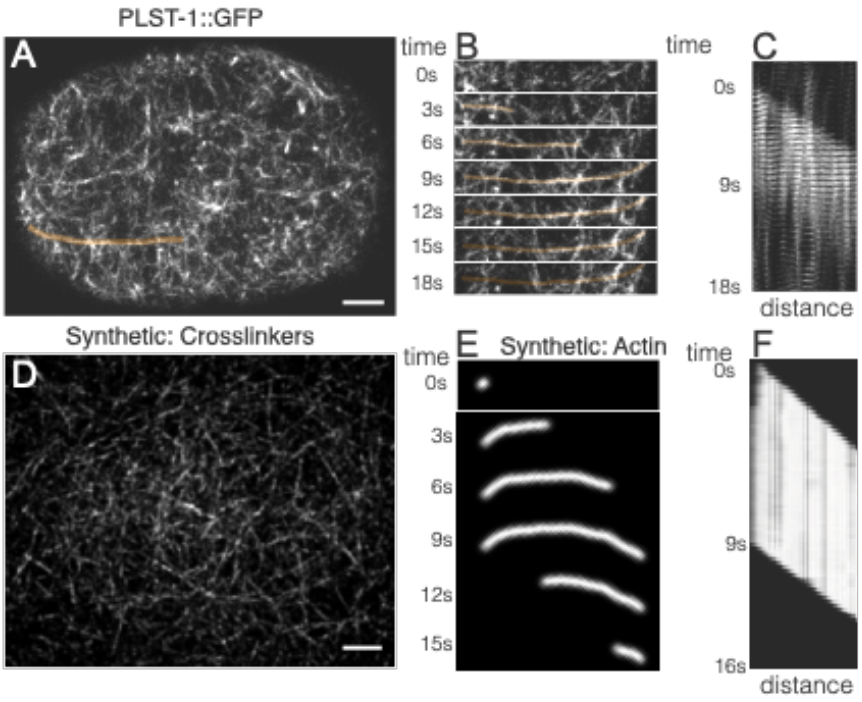

Figure 2.1: Actin filaments assemble from the barbed end for 7-9 seconds before disassembly begins at the pointed end. A: PLST::GFP labeled in one-cell *C. elegans* embryo. Streaks of plastin occur throughout the video, indicating two actin filaments assembling along one another. B: time course of plastin streak highlighted in A. C: Kymographs of 5 plastin streaks over course of video. Actin filaments assemble at a fixed rate, and disassembly begins after ~9 second delay at a fixed rate. D: Simulated image of crosslinkers in simulations. E: Simulated image of an actin filament over its lifetime. F: Kymograph of actin filament over its lifetime. Actin filament assembles at fixed rate, and disassembly begins with ~9 second delay. Scale bar: 5 μm.

To visualize my simulations, I created simulated images of a point spread function convolved with point sources at the locations of different components in simulations such as the actin filament subunits (Figure 2.1E). Looking at an actin filament over its lifetime and

corresponding kymograph demonstrates that this fiber class successfully reproduced the dynamics observed *in vivo* (Figure 2.1E-F).

2.3.2 Actin filaments preferentially assemble along existing filaments and form bundles of various sizes

Having reproduced the dynamics of isolated actin filaments, I next sought to quantify the dynamics and extent of actin filament bundling to incorporate these dynamics into my simulations. Due to the dense nature of the cortex and actin filament turnover, I do not expect bundling to occur through alignment of existing actin filaments. In previous work, Li and Munro observed that assembling actin filaments align their growth with existing filaments in a process they term "filament-guided filament assembly[17]." This, combined with the rapid filament turnover described above, provides the microscopic basis for bundle assembly dynamics.

I propose that filament-guided filament assembly is mediated by crosslinking proteins that bind elongating actin filaments fast enough to zipper them together. The major crosslinker in early *C. elegans* embryos is thought to be plastin[16]. My observation (Figure 2.1) that plastin streaks grow at the same rate as individual filaments suggests that plastin is sufficiently abundant and its rate of binding to actin filaments is sufficiently fast that plastin is the molecular zipper that mediates bundle assembly. Therefore, I incorporated a single crosslinker, modeled on plastin, into my simulations. I tuned the density and binding/unbinding rates of my crosslinker to reproduce the rapid crosslinker decoration of growing filament bundles observed for plastin and the observed dynamics of filament-guided filament assembly (see Methods for details). I found that an abundance of crosslinkers (~70/μm^2) and a fast binding rate (60 s^{-1}) was necessary to produce the filament-guided filament assembly reported by Li and Munro (Figure 2.2A). Simulated images of

crosslinkers parameterized as described above closely resemble micrographs of *C. elegans* zygotes expressing GFP::plastin (Figure 2.1D).

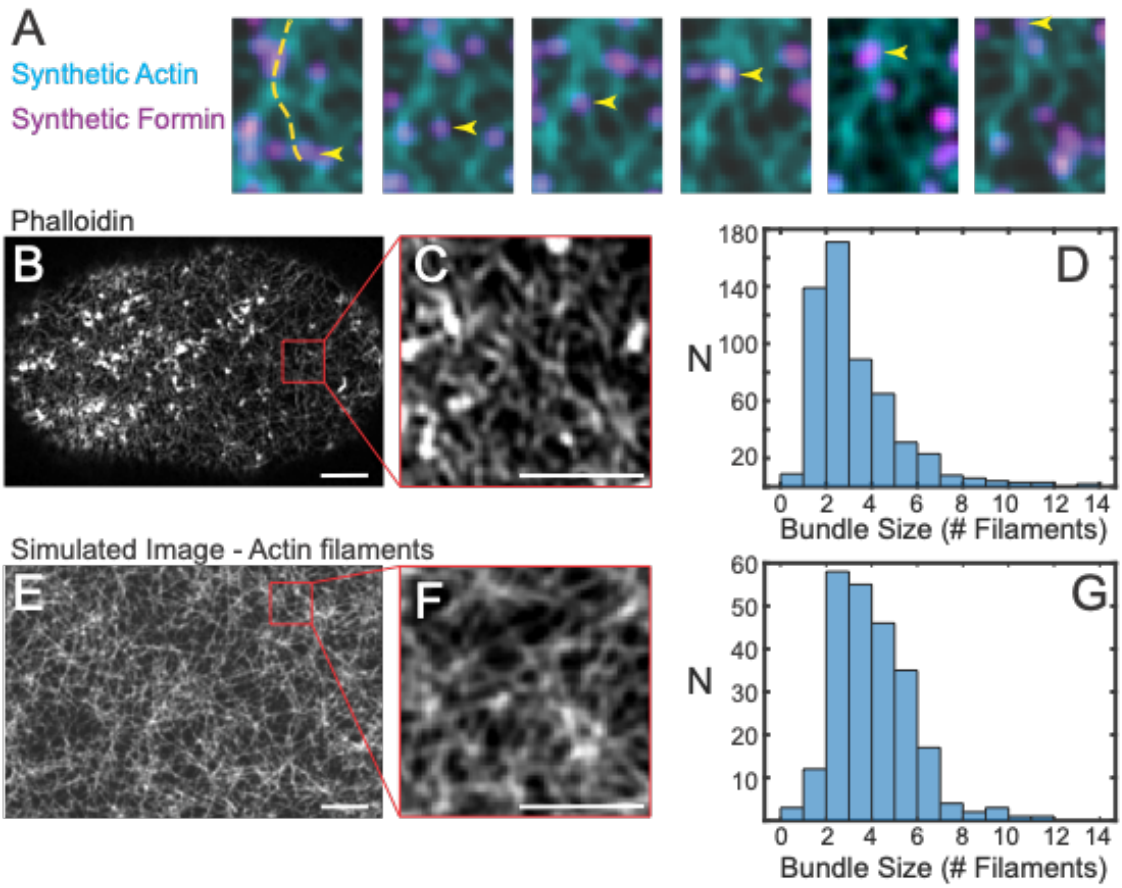

Figure 2.2: Actin filaments preferentially assemble along existing filaments and form bundles of varying sizes. A: Simulated images of actin (cyan) and formin (magenta) over time. White circle shows a formin dimer associated with an elongating filament traveling along existing actin filament. B: Phalloidin labeled in *C. elegans* embryo. C: Inset of B, highlighted in red box, showing actin filament bundles of different widths and brightness. D: Histogram of bundle sizes in experimental images. E: Simulated image of actin filaments in simulation. F: Inset of E highlighted in red box, showing actin bundles of different widths and brightness. G: Histogram of bundle sizes in simulated images. B and E: Scale bar 10 μm. C and F: Scale bar 5 μm.

Next, I wanted to quantify the overall actin bundle architecture in the cortex. I stained *C. elegans* embryos with phalloidin and imaged them using laser scanning confocal microscopy with an AiryScan detector to produce high resolution images in which I could distinguish individual actin bundles (Figure 2.2A-B). The brightness and widths of the actin bundles varied, indicating

bundles comprised of different numbers of filaments. I took transects across these bundles and calculated the bundle size distribution (see Methods for details). Assuming the dimmest transects represent a single filament (see Methods for further discussion), the peak of the distribution is ~3 filaments, and the average bundle size is 4 filaments (Figure 2.2C).

The next key parameter I wanted to constrain was the overall actin density. Since I constrain the actin filament lifetime and elongation rate with experimental measurements, the actin nucleation rate effectively determines the overall actin density in my system. I quantified actin fiber bundle size and density *in vivo*, and then tuned the nucleation rate to reproduce the experimental bundle size distribution in my simulations (see Methods for details). I created simulated images of the actin filaments in my simulations and repeated the same analysis on my simulated data over a range of actin nucleation rates (see Methods for more details). I found that the nucleation rate (121 s^{-1}) that reproduced the bundle size distribution observed *in vivo* (see Methods for details). The peak of the distribution was centered around 3-4 filaments, and the average bundle size was 6 filaments. While the average bundle size did not match perfectly, the general shape and range of the distribution matched between simulations and experiments.

2.3.3 Reproducing macroscopic flow observed during maintenance phase

My next major goal was to establish a basis for quantitative comparison of cortical flows between *in vivo* observations and simulations. As previously stated, I chose to focus on the quasi-steady-state flows that occur in polarized *C. elegans* embryos during mitosis. During this phase, a spatial gradient of myosin drives coherent flow from the posterior to anterior pole[10,12,13]. Thus, my initial goal was to quantify spatial patterns of myosin and flow during mitosis, and then use these as a basis for selecting an appropriate spatial domain, appropriate boundary conditions, and appropriate

methods for reproducing the myosin activity gradient to allow direct comparisons between experiments and simulations.

I began by using embryos expressing myosin II endogenously tagged with mKate (NMY2::mKate) to simultaneously image spatial distributions of myosin II and patterns of cortical flow during mitosis (see Figure 2.3A and Supplementary Video 2.3).

For each embryo, I selected a time window of 60-80 seconds during which myosin II densities and flow patterns were approximately steady. I calculated the myosin II intensity profile along the anterior/posterior (AP) axis (Figure 2.3B) and used QFSM to quantify the flow velocity field across the embryo by particle image velocimetry (PIV)[27] (Figure 2.3C). Because time averaged flows are aligned with the AP axis of the embryo, I averaged velocity vectors based on their distance from the boundary to the anterior domain of the embryo to construct a mean axial velocity profile (see Methods for details). In my convention, negative velocity is flow towards the anterior pole (left in figure), while positive velocity is flow towards the posterior pole (right in figure). In all embryos, I observed a characteristic pattern of myosin II distribution and cortical flow. Myosin was enriched in the anterior cortex and gradually decreased toward the posterior within a medial zone that was approximately 13 μm in width (marked by the red box in Figure 2.3A-C). Anterior-directed flows reached a maximum flow rate (i.e., were most negative) within the medial zone. In some embryos, flow reversed direction near the anterior edge of the medial zone (left edge of red box in Figure 2.3A-C); in others the speed plateaued close to zero. However, in all embryos, there was a clear inflection point in the velocity curve near the edge of the medial zone. I therefore used this inflection point to align flow profiles from multiple embryos. The flow profiles from different embryos had similar maximum flow rates and shapes (Figure 2.3D).

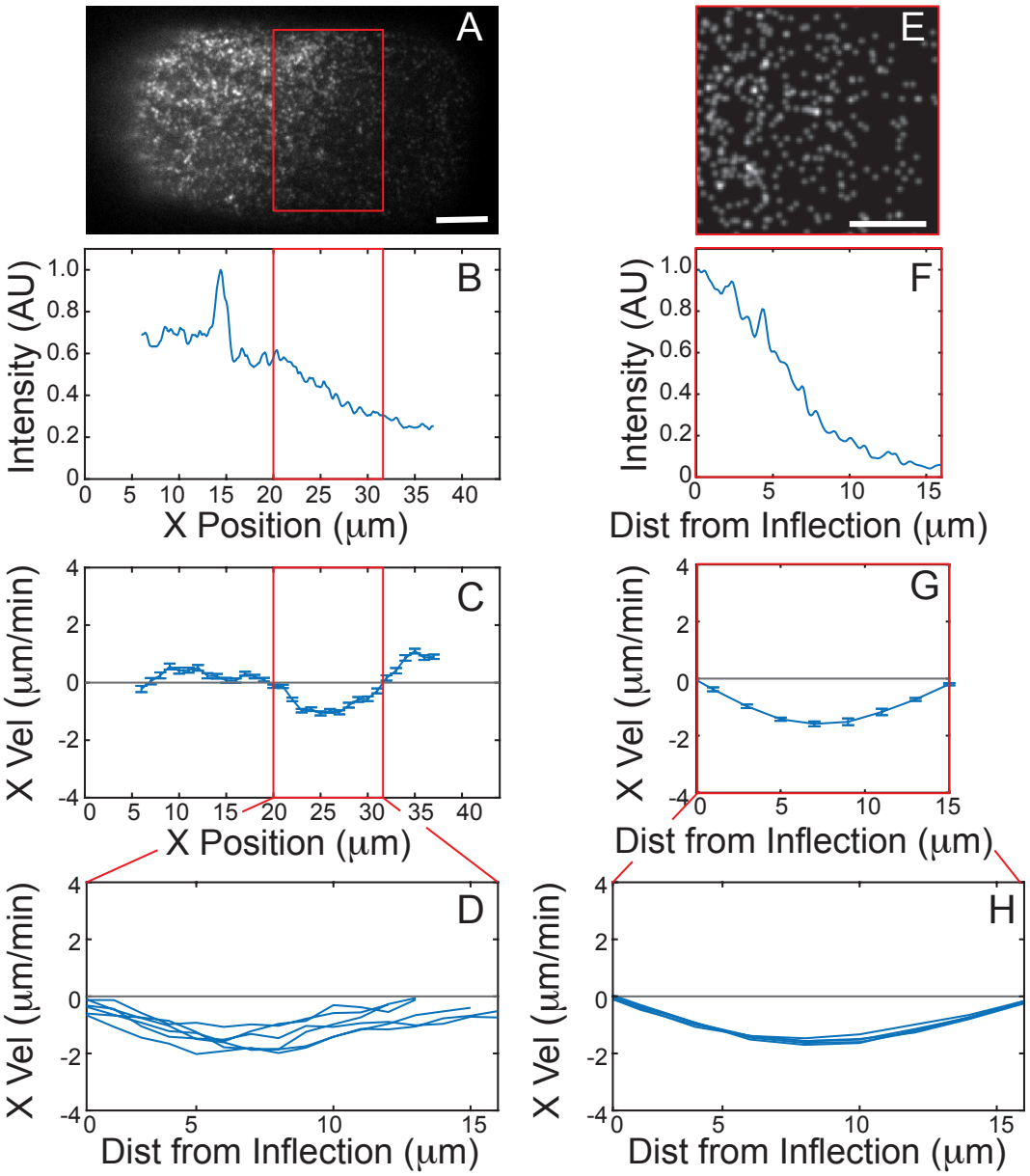

Figure 2.3: Myosin gradient drives macroscopic flow in posterior region of *C. elegans* embryo, and can be reproduced in simulations. A: Single frame of NMY2::mKate in *C. elegans* embryo during maintenance phase. B: Intensity profile of myosin along AP axis, averaged over all times in video. C: Velocity profile along AP axis, averaged over all times. Posterior region of embryo is defined by inflection point of velocity profile (shown in red box, A-C). D: Velocity profiles of posterior region of multiple embryos (N=6). E: Simulated image of myosin in simulations. F: Intensity profile of myosin in simulations, averaged over all times in video. G: Velocity profile of single simulation run (60 seconds). H: Velocity profiles of 5 separate simulations. Velocity in profiles match shape and max velocity of experimental data. Scale bar 5 μm.

Based on these observations, I chose a physical domain for my simulations corresponding to a patch of the medial zone of the embryo in which myosin forms a spatial gradient and flow speeds approach zero at either end. The Y dimension is set by the region of the embryo that is in focus during observation. I performed simulations on a mirror image duplicate of the physical domain, using a spatial distribution of myosin II with a peak at the center and periodic boundary conditions in both X and Y directions (see Methods for details). Exploiting symmetry this configuration ensured that time averaged flows vanish at the edges and the center of the simulated domain. I used only the right half of the simulations so it would directly match my experimental data.

Before establishing a myosin gradient, I selected some of the base parameters that govern myosin activity in simulations. I calculated the unloaded speed of myosin by imaging embryos expressing myosin II endogenously tagged with mKate (NMY2::mKate) at a fast frame rate. I identified myosin speckles that appeared to be undergoing ballistic motion, then calculated their velocity using kymography. The average myosin II unloaded speed was 0.3 μm/s. I estimated the stall force by multiplying the average number of myosin heads in a minifilament (10-20)[28] with the stall force of a single myosin motor (~3.4 pN)[29] and set the stall force to 45 pN.

Next, I tested how best to capture the myosin gradient observed in simulations. I initialized the center of the simulation space with a higher density of myosin. Throughout the simulation, I added and deleted myosin from the system to replicate turnover. The myosin gradient and cortical flows were controlled by three key parameters: the base myosin addition rate, activity ratio between the center and periphery of the simulations, and the number of motors in the system (see Methods for details). I tuned these three parameters to produce myosin gradients and patterns of flow.

I selected a base addition rate, activity ratio, and myosin density that produced a clear myosin gradient and patterns of cortical flow. I created simulated images of myosin in the simulations and quantified the myosin gradient (Figure 2.3E-F) and observed that the myosin density is high in the left and decreases when approaching the right as expected. My simulations also produced a clear pattern of cortical flow (see Supplementary Video 2.4), and the magnitude and overall flow profile matched my experimental observations (Figure 2.3G-H).

Altogether, these results show that a model in which many of the key physical parameters that govern microscopic network dynamics are constrained can reproduce the observed dynamics of cortical flow in *C. elegans* embryos. This empirically grounded model provided us with a rigorously characterized setup in which I could perturb the microscopic properties of the cortex in experiments and simulations and compare the two.

See Table 2.1 on the following page for a detailed list of key parameters in the simulations and a description of how these parameters were chosen.

	Value	Source/citation
System		
Size	32 μm x 20 μm	Measured from size of posterior in *C. elegans* embryos
Boundary Conditions	Periodic	Chosen based on properties of experimental region of interest
kT	0.0042 pN/μm	Thermal energy at 25° C
Viscosity	1 pN s/μm^2	Ref 36
Actin filaments		
Actin filament rigidity	0.075 pN/ μm^2	Ref 36
Actin filament segmentation	0.2 μm	Computational parameter, recommended by Cytosim guidelines, Ref 36
Actin filament assembly/disassembly speed	1.5 μm/s	Ref 17
Crosslinkers		
Binding Rate	60 s^{-1}	Optimized to reproduce filament-guided filament assembly
Unbinding Rate	0.05 s^{-1}	Ref 16
Binding Range	10 nm	Ref 16, 35
Diffusion	10 μm^2 /s	Ref 16
Stiffness	250 pN/μm	Ref 16, 35
Motors		
Binding Rate	5 s^{-1}	Ref 16
Unbinding Rate	0.15 s^{-1}	Ref 16
Binding Range	10 nm	Ref 16, 35
Diffusion	10 μm^2 /s	Ref 16
Stiffness	250 pN/μm	Ref 16, 35
Unloaded Speed	0.3 μm/s	Measured speed of myosin minifilaments undergoing ballistic motion
Stall Force	45 pN	Calculated from Ref 28, 29

Table 2.1: Simulation parameters and their sources.

2.3.4 Perturbing microscopic properties of the cortex in experiments alters the macroscopic patterns of cortical flow

I next sought to test the predictive abilities of the parameterized model. To this end, I used RNAi to deplete the expression of proteins that regulate actin binding and actin assembly dynamics and

developed methods to quantify the strength of the level of depletion in individual embryos. This allows us to construct "dose response" curves, or tuning curves in which I plot quantitative measures of cortical contractility and flow relative to the degree of depletion. This strategy allows us to make a strong comparison to models, which was not previously possible.

I focused on three perturbations that I expected to affect cortical flow. First, I perturbed crosslinker density by depleting levels of plastin. I measured the average plastin intensity during maintenance phase as a measure of the depletion; the average intensity decreased at higher levels of depletion. Next, I reduced actin filament nucleation by depleting levels of formin. I imaged formin in the two-cell zygote and calculated the number of formin speckles detected during mitosis (see Methods). I used the decrease in the density of formin speckles as a proxy for decreasing the rate of actin filament nucleation. Finally, I slowed the actin elongation rate by depleting levels of profilin. I collected streaming data for labelled formin during mitosis in the 2-cell zygote and used particle tracking to directly calculate the actin elongation rate (see Methods). These calculations are explained in more detail in the Methods.

Previous studies report that perturbing crosslinker density, actin nucleation rate, and actin elongation rate affect the connectivity of the network and thus both its ability to transmit force and resist deformation[1,16,20,22,24,30]. However, they do so in different ways. The crosslinker density directly affects the connectivity, while the actin filament nucleation rate and elongation rate affect it through the overall actin density; the actin elongation rate also changes the average filament length in the system. Thus, I expect these three perturbations to affect the balance of force transmission and resist to deformation (and thus overall flow) in different ways.

I illustrate the effects of the depletions through kymographs across the posterior region in Figure 2.4 (see also Supplementary Videos 2.5-10). Throughout the figure, yellow arrows are

meant to guide the eye to show rates of anterior-directed flow in the embryo, which are captured by diagonal streaks in the kymographs. Blue arrows highlight local fluctuations, which are captured by curved lines, or sharp turns in the streaks.

Intermediate depletion of plastin, formin, and profilin caused increases in the rates of anterior directed flow (Figure 2.4B-D highlighted by yellow arrows). For stronger perturbations, I observed a more complicated response in which flows lose coherence; there are more local fluctuations in the velocity field which correspond with local tearing in the cortex (Figure 2.4B-D, highlighted by blue triangles). This was especially evident in the profilin depletions, and to a lesser extent in the formin depletions. In the moderate and strong formin depletions, there were sharp turns in isolated locations of the kymograph, which indicates local tearing. In contrast, strong profilin depletions produced sharp turns that spanned large regions, which indicates tearing on a much larger scale (see Supplementary Videos 2.9 and 2.10).

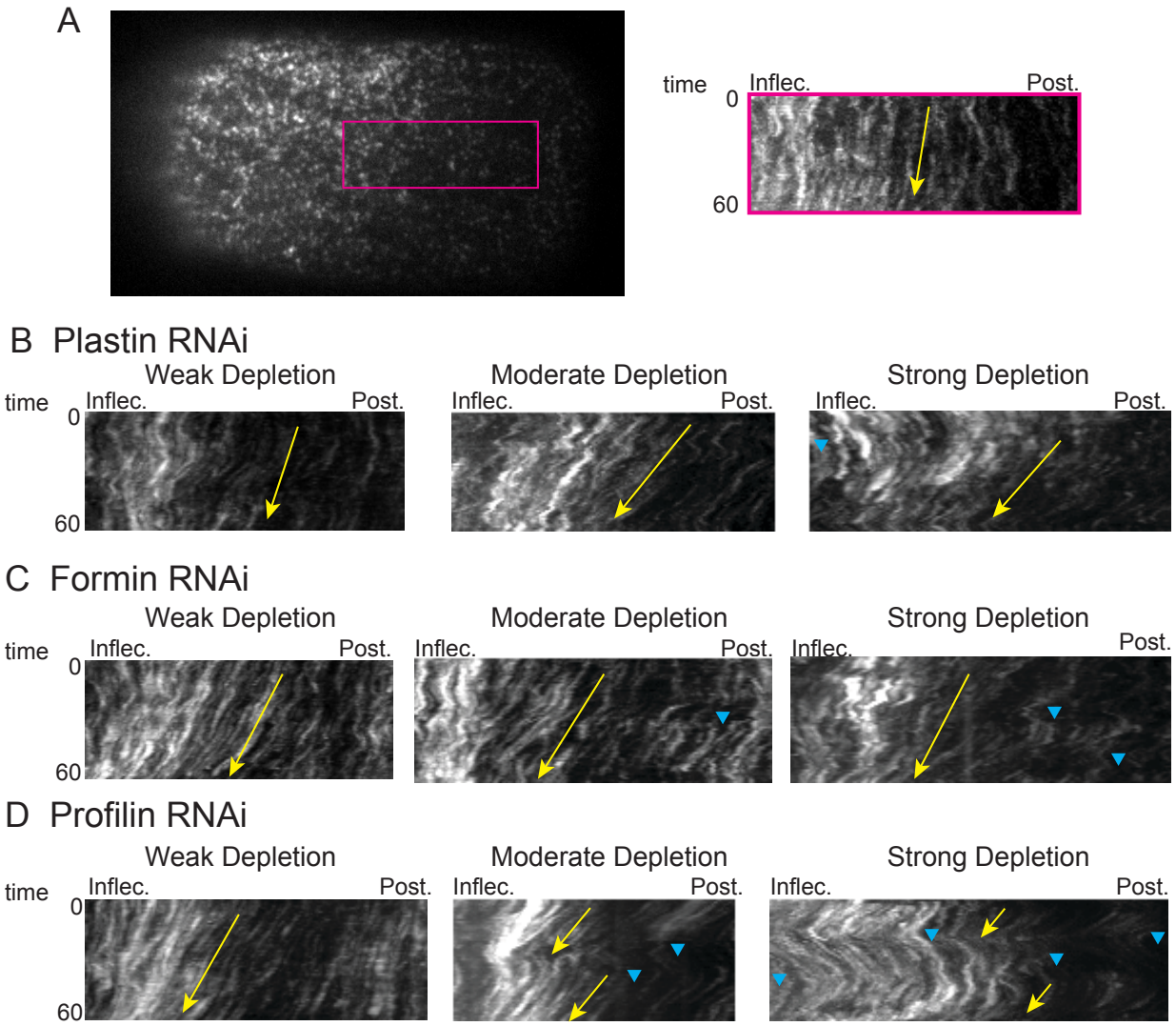

Figure 2.4: Depleting plastin, formin, and profilin alters patterns of macroscopic flow in distinct ways. A: NMY2::GFP in *C. elegans* embryo maintenance phase. Pink box shows area used to create kymograph shown to the right. Kymographs of weak (left), moderate (middle), and strong (right) depletions for plastin (B), formin (C), and profilin (D) displayed. Yellow arrows highlight flow towards anterior pole. Blue arrows highlight local fluctuations in cortical flows.

2.3.5 Simulations predict changes in maximum flow rate in response to perturbing crosslinker

I first sought to quantify and compare the coherent anterior-directed cortical flows between simulations and experiments. My experimental set up provided us a simple way to construct "dose response" curves and plot a metric of flow with respect to different levels of depletion. I used the maximum time-averaged axial flow rate to quantify coherent cortical flows. To measure this

maximum flow rate, I examined the experimental and simulated axial velocity profiles described in Figure 2.3C-D and 2.3G-H. The maximum flow rate is the absolute value of the point at which the axial flow is the fastest towards the anterior (most negative).

In my simulations, decreasing the crosslinker density, actin nucleation rate, and actin elongation rate all caused the maximum flow rate to increase at moderate depletions, then decrease at extreme depletions (Figure 2.5, A,C,E respectively; yellow markers represent conditions used in my standard simulations, and purple represent conditions that have been perturbed). The maximum flow rate had different level of sensitivity for each perturbation. Decreasing the crosslinker density caused the maximum flow rate to slowly increase, then decrease when the density was below 30% its standard setting (Figure 2.5A). In contrast, the maximum flow rate did not increase until the actin nucleation rate was below 40% its original value and did not decrease until it was below 20% its original value (Figure 2.5C). The maximum flow rate was quite sensitive to the actin elongation rate; it quickly increases at mild depletions, and when the elongation rate was below 0.75 μm/s (half of the standard value), the max flow rate decreased (Figure 2.5E).

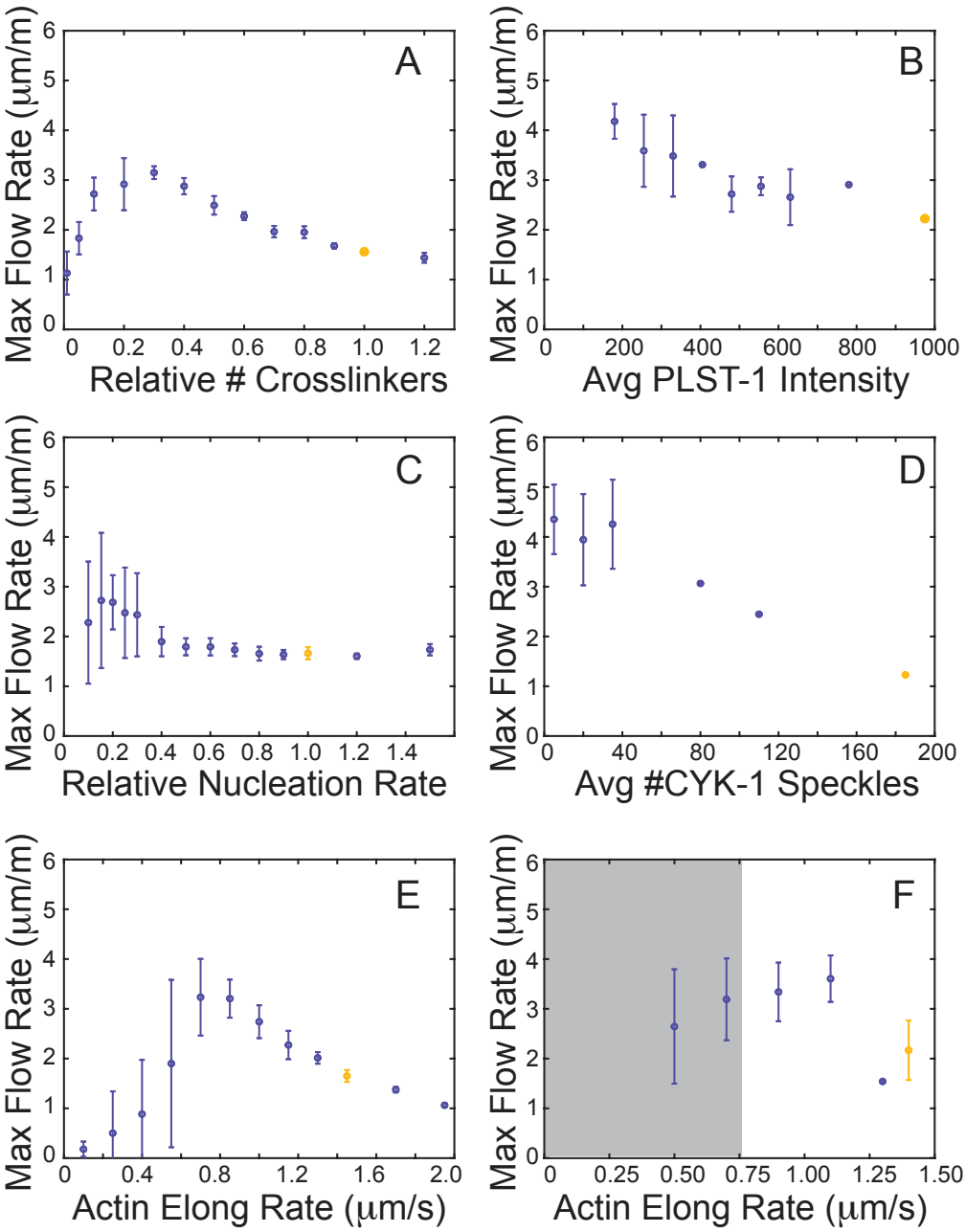

Figure 2.5: Simulations accurately predict changes in maximum flow rate in response to perturbing plastin, formin, and profilin. Maximum flow rate was calculated for a single condition by taking absolute value of the fastest point along the velocity profile. In simulations, maximum flow rate was averaged across 5 simulations. In experiments, maximum flow rate was calculated for a single embryo, then averaged based on depletion level. Maximum flow rate for simulations (left) and experiments (right) was calculated for perturbing crosslinker density (A,B), actin nucleation rate (C,D), and actin elongation rate (E,F). Yellow denotes wild type conditions in experiments, and standard settings in simulations. Figure 2.5 Continued (pg. 48)

Figure 2.5 Continued. Purple represents simulations in which the actin density was variable, and pink represents simulations in which the actin density was held constant. Gray box in F denotes where measurements of actin elongation rate are less reliable due to network tearing.

Depleting plastin, formin, and profilin produced clear trends in the maximum flow rate. I calculated the maximum flow rate for each embryo and plotted it against the depletion strength (Figure 2.5, right column; yellow markers represent wild type data, purple markers represent RNAi experiments). For plastin and formin depletions, the maximum flow rate increased with stronger depletion levels (Figure 2.5B,D respectively). At weak profilin depletions, the maximum flow rate also increased (Figure 2.5F). When the actin elongation rate was below 0.75 μm/s, the cortex underwent major local tearing, which makes it difficult to precisely measure the actin elongation rate. However, it does appear that the maximum flow rate begins to decrease at these slow actin elongation rates (Figure 2.5F). Notably, local fluctuations begin to dominate system dynamics when the elongation rate is ~0.75 μm/s in both experiments and simulations. Overall, my simulations produce accurate predictions of the trends in maximum flow rate for each depletion experiment. The precise trends were different between my three perturbations, and the simulations detected and predicted these differences.

2.3.6 The velocity magnitude changes in response to decreasing crosslinker density, actin nucleation rate, and the actin elongation rate

Some embryos undergoing strong depletions had rapid fluctuations in the velocity field that were not parallel to the AP axis, and thus could be averaged out when calculating the maximum axial flow rate. The underlying velocity magnitude can be used as a proxy for loss of coherent flow and the presence of local tearing. When tearing is present, I expect the average velocity magnitude to increase. Therefore, I calculated the average magnitude of the velocity vectors using PIV for each

condition in experiments. In simulations, I constructed a corresponding velocity field by averaging the velocity in a given region, and then found the magnitude of these averaged velocity vectors.

The trends in the maximum flow rate and the velocity magnitude were distinct from one another in simulations. Decreasing the crosslinker density and actin nucleation rate caused the velocity magnitude to increase (Figure 2.6A,C). For the crosslinker density, the trend seemed to be approximately the same regardless of the level of depletion. However, when the actin nucleation rate was below 40% of its original value, the velocity magnitude drastically increased. In contrast, decreasing the actin elongation rate caused the velocity magnitude to slowly increase when the elongation rate was above 0.9 μm/s, increase more quickly when the elongation rate was between 0.75-0.9 μm/s, and then decrease when it was below 0.75 μm/s (Figure 2.6E).

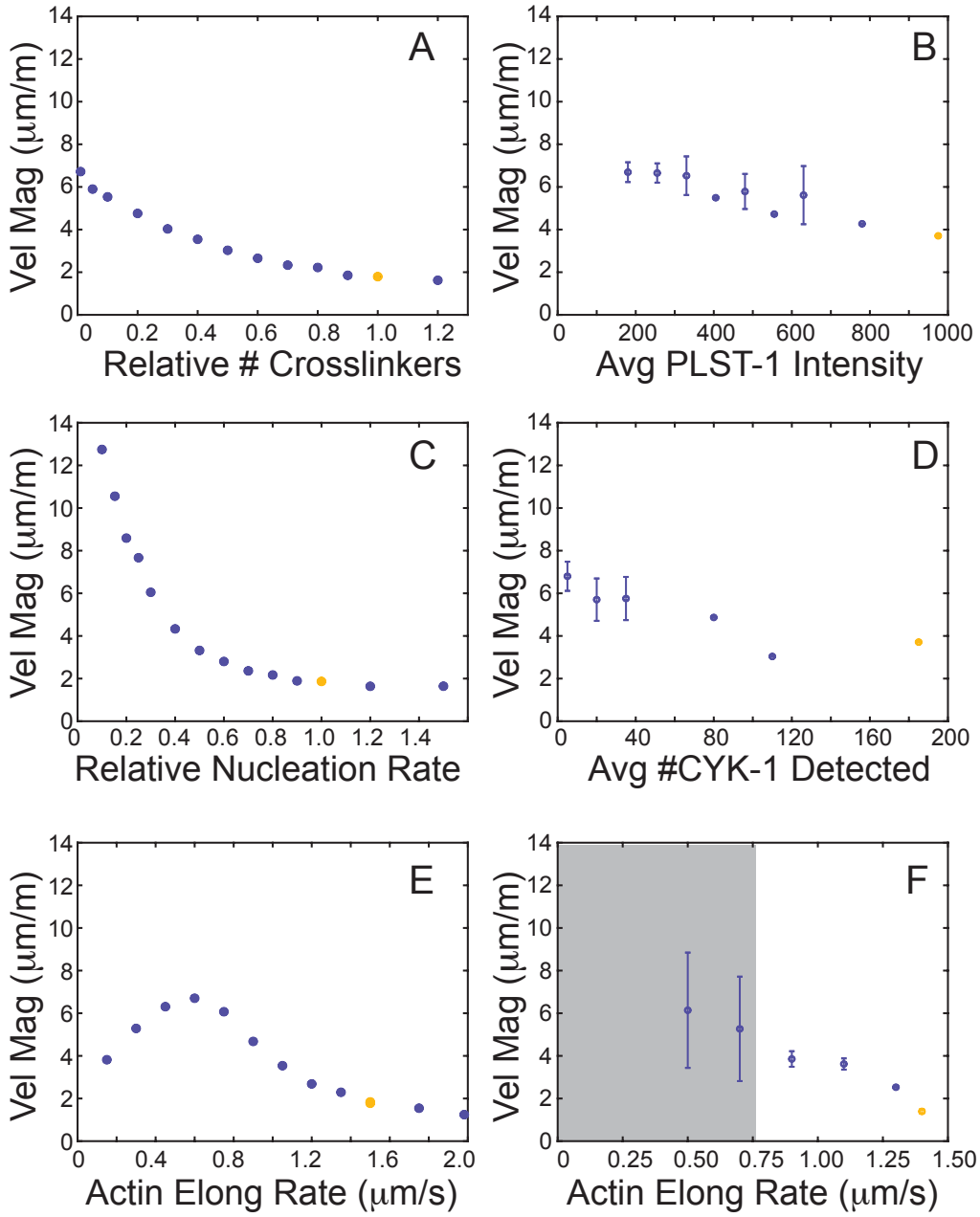

Figure 2.6: Simulations accurately predict changes in average velocity magnitude of PIV field changes in response to decreasing crosslinker density, actin nucleation rate, and actin elongation rate. Average velocity magnitude in simulations (left), and experiments (right) for crosslinker density (A,B), nucleation rate (C,D), and actin elongation rate (E,F). In simulations, the velocity magnitude was averaged across 5 simulations. In experiments, the velocity magnitude was calculated for a single embryo, then averaged based on depletion level. Yellow denotes wild type conditions in experiments, and standard settings in simulations. Figure 2.6 Continued (pg. 51)

Figure 2.6 Continued. Purple represents simulations in which the actin density was variable, and pink represents simulations in which the actin density was held constant. Gray box in F denotes where measurements of actin elongation rate are less reliable due to network tearing.

In experiments, depleting plastin and formin produced similar results; the velocity magnitude slowly increased at increasing depletion strengths, and there were not any major changes in the trends (Figure 2.6B,D). In the formin RNAi experiments, I do not see the sharp increase in velocity magnitude that I observe in simulations. Weak depletions of profilin caused the velocity magnitude to slowly increase. When the actin elongation rate was below 0.75 μm/s, the velocity magnitude drastically increased (Figure 2.6F). My simulations accurately predicted changes in velocity magnitude in response to perturbing the crosslinker density, actin nucleation rate, and actin elongation rate, and the trends for each perturbation were distinct from one another.

2.4 Discussion

The cortex is regulated by a balance of active force and internal resistance to deformations. Interactions between actin, crosslinkers, and motors control this balance and have major effects on cortical flows[16,23,25,30]. Each component of the cortex can contribute to active force, internal resistance, or both[1,2,20]. Understanding how macroscopic patterns of flow are affected by proteins that microscopically regulate the cortex is an ongoing challenge. Here, I explore how properties of the microscopic components of the cell cortex tune cortical flows in polarized single-cell *C. elegans* embryos.

In the first phase of the project, I quantified microscopic properties of the *C. elegans* cortex and used these to constrain my Cytosim simulations. First, I identified that actin filaments undergo dynamic treadmilling and this governs actin filament assembly/disassembly dynamics. I created a custom fiber class in Cytosim that reproduces this behavior. I also characterized actin filament

bundling dynamics and bundle sizes and tuned the crosslinker properties and actin density in the system to reproduce these behaviors in simulations.

The last step in tuning my simulations was tuning the myosin dynamics until I successfully reproduced the myosin gradient and patterns of flow observed *in vivo*. I did so by initializing the simulation space with an increased myosin density and enforcing a faster addition rate of myosin in the center of the simulation than at the periphery. This maintained a gradient of myosin through the space. I compared the velocity profiles in my experiments and simulations and found that they closely agreed.

My results show that incorporating experimentally measured parameters of actin filament assembly/lifetime, crosslinkers, and motors in simulations is sufficient to reproduce the cortical flows observed *in vivo*. This demonstrates that these cortical flows are dominated by the network structure and dynamics and that other features (e.g., hydrodynamics) are not needed to account for the observed flows. This was a significant accomplishment in my research and provided confidence that my simulations accurately reflected the experimental system.

In the second phase of my project, I sought to quantify the effects of perturbing microscopic properties of the system on the cortical flows. I used my simulations to predict the responses in cortical flows, and then compared these predictions to my experiments. I focused on perturbing the crosslinker density, actin nucleation rate, and actin elongation rate because they are known to affect the macroscopic properties of the cortex in complex ways. In experiments, I completed RNAi experiments to deplete the expression of plastin, formin, and profilin respectively and quantified the level of depletion for each embryo. This allowed us to construct “dose response” curves to determine how cortical flows are affected by a range of depletion levels and directly compare my experimental results with my simulations.

Qualitatively, depleting plastin, formin, and profilin altered the cortical flows observed during maintenance phase. Intermediate depletions of each protein increased the rate of cortical flow. Strong depletions of formin and profilin produce network tearing, characterized by rapid fluctuations in the velocity field. At very strong profilin depletion levels, the cortical dynamics were dominated by local fluctuations.

I quantified the maximum flow rate to assess how perturbing the crosslinker density, actin nucleation rate, and actin elongation rate affect coherent cortical flows. My simulations predicted a biphasic response for altering these three properties. At intermediate depletion levels, the maximum flow rate increased and at high depletion levels, the maximum flow rate decreased. The sensitivity to each perturbation varied. In my corresponding experiments, I depleted plastin, formin, and profilin using RNAi and calculated the maximum flow rate and compared it with the level of depletion for each embryo. My simulations accurately predicted the experimental trends for each perturbation. One of the most striking similarities comes from comparing simulations and experiments that alter the actin elongation rate. In simulations, the maximum flow initially increases, and when the actin elongation rate is below 0.75 μm/s, local tearing dominates the network. In experiments I see the same trend, and the same inflection point. This demonstrates that my simulations are predicting both the trends and the sensitivity to perturbations that I conduct experimentally.

Qualitatively, depleting formin and profilin produced local tearing, which is characterized by fast velocity vectors that are not always along the AP axis. So, I calculated the velocity magnitude to quantify the emergence of these fast, incoherent motions. I predict that increased local fluctuations will result in an increased velocity magnitude. My simulations predicted quite distinct changes in the velocity magnitude in response to depleting the crosslinker density, actin

nucleation rate, and actin elongation rate. Depleting the crosslinker density slowly and steadily increased the velocity magnitude. Lowering the actin nucleation rate initially slowly increased the velocity magnitude, and when the nucleation rate was less than 40% of the original, the velocity magnitude rapidly increased. Slowing the actin elongation rate initially slowly increased the velocity magnitude, rapidly increased it when the rate was below 0.9 μm/s, then rapidly decreased when the elongation rate was below 0.75 μm/s. In my experiments, depleting plastin and formin slowly increased the velocity magnitude. Depleting profilin slowly increased the velocity magnitude until the actin elongation rate was below 0.75 μm/s at which point the velocity magnitude rapidly increased.

While my simulations generally accurately predict trends resulting from my perturbations, my plastin and formin depletion experiments do not exhibit the behavior simulations predict at very strong depletion levels. I hypothesize that this discrepancy is because I have not depleted plastin and formin experimentally to the extent that I am able to do so in simulations. Plastin is not the only crosslinker in the *C. elegans* cortex, so it is possible that an incredibly strong plastin depletion would still have a significant amount of crosslinking in the system. Since the actin nucleation rate has a major role in determining the actin density in the system, it is possible that I cannot deplete the formin much further without killing the embryo.

There is a biphasic dependence of flow speeds based on the expression of plastin, formin, and profilin. I suggest that each of these perturbations affect the connectivity of the cortex, which in turn affects both force transmission and resistance to deformation. Mild depletions reduce resistance to an extent that leads to increased flows. This is observed in the increase in the maximum flow rate and the velocity magnitude. More extreme depletions reduce connectivity to

the point that force transmission, and thus cortical flows, ultimately fail. I see this level of depletion in all of my simulations, and in my experimental profilin depletion data.

Comparing the effects of the formin and profilin depletions suggests some interesting insights to how forces are propagated through the cortex. Both perturbations affect actin assembly dynamics and the overall actin density in the cortex. Depleting formin in simulations and experiments qualitatively increases local contractions and tearing. Depleting profilin in simulations and experiments drastically increases contractions – both local and over large spatial scales – and network tearing. Thus, it appears that altering the actin elongation rate affects the connectivity and ability for forces to propagate through the network more than altering the actin nucleation rate. This may be partially related to the average filament length, which decreases in response to decreasing the actin filament elongation rate but does not change in response to decreasing the actin nucleation rate. I hypothesize that when the cortex is comprised of shorter actin filaments, force is not able to propagate as well through the system.

There are several key take aways from this work. I demonstrate that tightly constraining agent-based simulations with measurements of the microscopic properties of a biological system can produce cortical flows. Additionally, these simulations accurately predict the responses to altering different microscopic properties of the cortex. The simulations also pick up on subtleties between different perturbations, particularly at extreme depletion levels that may not be accessible experimentally. Furthermore, I demonstrate that crosslinking and actin filament assembly/lifetime regulators affect cortical flows in complex ways. It appears as though these perturbations affect both force transmission and resistance to deformations in the cortex. These two effects are difficult to disentangle, but this is a promising platform to further purse how microscopic properties of the cortex affect cortical flow in the future.

2.5 Methods

Experimental Models and Subject Details

I cultured *C. elegans* strains under standard conditions[31] on 60 mm plates containing OP50 on normal growth medium. All strains were cultured at 20-22 °C. See Table 2.1 for a list of worm strains used in this study.

Strain Name	Description	Genotype
EM319	NMYII::mKate, LifeAct::mCherry	NMY-2(cp52[NMY-2::mkate2 + LoxP unc-119(+) LoxP]) I; unc-119(ed3) III;mgSi3[cb-UNC-119 (+) GFP::UtrophinABD]II
EM394	NMYII:mKate, PLST-1::GFP	plst-1(msn190[plst-1::GFP]) IV; NMY-2(cp52[NMY-2::mkate2 + LoxP unc-119(+) LoxP]) I;
EM460	NMYII:mKate, CYK-1::GFP	him-8(e1489) IV; NMY-2(cp52[NMY-2::mkate2 + LoxP unc-119(+) LoxP]) I; cyk-1 (knu83 C-terminal GFP, unc-119 (+));
EM365	LifeAct::mCherry, PLST-1::GFP	plst-1(msn190[plst-1::GFP]) IV; zbIs2[pie-1::Life::mCherry, unc-119(+)];
EM342	LifeAct::mCherry, PLST-1::GFP	cyk-1 (knu83 C-terminal GFP, unc-119 (+)); zbIs2[pie-1::Life::mCherry, unc-119(+)];

Table 2.2: *C. elegans* strains used in experiments.

Phalloidin Staining

We fixed embryos and stained them following the protocol described in Willis et al., 2006[32]. Briefly, we raised embryos to the L4 stage, then used the bleaching technique[33] to release the eggs. We then rinsed the eggs in egg salts, and fixed them in 3% formaldehyde and rinsed them briefly three times in PBS with 0.1% Triton-X (PBT), and then stained them for one hour at room temperature with Bodipy fl-phallicidin (Molecular Probes), at 1 U/200 µl in PBT. We then rinsed

embryos in PBS, and mounted them on coverslips and allowed them to cure for >24 hours before imaging.

AiryScan Microscopy

Images were acquired using a point scanning confocal microscope (Zeiss Airyscan LS980) with a laser line at 491 and suitable emission filter. A 40x oil immersion objective was used. Laser power and exposure were adjusted to optimize signal. Z-stacks across the cortex, with a step of 0.16 μm were acquired for each embryo.

RNAi

I used the previously established feeding method[34] to perform RNAi experiments. I obtained bacteria targeting GFP, formin (CYK-1), and profilin (PFN-1). I grew bacteria in LB with 50 ug/ml ampicillin, then seeded the culture on NGM plates with 1 mM IPTG. I incubated plates for ~36 hours, and then stored them at 4˚ C for up to ten days before use. Prior to imaging, I transferred L4 larvae to RNAi plates and cultured them at room temperature. See Table 2.2 for the ranges of incubation times for each RNAi experiment.

Note: I did not have a well-characterized plastin RNAi strain. Instead, I used a strain that endogenously labeled plastin with GFP and used GFP RNAi depletion expression. I verified the depletion by quantifying the overall plastin signal in the cortex and observed that the intensity of the signal decreased in response to longer feeding times.

Target gene	**RNAi strain**	**Incubation time**
Plastin	GFP-RNAi	28-40 hours
Formin	CYK-1 RNAi	18-30 hours
Profilin	PFN-1 RNAi	12-24 hours

Table 2.3: Details of RNAi experiments.

TIRF Microscopy

For two-color imaging of F-actin (GFP::UTR) and myosin (NMY-2::mKate2) or CYK-1 (CYK-1::GFP and F-actin (Lifeact::mCherry), we used a Nikon Ti-E inverted microscope equipped with solid state 50mW 481 and 561 Sapphire lasers (Coherent), a TIRF illuminator, and a Ti-ND6-PFS Perfect Focus unit. A laser merge module (Spectral Applied Research; LMM5) equipped with an acousto-optical tunable filter (AOTF) allowed rapid (1-2 msec) switching between excitation wavelengths. We collected near TIRF images using a CFI Apo 1.45 NA oil immersion TIRF objective, onto a PRIME 95B CMOS camera, yielding a pixel size of ~107nm. Image acquisition was controlled by Metamorph software.

For single molecule/single particle tracking analysis of actin::GFP or CYK-1::GFP, we used an Olympus IX50 inverted microscope equipped with an Olympus OMAC two-color TIRF illumination system, a CRISP autofocus module (Applied Scientific Instrumentation), and a 1.45 NA oil immersion TIRF objective. Laser illumination at 488 nm from a 50-mW solid-state Sapphire laser (Coherent) was delivered by fiber optics to the TIRF illuminator. Images were magnified by 1.6x and collected on an Andor iXon3 897 EMCCD camera, yielding a pixel size of 100 nm. Image acquisition was controlled by Andor IQ software.

For all experiments, we set the laser illumination angle to a standard value that was chosen empirically to approximately maximize signal-to-noise ratio while maintaining approximately even illumination across the field of view. Further details of the imaging conditions used for specific quantitative analyses are provided below.

For timelapse imaging, images were collected at 1 frame per second, with an exposure of 200 msec per image. Laser power was set to 30%. The Digitizer was 16 MHZ, and the Gain was set automatically. For streaming data of CYK-1, images were collected as 20 frames per second,

with an exposure of 50 msec. The Digitizer was 12 MHZ, and the Gain was set automatically.

Simulated Images

To create simulated images, I performed rough calculations to estimate the point spread function of different labels and imaging conditions (ex. phalloidin-stained actin filaments visualized AiryScan microscopy vs myosin visualized with TIRF). I then picked the corresponding simulation component of interest, and convolved this point spread function on the location of these components (ex. convolve point spread function at the location of every bound crosslinker in the system). This allowed us to compare simulations and experiments more closely and run the same analysis methods for simulations and experiments.

Plastin Streak Analysis

We collected a sequence of images from embryos expressing PLST-1::GFP on the Olympus TIRF microscope with 30% laser power and 100 msec exposures. We manually identified individual events in which bright streaks of PLST-1 fluorescence could be observed to grow and then disappear. In FIJI, we used maximum intensity projections to identify the path of the growing streak; we used the Straighten plugin (https://imagej.net/plugins/straighten) to extract a linear pixel array of width 5 pixels along the path for each frame of the image sequence, and converted the resulting image stack into a kymograph for analysis.

Bundle Size Analysis

I drew large scans across the images and identified peaks, which acted as candidates for actin bundles. For each candidate bundle, I took a small transect spanning the fiber and produced intensity profiles.

To be considered a valid candidate, the transect profile had to meet the following criteria: there must be a single peak in the profile, the peak intensity must be above a certain threshold, and the minima on the left and right of the peak must be below 70% of the peak intensity. I then found the integrated intensity of the transect profiles between the left and right minima. The smallest integrated intensity corresponded with the transect that was perpendicular to the bundle. I used this value to compare the bundle sizes.

I hand-identified the smallest and dimmest filaments in the image and considered these a single filament. I calculated the integrated intensity for these peaks and used this value to normalize the distribution of integrated intensities. It is important to note that I cannot be certain that these dim fibers are in fact single filaments; it is possible that these fibers are the smallest detectable bundle size, which could be more than one filament.

For simulations, I produced simulated images of the actin filaments and repeated this same analysis on those simulated images. To normalize the bundle size distribution, I created images of a single filament and found the integrated intensity. In this case, I can be certain that I was normalizing to a single filament.

Identifying Maintenance Phase

I made kymographs across the AP axis of the embryos spanning the entire 1-cell stage. The window of maintenance phase was identified based on enrichment of myosin in the anterior of the embryo, and the presence of anterior-directed cortical flows in the posterior region. I then selected a 60-80 second time span within this window, taking care to avoid the end of polarization establishment and onset of cytokinesis.

QFSM

I used QFSM software to calculate the PIV field[27] from myosin::mKate labeled in *C. elegans* embryos. Briefly, I selected a small region outside of the cortex to determine the background level. I only considered videos in which the Gaussian ratio of the signal to noise was greater than 2.4 to ensure that my measurements were robust. I then manually set a threshold of the intensity signal to consider. QFSM creates a mask based off this value and only calculates the PIV field within this video. I then ran the speckle detection and speckle tracking using standard settings.

Identifying medial boundary

Myosin is enriched in the anterior region of the embryo during maintenance phase and there was a clear boundary between the domains. However, this boundary was occasionally at an angle rather than precisely perpendicular to the AP axis. Additionally, the boundary occasionally moved during maintenance phase, particularly in embryos undergoing strong depletions. Therefore, I manually identified the location and angle of the boundary. I adjusted the boundary details every ten seconds when necessary.

Flow Rate Profiles in Experiments

I sought to quantify the flow along the AP axis in the *C. elegans* embryos during maintenance phased. To produce clear flow profiles, I needed to calculate the flow profile with respect to the boundary between the anterior and medial region. For each velocity vector, I calculated the distance along the AP axis to the closest point on the boundary. I then aligned the velocity vectors based on their distance from the anterior/posterior boundary. I divided the embryo into 1 μm bins along the AP axis and calculated the average velocity in that bin over all times.

Next, I wanted to focus on the posterior regions of the embryos rather than the entire profile. The flow profile was generally positive (directed towards the posterior) at the posterior pole, but then became negative (directed towards the anterior) across the posterior region. At the boundary between the posterior and medial region, the flow then became zero, or positive. I selected the region in this flow profile that had anterior-directed flow. There were some cases that the flow did not before posterior-directed at the medial region, but there was always an inflection point in the flow profiles. So, I used the inflection points to define the medial boundary when necessary.

Flow Rate Profiles in Simulations

I used crosslinkers as markers for the velocity, only considering crosslinkers that were bound to the same actin filament in two consecutive frames. I calculated the velocity of each crosslinker between frames over the course of the simulation. Then, I divided the simulation space into 1 μm bins along the X axis and calculated the average velocity in that bin over all times.

Max Flow Rate

I located the position at which the flow rate was the fastest towards the anterior. I defined the maximum flow rate to be the absolute value of the flow at this location.

Velocity Magnitude

In experiments, I simply calculated the magnitude of the velocity vectors and took the average. In simulations, I constructed a regularly spaced velocity field over the simulation space. I divided the

simulations into 1 μm x 1 μm squares and averaged all of the velocity vectors within that square at a given time. I then used this velocity field to calculate the average magnitude of the velocity vectors.

Quantifying RNAi depletion strength of plastin, formin, and profilin

For each of my perturbations, I sought to quantify the relative expression level compared to my wild type data. In my plastin RNAi experiments, I measured a strain that has plastin endogenously labeled with GFP. To account for varying noise levels between samples, I calculated the average background noise for each video and subtracted that from the image. I then simply calculated the average plastin intensity in the posterior region during maintenance phase. I found that the plastin intensity decreased in response to the length of time *C. elegans* were fed on RNAi plates, which matches my expectations.

In my formin RNAi experiments, I collected timelapse images of formin over the course of the 2-cell embryo stage. The signal to noise ratio for these images was much lower, so I was not able to simply calculate the formin intensity as I did for plastin. Instead, I used Kilfoil tracking software to localize, but not link, formin speckles. I used standard settings for all videos. I then plotted the number of formin speckles across time and identified the time range in which there was a plateau in the number of formin speckles (see Figure 2.7). Based on the timing of this event, I believed that this corresponded to maintenance phase in the 2-cell stage. I averaged the number of formin speckles over 50 frames in this region. I found that the average number of formin speckles detected clearly decreased based on the strength of the depletion, so I used this as a metric going forward.

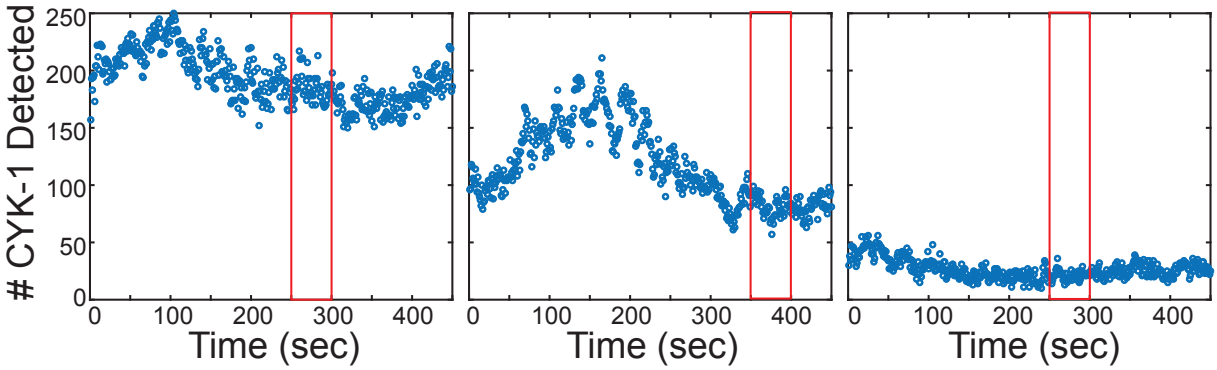

Figure 2.7: Quantifying the CYK-1 density over 2-cell development at different depletion levels. Number of CYK-1 speckles detected over time for wild type (left) and two different depletion levels (middle, right). Red box highlights 50 s window during which I calculate average number of CYK-1 speckles used to align depletion levels.

Finally, I wanted to calculate the actin elongation rate in my profilin RNAi experiments. By tracking formin, I was able to directly observe elongating actin filaments as described previously[17]. I waited 3-4 minutes after cell division and collected streaming data of formin labeled in the embryo. I then tracked the formin speckles, selected trajectories undergoing ballistic motion ($\alpha > 1.5$) and calculated the velocity of these speckles. In embryos that had a high profilin depletion level, there were many local and global network tearing events. This distorted the number of motors it appeared were undergoing ballistic motion; if a motor was bound to a filament that was undergoing a tearing event, the α was artificially high. In these cases, I hand selected as many trajectories as possible that I believed were not affected by network tearing events. I then only used these trajectories to calculate the average elongation rate. A representative example of the distribution of actin elongation rates for a single embryo is shown in Figure 2.8.

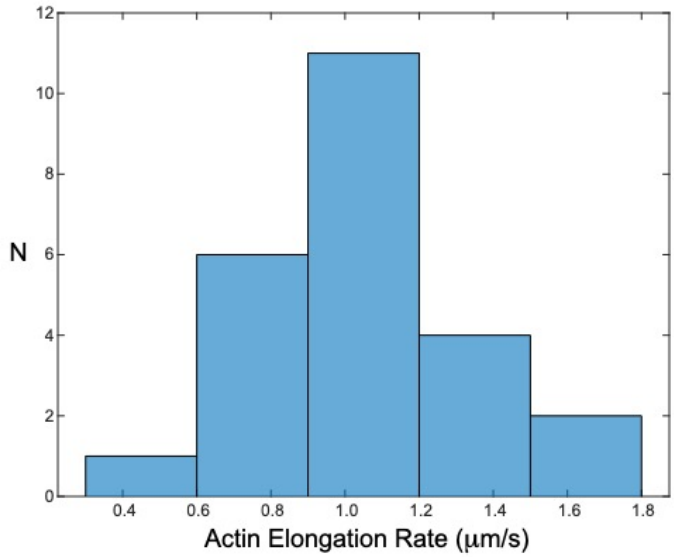

Figure 2.8: Actin elongation rate distribution from example *C. elegans* zygote. Histogram of velocities of formin undergoing ballistic motion.

Cytosim Set Up

Cytosim is an agent-based simulation suite to model cytoskeletal systems[35–37]. Filaments, crosslinkers, and motors are coarse-grained and represented as point objects that move by Langevin dynamics. On a user level, it is easy to customize Cytosim software. The GitHub repository gives detailed examples of configuration files and provides instructions on how to introduce new classes of objects such as filaments. For my simulations, I created a customized fiber class and tuned its parameters to reproduce experimentally relevant observations.

Briefly, I selected a 32 μm x 20 μm rectangular region with periodic boundaries. Actin filaments underwent periods of assembly and disassembly as determined by my custom fiber class. I enforced turnover in the system by adding and deleting crosslinker and motors throughout the simulation. Crosslinkers were added and deleted from the system at the rate of 50 s^{-1}. Myosin was added throughout the entire simulation space at the rate of 30 s^{-1} and in the center 10 μm of the system it was added at a rate 6 fold higher (180 s^{-1}). This enforced a myosin gradient that drove

cortical flows. Table 2.3 provides overview of parameter choices in my standard simulations, and Table 2.4 provides the range of perturbations I completed when altering crosslinker density, actin nucleation rate, and actin elongation rate.

Perturbation	Minimum Value	Maximum Value	Standard Value
Crosslinker Density	445	53,400	44,500
Actin Nucleation Rate	12.1 s^{-1}	181.5 s^{-1}	121 s^{-1}
Actin Elongation Rate	0.15 μm/s	2.0 μm/s	1.5 μm/s

Table 2.4: Ranges of perturbations for Cytosim simulations. Details range of parameters tested when perturbing crosslinker density, actin filament nucleation rate, and actin elongation rate.

Customizing a fiber class that undergoes periods of assembly and disassembly

In the cortex of the one-cell *C. elegans* embryo, actin filaments nucleate and undergo a period of elongation; after approximately 7-9 seconds, they disassemble from the pointed end[38]. Previously developed fiber objects are static or allow treadmilling only with assembly and dissasembbly rates that are the same, so the actin filament length stays constant. To reproduce the behavior in the cortex, I needed to add a custom fiber class. To this end, I introduced two independent "timer" variables in my fiber class. The first timer sets the time at which elongation from the plus end stops, and the second timer sets the time at which disassembly from the minus end begins. The values of both of these variables are drawn from an exponential distribution with an average time of 7.5 seconds.

Determining crosslinker binding rates to produce zippering

I used a combination of published simulations[16] and calculations to set the parameters for the crosslinkers. Based on previous reports of plastin in *C. elegans* embryos[16], the crosslinkers were

composed of identical subunits with stiffnesses of 250 pN/μm, diffusion constant of 10 $\mu m^2/s$ and binding range of 10 nm.

Previous work observed that growing actin filaments preferentially assemble along existing actin filaments[17]. I sought to find the crosslinker density and binding rates that reproduced this behavior. First, I looked at the simplest system. Namely, I created a system with one long actin filament that was undergoing treadmilling and then nucleated new actin filaments with random orientations 5 nm away from it. I could then observe if the assembling filament crosslinked to the existing filament during its lifetime. For each set of binding/unbinding rates, I observed 10-20 fibers to see how frequently zippering occurred. I found that zippering never occurred when the binding rate was below 20 s^{-1}. When the binding rate was 20 s^{-1}, zippering occurred occasionally. Increasing the binding rate to be more than 20 s^{-1} caused the frequency of zippering to increase.

Of course, my actual simulations are not idealized; actin filaments are not nucleated immediately next to existing actin filaments. So, I tested various crosslinker densities and binding rates in full simulations, with many actin filaments present. I then made videos to observe whether or not zippering occurred. I found that zippering occurred rarely when the binding rate was 20 s^{-1}. When the binding rate was 60 s^{-1}, zippering was prevalent throughout the simulations. Increasing the binding rate above 60 s^{-1} did not drastically increase how frequently I saw filaments zipper along one another. I set the binding rate of my crosslinkers to be 60 s^{-1} in my standard simulations.

Determining network density (via actin nucleation rate) to produce target bundle size distribution

Actin filaments are crosslinked together by plastin into bundles of varying sizes in the *C. elegans* cortex. I calculated the range of bundle sizes *in vivo* and wanted to reproduce this bundle size distribution in my simulations. The ability to create bundles of different sizes depends on the

overall actin density in the network. The overall actin density is controlled by the actin nucleation rate, actin elongation rate, and average filament lifetime. Since the elongation rate and lifetime were constrained by experimental measurements, I adjusted the nucleation rate to control the overall actin density in the system. The nucleation rate was determined using the following formula:

$$Nucleation\ Rate\ = \frac{n\sqrt{A}}{< L_m >< \tau >}$$

where n is the average total linear amount of actin, A is the area of the system, $\boldsymbol{\tau}$ is the average lifetime of the actin filaments, and L_m is the average maximum length, which can be re-written as:

$$L_m\ =\ Elongation\ Rate\ *\ \tau$$

I identified target actin densities (e.g. the total linear amount of actin in the system) and adjusted the nucleation rate to achieve these values. Then, I calculated the bundle size distribution for each condition. The mean bundle size and range of bundle sizes were both sensitive to the overall actin density (see Figure 2.9). I found that the nucleation rate 121 s^{-1} produced the range of bundle sizes found in simulations. Going forward, this became the standard nucleation rate used in my simulations.

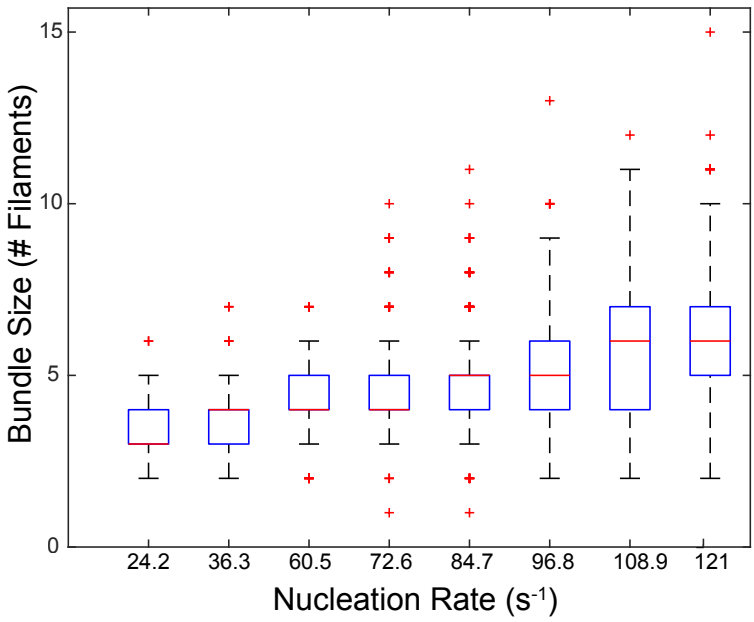

Figure 2.9: Increased actin nucleation rate leads to increase in the bundle size distribution. The bundle size distribution was quantified for a range of nucleation rates in the system. The red lines are the average bundle size, while the plus signs are the outliers.

Creating a myosin gradient to drive cortical flow

To create a myosin gradient, I initialized the system with a higher density of myosin in the center (see Figure 2.10 for general schematic of simulation). Then, throughout the simulation, I added myosin to the center of the system at a higher rate than I did at the periphery while removing it from the system without any spatial bias.

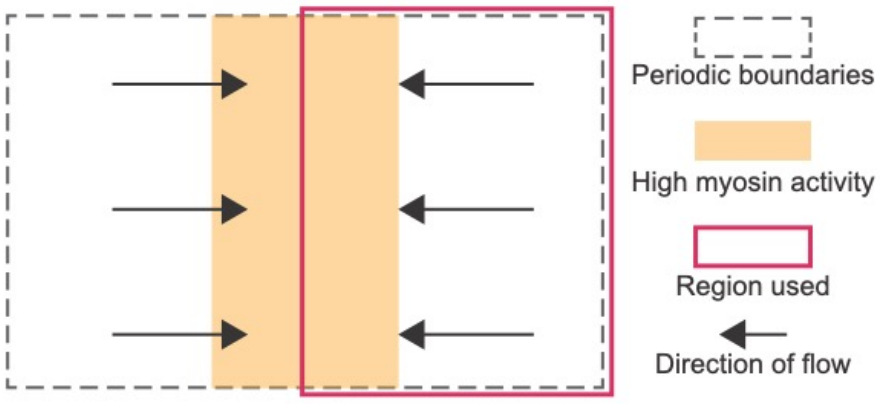

Figure 2.10: Schematic of Cytosim simulations. Figure 2.10 Continued (pg. 70)

Figure 2.10 Continued. Simulations were constructed in a 32x20 μm rectangular space with periodic boundaries on the X and Y axes. Myosin was enriched in the center 10 μm of the simulation, which produced flow towards the center of the space. Only the right half of the simulations were used in analysis.

I optimized three parameters: the base addition rate of myosin in the system, the addition rate in the center relative to the base addition rate, and the number of myosin motors in the system. I first varied the base addition rate with the addition rate in the center fixed at 10 times the base addition rate. I computed the maximum velocity (Figure 2.11A) and the myosin density in the center and at the edges of the simulation space (blue and red respectively in Figure 2.11B). Based on these results, I chose a base addition rate of 30 s^{-1} and used this going forward.

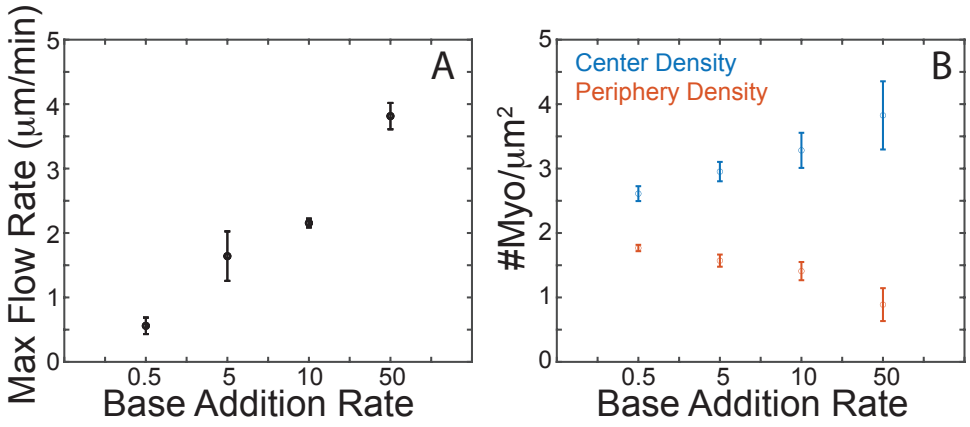

Figure 2.11: Maximum flow and myosin gradient change based on the base addition rate of myosin in the system. A: Maximum flow rate increases as base addition rate increases. B: Density of myosin in center (blue) and periphery (red) change based on activity ratio. The difference between the densities increases at higher base addition rates. Note: X axis is not linear.

Next, I varied the ratio of the center addition rate to the base addition rate. In previous simulations (not shown), I found that ratios between 2 and 10 were necessary for to observe any flow, so I tested ratios of 4-8. The changes in the maximum flow rate (Figure 2.12A) and myosin

gradient (Figure 2.12B) were subtle, but the value that was closest to experimental observations was an activity ratio of 6, so that was my final choice.

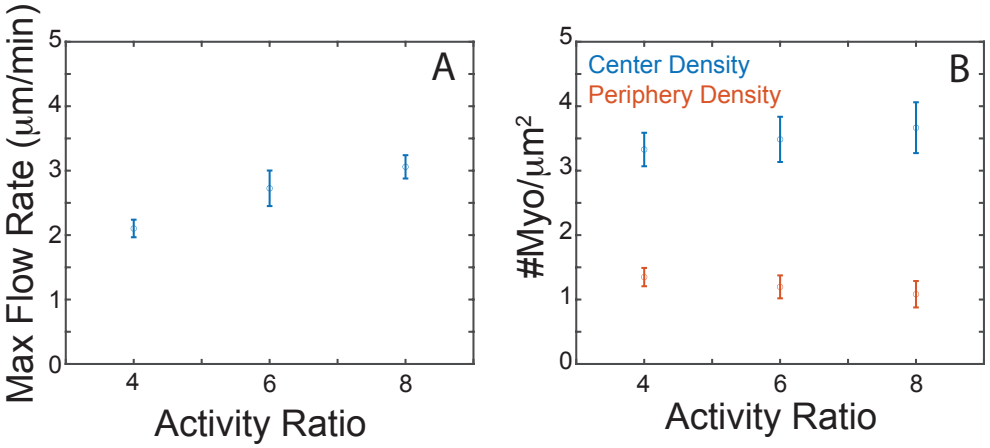

Figure 2.12: Maximum flow rate and myosin gradient undergo subtle changes in response to the activity ratio. A: maximum flow rate vs activity ratio. Maximum flow rate slightly increases at higher activity ratios. B: Density of myosin in center region (blue) and periphery (red). The difference in density slightly increases at higher activity ratios.

Finally, I tested the effect of changing the total number of myosin in the system. I found that increasing the total number of myosin increases the maximum flow rate (not shown), so I selected 1,600 myosin motors in the system because it produced the maximum flow rate closest to experimental values.

2.6 Chapter 2 References

1. Chugh, P. & Paluch, E. K. The actin cortex at a glance. *J. Cell Sci.* **131**, jcs186254 (2018).

2. Salbreux, G., Charras, G. & Paluch, E. Actin cortex mechanics and cellular morphogenesis. *Trends Cell Biol.* **22**, 536–545 (2012).

3. Lenz, M. Geometrical Origins of Contractility in Disordered Actomyosin Networks. *Phys. Rev. X* **4**, 041002 (2014).

4. Chugh, P. *et al.* Actin cortex architecture regulates cell surface tension. *Nat. Cell Biol.* **19**, 689–697 (2017).

5. Koenderink, G. H. & Paluch, E. K. Architecture shapes contractility in actomyosin networks. *Curr. Opin. Cell Biol.* **50**, 79–85 (2018).

6. Truong Quang, B. A. *et al.* Extent of myosin penetration within the actin cortex regulates cell surface mechanics. *Nat. Commun.* **12**, 6511 (2021).

7. Bray, D. & White, J. G. Cortical Flow in Animal Cells. *Science* **239**, 883–888 (1988).

8. Roubinet, C. *et al.* Spatio-temporally separated cortical flows and spindle geometry establish physical asymmetry in fly neural stem cells. *Nat. Commun.* **8**, 1383 (2017).

9. Oon, C. H. & Prehoda, K. E. Asymmetric recruitment and actin-dependent cortical flows drive the neuroblast polarity cycle. *eLife* **8**, e45815 (2019).

10. Munro, E., Nance, J. & Priess, J. R. Cortical Flows Powered by Asymmetrical Contraction Transport PAR Proteins to Establish and Maintain Anterior-Posterior Polarity in the Early C. elegans Embryo. *Dev. Cell* **7**, 413–424 (2004).

11. Hernández-Vega, A. *et al.* Polarized cortical tension drives zebrafish epiboly movements. *EMBO J.* **36**, 25–41 (2017).

12. Hird, S. N. & White, J. G. Cortical and cytoplasmic flow polarity in early embryonic cells of Caenorhabditis elegans. *J. Cell Biol.* **121**, 1343–1355 (1993).

13. Cuenca, A. A., Schetter, A., Aceto, D., Kemphues, K. & Seydoux, G. Polarization of the C. elegans zygote proceeds via distinct establishment and maintenance phases. *Development* **130**, 1255–1265 (2003).

14. Cowan, C. R. & Hyman, A. A. Acto-myosin reorganization and PAR polarity in C. elegans. *Development* **134**, 1035–1043 (2007).

15. Lang, C. F. & Munro, E. The PAR proteins: from molecular circuits to dynamic self-stabilizing cell polarity. *Development* **144**, 3405–3416 (2017).

16. Ding, W. Y. *et al.* Plastin increases cortical connectivity to facilitate robust polarization and timely cytokinesis. *J. Cell Biol.* **216**, 1371–1386 (2017).

17. Li, Y. & Munro, E. Filament-guided filament assembly provides structural memory of filament alignment during cytokinesis. *Dev. Cell* **56**, 2486-2500.e6 (2021).

18. Joanny, J.-F. & Prost, J. Active gels as a description of the actin-myosin cytoskeleton. *HFSP J.* **3**, 94–104 (2009).

19. Jülicher, F., Kruse, K., Prost, J. & Joanny, J.-F. Active behavior of the Cytoskeleton. *Phys. Rep.* **449**, 3–28 (2007).

20. Blanchoin, L., Boujemaa-Paterski, R., Sykes, C. & Plastino, J. Actin Dynamics, Architecture, and Mechanics in Cell Motility. *Physiol. Rev.* **94**, 235–263 (2014).

21. Prost, J., Jülicher, F. & Joanny, J.-F. Active gel physics. *Nat. Phys.* **11**, 111–117 (2015).

22. Mayer, M., Depken, M., Bois, J. S., Jülicher, F. & Grill, S. W. Anisotropies in cortical tension reveal the physical basis of polarizing cortical flows. *Nature* **467**, 617–621 (2010).

23. Sedzinski, J. *et al.* Polar actomyosin contractility destabilizes the position of the cytokinetic furrow. *Nature* **476**, 462–466 (2011).

24. Ding, Z., Lambrechts, A., Parepally, M. & Roy, P. Silencing profilin-1 inhibits endothelial cell proliferation, migration and cord morphogenesis. *J. Cell Sci.* **119**, 4127–4137 (2006).

25. Tinevez, J.-Y. *et al.* Role of cortical tension in bleb growth. *Proc. Natl. Acad. Sci.* **106**, 18581–18586 (2009).

26. Vicente-Manzanares, M., Ma, X., Adelstein, R. S. & Horwitz, A. R. Non-muscle myosin II takes centre stage in cell adhesion and migration. *Nat. Rev. Mol. Cell Biol.* **10**, 778–790 (2009).

27. Danuser, G. & Waterman-Storer, C. M. Quantitative fluorescent speckle microscopy of cytoskeleton dynamics. *Annu. Rev. Biophys. Biomol. Struct.* **35**, 361–387 (2006).

28. Dasanayake, N. L. & Carlsson, A. E. Stress generation by myosin minifilaments in actin bundles. *Phys. Biol.* **10**, 036006 (2013).

29. Hundt, N., Steffen, W., Pathan-Chhatbar, S., Taft, M. H. & Manstein, D. J. Load-dependent modulation of non-muscle myosin-2A function by tropomyosin 4.2. *Sci. Rep.* **6**, 20554 (2016).

30. Funk, J. *et al.* Profilin and formin constitute a pacemaker system for robust actin filament growth. *eLife* **8**, e50963 (2019).

31. Brenner, S. The genetics of Caenorhabditis elegans. *Genetics* **77**, 71–94 (1974).

32. Willis, J. H., Munro, E., Lyczak, R. & Bowerman, B. Conditional Dominant Mutations in the Caenorhabditis elegans Gene act-2 Identify Cytoplasmic and Muscle Roles for a Redundant Actin Isoform. *Mol. Biol. Cell* **17**, 1051–1064 (2006).

33. Porta-de-la-Riva, M., Fontrodona, L., Villanueva, A. & Cerón, J. Basic Caenorhabditis elegans Methods: Synchronization and Observation. *J. Vis. Exp. JoVE* 4019 (2012) doi:10.3791/4019.

34. Timmons, L., Court, D. L. & Fire, A. Ingestion of bacterially expressed dsRNAs can produce specific and potent genetic interference in Caenorhabditis elegans. *Gene* **263**, 103–112 (2001).

35. Belmonte, J. M., Leptin, M. & Nédélec, F. A theory that predicts behaviors of disordered cytoskeletal networks. *Mol. Syst. Biol.* **13**, 941 (2017).

36. Nedelec, F. & Foethke, D. Collective Langevin dynamics of flexible cytoskeletal fibers. *New J. Phys.* **9**, 427–427 (2007).

37. Popov, K., Komianos, J. & Papoian, G. A. MEDYAN: Mechanochemical Simulations of Contraction and Polarity Alignment in Actomyosin Networks. *PLOS Comput. Biol.* **12**, e1004877 (2016).

38. Li, Y. & Munro, E. Existing actin filaments orient new filament growth to provide structural memory of filament alignment during cytokinesis. *bioRxiv* 2020.04.13.039586 (2020) doi:10.1101/2020.04.13.039586.

CHAPTER 3

EXTRACELLULAR VESICLES ARE AN EMERGING SYSTEM OF INTEREST TO UNDERSTAND HOW INFORMATION IS TRANSFERRED BETWEEN CELLS

3.1 Extracellular vesicles are an important mechanism to transfer information between cells

Extracellular vesicles (EVs) are vesicles that are produced in the cell, and then exported through various mechanisms. EVs were originally thought to be cellular waste[1]. However, it was then found that EVs can travel through the body, be taken up by other cells, and even transfer information between cells[2,3].

One of the first studies that showed EVs are capable of transferring information between cells did so in the immune system. Raposo *et al.* showed that B lymphocytes collected and purified EVs and found that these EVs present antigens[4]. They then incubated T cells with labeled EVs and observed that the cells proliferated and increased secretion of interleukin-2, a cytokine signaling molecule that is common in the immune system[4]. The T cells are only incubated with EVs and do not come into contact with any B lymphocytes. Therefore, they conclude that the EVs are capable of transmitting information, although they do not suggest any mechanism. Since then, many studies have confirmed that EVs are able to transfer information between immune cells and induce different immune responses[5–8].

Studies following Raposo *et al.*'s sought to understand exactly what materials EVs transfer between cells. Valadi *et al.* explored the hypothesis that EVs are able to transfer information between cells via RNA transfer[9]. First, they verified that RNAi was present in EVs through

Western blots and by identifying radioactive ^{3}H-uracil. Through detailed analysis, they were able to verify that mRNA and miRNA are present in EVs. Next, Valadi *et al.* collected and purified EVs containing ^{3}H-uracil from mouse mast cells and then incubated non-treated cells with these labeled EVs. 24 hours later, they washed EVs from the plates and found that the cells were radioactively labeled[9]. Notably, both mouse mast cells and human mast cells expressed ^{3}H-uracil after being incubated with the mouse mast cell derived EVs. This proved that EVs transfer RNA between cells.

EVs are capable of transmitting information beyond RNA. They are also known to transfer lipids, proteins, and other signaling molecules [2,3,8,10,11]. Some of the most common materials transferred are membrane organizer, cell adhesion, and intracellular trafficking proteins[2,8]. There have also been studies into a variety of systems, determining that EVs secreted by different cells have cell-specific markers[2].

While EVs are secreted from many cell types and play a critical role in the immune system, they do not always have positive attributes in human health. There has been increased research into the role of EVs in cancer, specifically the role EVs play in metastasis. Hoshino *et al.* was the first to observe that EVs promote cancer metastasis[12]. They injected mice with tumor-derived EVs and observed that EVs travel to specific organs (such as the lungs, brain, or liver), and promote tumor growth in those regions[12]. Other groups found that EVs secreted from breast cancer cells transfer a certain miRNA. The expression of that miRNA in endothelial cells destroys cell junctions and allows tumor cells to invade and metastasize[13]. Since then, many studies have confirmed that EVs promote metastasis and tumor growth in various forms of cancer[2,8,14–16].

Another intriguing observation is that tumor-derived EVs can "educate" other cells to have a pro-metastatic phenotype[17,18]. Pro-metastatic generally describes a state in which macrophages have increased cell invasion. This can be measured directly through invasion assays, or by screening cells for markers typically associated with cell invasion[17]. Rabe *et al.* incubated bone marrow derived macrophages with tumor-derived EVs, and found that these EVs were necessary to induce a pro-metastatic phenotype[18]. Other studies have found similar results in different cell lines and from EVs derived from various tumor sources[16,17].

EVs are clearly capable of transferring information between cells. Furthermore, EVs may have a functional role in cancer metastasis. However, the exact function of EVs is less clear. EVs are incredibly heterogenous. It is possible that only a subpopulation of EVs can promote cancer metastasis, but at this point subpopulations are not clear enough to make that distinction. Classifying EV subpopulations is an ongoing challenge in the field[2,3,8,19,20].

3.2 Ambiguities in nomenclature and *in vitro* methods obfuscate definitions of EV subpopulations

So far, I have discussed "extracellular vesicles" without precisely defining the term. Extracellular vesicle is a general term that encompasses multiple types of vesicles exported from cells, including exosomes and microvesicles. Exosomes originate as intraluminal vesicles in the endosomal pathway and are transported through the cell in multivesicular bodies (MVBs)[2,3,8,10,21]. When MVBs fuse with the plasma membrane of the cell, exosomes are released. In contrast, microvesicles bud outwardly directly from the plasma membrane[2,8,11,15]. For a detailed comparison of exosomes and microvesicles, see Figure 3.1.

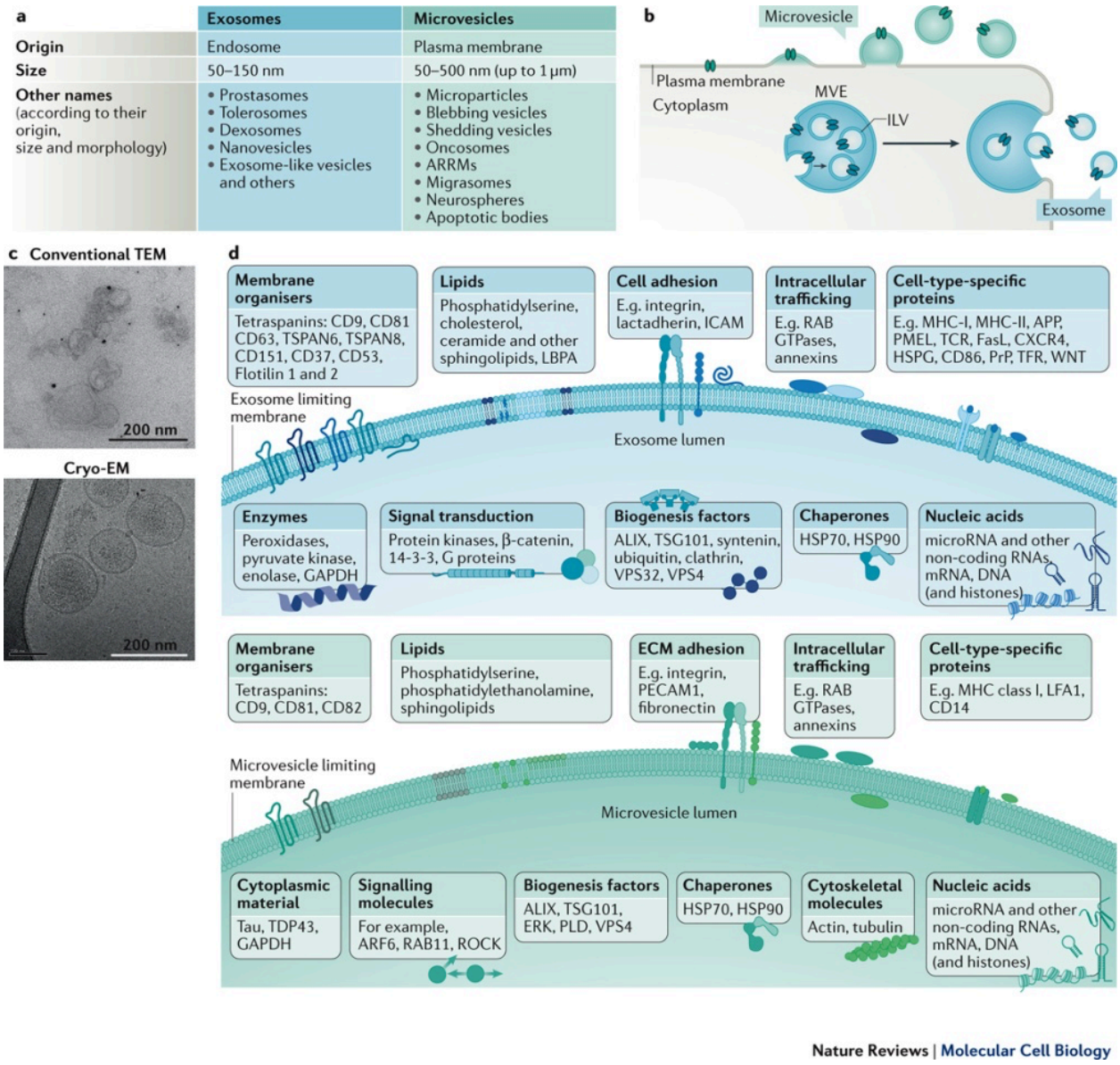

Figure 3.1: Comparison of exosomes and microvesicles. Image from Figure 1 in van Niel *et al*., 2018, "Shedding light on the cell biology of extracellular vesicles." Nat Rev Mol Cell Bio.[2]

While exosomes and microvesicles are defined based on their origin, classifying EVs as exosomes or microvesicles remains to be a challenge. It is worth noting that the challenge is partially due to inconsistencies in nomenclature in the field. EVs are an emerging system of interest, and scientists have yet to finalize the vocabulary used to describe EVs. For instance, exosomes are also referred to as protosomes, dexosomes, and nanovesicles[2,8,22,23]. Microvesicles

are also called oncosomes, migrasomes, and ectosomes[2,20,24]. The variation in terminology contributes to confusion in classifying EV subpopulations.

Classifying EV subpopulations is also a practical challenge. Most EV studies collect EVs that have already been secreted from cells, then isolate and purify them[2,4,7,9,12,17,18,25,26]. From there, EVs can be studied *in vitro*, or the EVs can be used in *in vivo* and *in situ* experiments. However, after a vesicle has been exported, there is no direct way to identify its origin. Therefore, there is no simple way to determine if a specific vesicle is an exosome or a microvesicle.

The most common way to isolate exosomes and microvesicles is through size-exclusion or ultracentrifugation. Exosomes are generally assumed to be the smallest fraction of EVs because they originate in MVBs. Using size-exclusion methods, exosomes are EVs that pass through a 200 nm filter, while microvesicles are larger vesicles. Using ultracentrifugation, exosomes and microvesicles are collected at different speeds. However, the sizes and masses of exosomes and microvesicles are heterogenous and overlapping, so this is not a clear-cut method. Furthermore, centrifugation itself can cause EVs to aggregate, which makes it even more difficult to study them independently[2,27].

It is also worth noting that the method of EV collection and purification alters the populations of EVs collected. In addition to ultracentrifugation, researchers can use density gradients or immune-affinity assays[2,27]. Density gradients have fewer problems with EV aggregation but yield fewer EVs. Immuno-affinity assays require one to use a known EV surface marker. Tauro *et al.* compared the methods and found that the morphology and protein content of EVs changed based on which method was used[27].

Since sorting based on physical characteristics is not sufficient to reliably separate exosomes and microvesicles, which are defined by their points of origin, researchers have turned

their focus to finding markers that can be used to distinguish these populations. However, many of these studies are *in vitro*, which inherently makes it impossible to determine how a vesicle originated unambiguously[19,21,26,28,29]. Most available studies report that contents of exosomes and microvesicles are heterogeneous and overlapping.

A more recent approach to finding markers for EV subpopulations is to look at EV markers *in situ*, prior to export from the cell. This would allow direct evidence of secretion pathways of the different EV markers take, which would in turn allow researchers to see if the EV markers are found in exosomes, microvesicles, or both.

3.3 Microscopy allows direct insight to EV localization and export pathways *in situ*

Various forms of microscopy have been critical in studying EVs thus far. It is possible to inject mice with labeled EVs and observe them traveling through the body[13,18,30]. Characterizing their localization also gives insight to the function of EVs. For instance, Zhou *et al.* observed that EVs that highly express a certain protein travel further throughout the body and localize in the liver, brain, and lungs. They also observed that this protein breaks down endothelial junctions. Overall, they found that EVs expressing this protein promote metastasis by increasing tumor cell invasion and weakening endothelial barriers in the host organism.

On a smaller scale, imaging cell culture *in situ* has provided valuable insights to EV function[3,24,25]. It is possible to see cells take up labeled EVs, and even specific interactions between EVs and different proteins and cellular compartments[25]. Several groups directly observed the uptake of EVs. Tian *et al*. dual labeled EVs with the lipid label DiD and protein label TAMRA-

NHS and observed that over time, the signals became spatially distant from one another[31]. This indicates that EV proteins and lipids are separated after they are taken up by cells.

While there are existing studies that visualize EV markers *in situ*, most of these studies rely on qualitative descriptions of the system rather than quantitative ones[21,31]. As described further in Chapter 1, quantifying imaging data provides more detailed information on the system. For instance, quantifying co-localization can help distinguish if two proteins are truly co-localized, or if they are found close to one another[32,33].

In Chapter 4, I investigate whether the proteins CD9 and CD63 can be used as potential biomarkers of different EV subpopulations. I used *in situ* volumetric microscopy to observe the distribution and co-localization of these two proteins with each other and other cellular components. I use various statistical methods to quantify the co-localization of these proteins.

3.4 Chapter 3 References

1. Johnstone, R. M., Adam, M., Hammond, J. R., Orr, L. & Turbide, C. Vesicle formation during reticulocyte maturation. Association of plasma membrane activities with released vesicles (exosomes). *J. Biol. Chem.* **262**, 9412–9420 (1987).

2. van Niel, G., D'Angelo, G. & Raposo, G. Shedding light on the cell biology of extracellular vesicles. *Nat. Rev. Mol. Cell Biol.* **19**, 213–228 (2018).

3. Colombo, M., Raposo, G. & Théry, C. Biogenesis, secretion, and intercellular interactions of exosomes and other extracellular vesicles. *Annu. Rev. Cell Dev. Biol.* **30**, 255–289 (2014).

4. Raposo, G. *et al.* B lymphocytes secrete antigen-presenting vesicles. *J. Exp. Med.* **183**, 1161–1172 (1996).

5. Alexander, M. *et al.* Exosome-delivered microRNAs modulate the inflammatory response to endotoxin. *Nat. Commun.* **6**, 7321 (2015).

6. Saha, B., Momen-Heravi, F., Kodys, K. & Szabo, G. MicroRNA Cargo of Extracellular Vesicles from Alcohol-exposed Monocytes Signals Naive Monocytes to Differentiate into M2 Macrophages. *J. Biol. Chem.* **291**, 149–159 (2016).

7. Wen, C. *et al.* Biological roles and potential applications of immune cell-derived extracellular vesicles. *J. Extracell. Vesicles* **6**, 1400370 (2017).

8. Yáñez-Mó, M. *et al.* Biological properties of extracellular vesicles and their physiological functions. *J. Extracell. Vesicles* **4**, 10.3402/jev.v4.27066 (2015).

9. Valadi, H. *et al.* Exosome-mediated transfer of mRNAs and microRNAs is a novel mechanism of genetic exchange between cells. *Nat. Cell Biol.* **9**, 654–659 (2007).

10. Théry, C., Zitvogel, L. & Amigorena, S. Exosomes: composition, biogenesis and function. *Nat. Rev. Immunol.* **2**, 569–579 (2002).

11. Raposo, G. & Stoorvogel, W. Extracellular vesicles: Exosomes, microvesicles, and friends. *J. Cell Biol.* **200**, 373–383 (2013).

12. Hoshino, A. *et al.* Tumour exosome integrins determine organotropic metastasis. *Nature* **527**, 329–335 (2015).

13. Zhou, W. *et al.* Cancer-secreted miR-105 destroys vascular endothelial barriers to promote metastasis. *Cancer Cell* **25**, 501–515 (2014).

14. Ozawa, P. M. M. *et al.* Extracellular vesicles from triple-negative breast cancer cells promote proliferation and drug resistance in non-tumorigenic breast cells. *Breast Cancer Res. Treat.* **172**, 713–723 (2018).

15. Tricarico, C., Clancy, J. & D'Souza-Schorey, C. Biology and Biogenesis of Shed Microvesicles. *Small GTPases* **8**, 00–00 (2016).

16. Peinado, H. *et al.* Melanoma exosomes educate bone marrow progenitor cells toward a pro-metastatic phenotype through MET. *Nat. Med.* **18**, 883–891 (2012).

17. Bs, H., A, P., N, P. & A, Z. Tumor-educated mesenchymal stem cells promote pro-metastatic phenotype. *Oncotarget* **8**, (2017).

18. Rabe, D. C. *et al.* Tumor Extracellular Vesicles Regulate Macrophage-Driven Metastasis through CCL5. *Cancers* **13**, 3459 (2021).

19. Allelein, S. *et al.* Potential and challenges of specifically isolating extracellular vesicles from heterogeneous populations. *Sci. Rep.* **11**, 11585 (2021).

20. Théry, C. *et al.* Minimal information for studies of extracellular vesicles 2018 (MISEV2018): a position statement of the International Society for Extracellular Vesicles and update of the MISEV2014 guidelines. *J. Extracell. Vesicles* **7**, (2018).

21. Bobrie, A., Colombo, M., Krumeich, S., Raposo, G. & Théry, C. Diverse subpopulations of vesicles secreted by different intracellular mechanisms are present in exosome preparations obtained by differential ultracentrifugation. *J. Extracell. Vesicles* **1**, (2012).

22. Daaboul, G. G. *et al.* Digital Detection of Exosomes by Interferometric Imaging. *Sci. Rep.* **6**, 37246 (2016).

23. Gould, S. J. & Raposo, G. As we wait: coping with an imperfect nomenclature for extracellular vesicles. *J. Extracell. Vesicles* **2**, (2013).

24. Mathieu, M., Martin-Jaular, L., Lavieu, G. & Théry, C. Specificities of secretion and uptake of exosomes and other extracellular vesicles for cell-to-cell communication. *Nat. Cell Biol.* **21**, 9–17 (2019).

25. Tian, F. *et al.* Protein analysis of extracellular vesicles to monitor and predict therapeutic response in metastatic breast cancer. *Nat. Commun.* **12**, 2536 (2021).

26. Kowal, J. *et al.* Proteomic comparison defines novel markers to characterize heterogeneous populations of extracellular vesicle subtypes. *Proc. Natl. Acad. Sci.* **113**, E968–E977 (2016).

27. Tauro, B. J. *et al.* Comparison of ultracentrifugation, density gradient separation, and immunoaffinity capture methods for isolating human colon cancer cell line LIM1863-derived exosomes. *Methods San Diego Calif* **56**, 293–304 (2012).

28. Conde-Vancells, J. *et al.* Characterization and comprehensive proteome profiling of exosomes secreted by hepatocytes. *J. Proteome Res.* **7**, 5157–5166 (2008).

29. Huang, L. *et al.* Pancreatic tumor organoids for modeling in vivo drug response and discovering clinically-actionable biomarkers. *bioRxiv* 513267 (2019) doi:10.1101/513267.

30. Kang, Y. *et al.* A multigenic program mediating breast cancer metastasis to bone. *Cancer Cell* **3**, 537–549 (2003).

31. Tian, T., Wang, Y., Wang, H., Zhu, Z. & Xiao, Z. Visualizing of the cellular uptake and intracellular trafficking of exosomes by live-cell microscopy. *J. Cell. Biochem.* **111**, 488–496 (2010).

32. Manders, E. M. M., Verbeek, F. J. & Aten, J. A. Measurement of co-localization of objects in dual-colour confocal images. *J. Microsc.* **169**, 375–382 (1993).

33. Dunn, K. W., Kamocka, M. M. & McDonald, J. H. A practical guide to evaluating colocalization in biological microscopy. *Am. J. Physiol. Cell Physiol.* **300**, C723-742 (2011).

CHAPTER 4

VOLUMETRIC MICROSCOPY OF CD9 AND CD63 REVEALS DISTINCT SUBPOPULATIONS AND NOVEL STRUCTURES OF EXTRACELLULAR VESICLES *IN SITU* IN TRIPLE NEGATIVE BREAST CANCER CELLS

This chapter is derived from the following publication:

ED White, ND Walker, H Yi, AR Dinner, NF Scherer, MR Rosner. 2022. "Volumetric microscopy of CD9 and CD63 reveals distinct subpopulations and novel structures of extracellular vesicles in situ in triple negative breast cancer cells." bioRxiv (7 November). **doi:** https://doi.org/10.1101/2022.11.08.515679.

EDW, NDW, HY, NFS, and MRR were responsible for experimental design. EDW, HY, ARD, and NFS were responsible for designing analysis. EDW collected and analyzed data and wrote the first draft of the manuscript. EDW, NDW, ARD, NFS, and MRR edited and reviewed the manuscript.

4.1 Abstract

Secreted extracellular vesicles (EVs) are now known to play multifaceted roles in biological processes such as immune responses and cancer. The two primary classes of EVs are defined in terms of their origins: exosomes are derived from the endosomal pathway while microvesicles (ectosomes) bud from the cell membrane. However, it remains unclear whether the contents, sizes, and localizations of subpopulations of EVs can be used to associate them with the two primary classes. Here, we use confocal microscopy and high-resolution volumetric imaging to study intracellular localization of the EV markers CD9 and CD63 prior to EV export from cells. We find significantly different spatial expression of CD9 and CD63. CD9 is primarily localized in microvesicles, while CD63 is detected exclusively in exosomes. We also observe structures in which CD63 forms a shell that encapsulates CD9 and interpret them to be multi-vesicular bodies.

The morphology and location within the endoplasmic reticulum of these shell-like structures are consistent with a role in differential sorting and export of exosomes and microvesicles. Our *in situ* imaging allows unambiguous identification and tracking of EVs from their points of origin to cell export, and suggest that CD9 and CD63 can be used as biomarkers to differentiate subpopulations of EVs.

4.2 Introduction

Extracellular vesicles (EVs) is a general term for vesicles that are assembled within a cell and subsequently secreted[1]. After EVs have been secreted from a cell, they are able to travel throughout the body and eventually be taken up by other cells[1–6]. EVs are involved in a variety of systems, including the immune response, cancer, and neurodegenerative diseases[2–5,7,8]. It is commonly accepted that EVs play a critical role in cancer metastasis[8–10]. We have recently shown that EVs secreted by breast cancer tumor cells are able to reprogram macrophages in the environment into pro-metastatic tumor EV-educated macrophages (TEMs)[11]. There is growing interest in using EVs in diagnostic or therapeutic approaches to different diseases[8,12,13]. However, understanding EV function is complicated by the existence of many EV subpopulations. It is theorized that EV subpopulations have distinct roles from one another[14,15]. For instance, a specific EV subpopulation could be involved in cancer metastasis. Identifying EV subpopulations would greatly advance our ability to study EV function.

Two notable types of EVs are exosomes and microvesicles. Both exosomes and microvesicles contain proteins and various forms of RNA[16,17]. Exosomes range from 50-100 nm, and microvesicles range from 50-500 nm[1]. Exosomes are formed in the endosomal pathway[18]. Late-stage endosomes become multivesicular bodies (MVBs) when inward budding occurs to form

intralumenal vesicles (ILVs) . The MVB can travel to the plasma membrane, fuse the outer membrane to the plasma membrane, and release the ILVs as exosomes[1,18–21]. In contrast, microvesicles bud directly from the plasma membrane of the cell[1,22]. Differentiating exosomes and microvesicles is difficult, partially because the size and contents of exosomes and microvesicles are heterogenous and overlapping[1,14,23].

The most common methods to study EVs are to collect EVs that have been secreted from the cell and isolate subpopulations using ultracentrifugation, density gradients, immunoaffinity assays, or some combination thereof[23,24]. EVs can then be characterized using Western blots, proteomics, or other methods. However, there are significant drawbacks to using *in vitro* methods to study EVs. First, *in vitro* methods separate EVs based on size or density, but they do not provide information on a specific vesicle's origin. Second, there are some inconsistencies in the terminology in the field, which makes it difficult to precisely define exosome and microvesicle biomarkers[25]. Third, EVs may aggregate during collection or ultracentrifugation, which obfuscates which EV markers are in different populations[14,24,25].

The transmembrane proteins CD9 and CD63 have been proposed as potential biomarkers to differentiate EV subpopulations. They are both tetraspanins, which are membrane stabilizing proteins[26]. Inhibiting Rab27a, a GTPase that is known to modulate EV secretion[7,27,28] decreases CD63 export but does not affect CD9 export[27]. This indicates that CD9 and CD63 may be associated with different EV subpopulations and could potentially be used as biomarkers to distinguish the subpopulations[26,28]. However, there is still significant debate about whether CD9 and CD63 are found in exosomes, microvesicles, or both. For instance, some researchers state that CD63 is an exosome-specific marker[12,29,30], while others state that CD63 is found in both exosomes

and microvesicles[14,24]. CD9 is widely reported to be found in both exosomes and microvesicles[10,13–15,31].

A potentially powerful approach to defining EV subpopulations more precisely is to study EVs intracellularly, prior to export. *In situ* high-resolution imaging can provide detailed information about the spatial locations of small objects, such as vesicles, which is necessary given that EVs are tens to hundreds of nanometers in diameter. Visualizing EV markers intracellularly would provide clearer insight into their origin. In 2021, Mathieu *et al.* visualized and tracked CD9 and CD63 in HeLa cells and saw that CD9 and CD63 were found in two different and one common EV populations[31]. Their work clearly demonstrates that *in situ* imaging is a powerful approach to study EV subpopulations, and that CD9 and CD63 are good candidate biomarkers for distinguishing EV subpopulations.

Volumetric imaging can provide greater insight than traditional 2-dimensional imaging into the morphology and arrangement of vesicles, such as endosomes or MVBs. In other systems, volumetric imaging has been used to reveal endosome sorting and recycling pathways that could not be visualized with 2D microscopy,[32,33] which demonstrates the advantage of understanding the 3-dimensional structure of vesicles within a cell. Furthermore, *in situ* measurements would allow analyzing the colocalization of potential EV biomarkers in a more biologically relevant context, rather than *in vitro* where the separation between vesicles may be obscured by aggregation. Therefore, high-resolution, volumetric imaging should allow gaining a deeper understanding of where EVs are localized and organized throughout individual cells.

Our work complements and builds off the findings of Mathieu *et al.,* 2021. We use high-resolution volumetric imaging to study CD9 and CD63 in triple-negative breast cancer (BM1[34]) cells. Our study reveals that CD9 and CD63 have vastly different intracellular patterns of spatial

localization and seldom colocalize, in contrast to previous *in vitro* studies that frequently report CD9 and CD63 colocalizing with one another. The spatial distribution of CD9 and its colocalization with the cell membrane suggest that CD9 is found primarily in microvesicles. CD63, on the other hand, is found only in exosomes. We substantiate this picture with detailed statistical analysis of the colocalization of CD9 and CD63 with one another and with the cell membrane. Finally, we observed 3D structures in which CD63 forms a shell that encapsulates CD9. These shell-like structures are located directly next to the endoplasmic reticulum and appear to be late-stage endosomes or early MVBs involved in EV sorting. These results suggest that CD9 and CD63 can be used to distinguish and characterize distinct subpopulations of EVs. Our work demonstrates that *in situ* imaging of EVs prior to export combined with statistical image analysis is a valuable method that offers unique insights into the subpopulations of EVs.

4.3 Results

4.3.1 In vitro Studies of Extracellular Vesicles Secreted from the Cell Show a High Degree of CD9 and CD63 Colocalization

CD9 and CD63 are often found to be colocalized when EVs are analyzed after being secreted from the cell[13,25]. To verify whether or not this occurs in EVs secreted from triple-negative breast cancer (BM1) cells, we used NanoView technology and quantified marker colocalization (Figure S4.1, see Methods for details). Using this *in vitro* measurement, we observed a high amount of colocalization of CD9 and CD63, which is consistent with other studies that use antibody-based approaches[10,13,16]. These findings for our BM1 cell line are consistent with reported observations for other cell lines.

4.3.2 Intracellular Imaging Shows that CD9 and CD63 Proteins are Spatially Distinct From One Another

We sought to determine whether CD9 and CD63 are truly colocalized intracellularly, or whether the apparent association of these markers might be an artifact of EV isolation. We used volumetric imaging via z-stacks from confocal microscopy to image BM1 cells transfected with CD9-mCherry or CD63-eGFP and observed strikingly different intracellular expression patterns for the two proteins (Supplementary Videos 4.1 (CD9), and 4. 2 (CD63)). CD9 appeared to be mainly at the cell membrane rather than the interior of the cell (Figure 4.1A). In contrast, CD63 appeared throughout the cytoplasm in two distinct forms: puncta, or small dots of various sizes, and what appeared to be small, hollow shells (Figure 4.1B). We observed CD9-containing or CD63-containing vesicles undergoing export from the cell (Figures 4.1A-B), suggesting these are secreted EVs. CD9 budding was also visualized, but the size of the bud makes it unclear whether these are large microvesicles or small apoptotic bodies (Figure S4.2). To be clear, we did not observe CD63 budding, nor did we observe vesicles with colocalized CD9 and CD63 undergoing export from the cell.

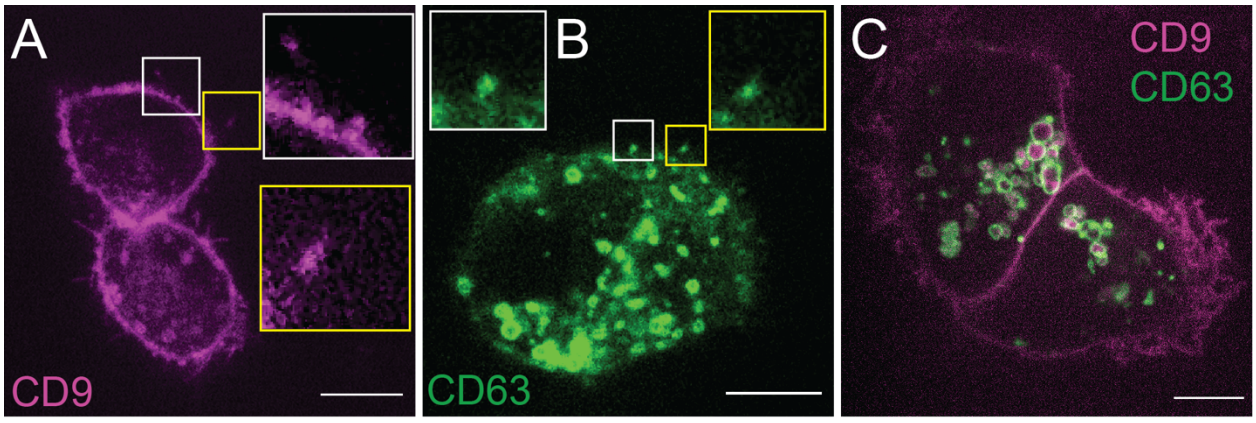

Figure 4.1. CD9 and CD63 are spatially distinct from one another. BM1 cells were transfected with 0.5 µg CD9-mCherry (left), CD63-eGFP (middle), or both CD9-mCherry and CD63-eGFP (right) and imaged 48 hours post-transfection. Left: CD9 is primarily located at the edge of the cell. Boxes and insets show CD9 EVs being exported from the cell. Figure 4.1 Continued (pg. 91)

Figure 4.1 Continued. Middle: CD63 is primarily located in the cytoplasm of the cell. Boxes and insets show CD63 EVs being exported from the cell. Right: CD9 is spatially distinct from CD63. The two proteins are rarely colocalized. Scale bars: 10 μm.

Various concentrations of DNA (0.2 μg- 2 μg) were used to transfect cells to determine if the CD9 and CD63 spatial distributions are primarily due to overexpression of the proteins. Regardless of the amount of DNA used, we observed that CD9 appeared localized primarily at the cell membrane and CD63 appeared localized primarily in the cytoplasm (Supplementary Figure 4.3). In addition, we used immunofluorescence to visualize endogenously expressed CD9 and CD63. We observed a similar trend as described above and conclude that CD9 and CD63 have distinct patterns of localization (Figure S4.4A). To determine the extent of CD9 and CD63 interaction, we transfected cells with both CD9-mCherry and CD63-eGFP (Figure 4.1c). When observing CD9 and CD63 in the same cell, it became even more clear that there was limited spatial overlap between the two proteins.

We sought to quantify the colocalization of CD9 and CD63. To do so, we used the Manders coefficient, a statistical test to determine the colocalization of two samples[35,36]. However, cells are 3D systems, and two markers may appear to be colocalized in 2D imaging if they are in the same xy location but different z locations. Therefore, we calculated the Manders coefficient of CD9 and CD63 for each z-plane in a cell (see Methods for details) (Figure 4.2). We limited this analysis to the medial z-planes of each cell (Figure 4.2D, area within black bars) to avoid artifacts associated with proximity to the top and bottom of the cell. Using this method, we calculated the percentage of the total CD9 that was colocalized with CD63, and the percentage of the total CD63 that was colocalized with CD9 for all the cells co-transfected with both proteins (Figure 4.2E-F). Although the results varied from cell to cell, our *in situ* imaging established very limited colocalization

between CD9 and CD63. Only 16% of the total CD9 population is colocalized with CD63, and only 25% of the total CD63 population is colocalized with CD9.

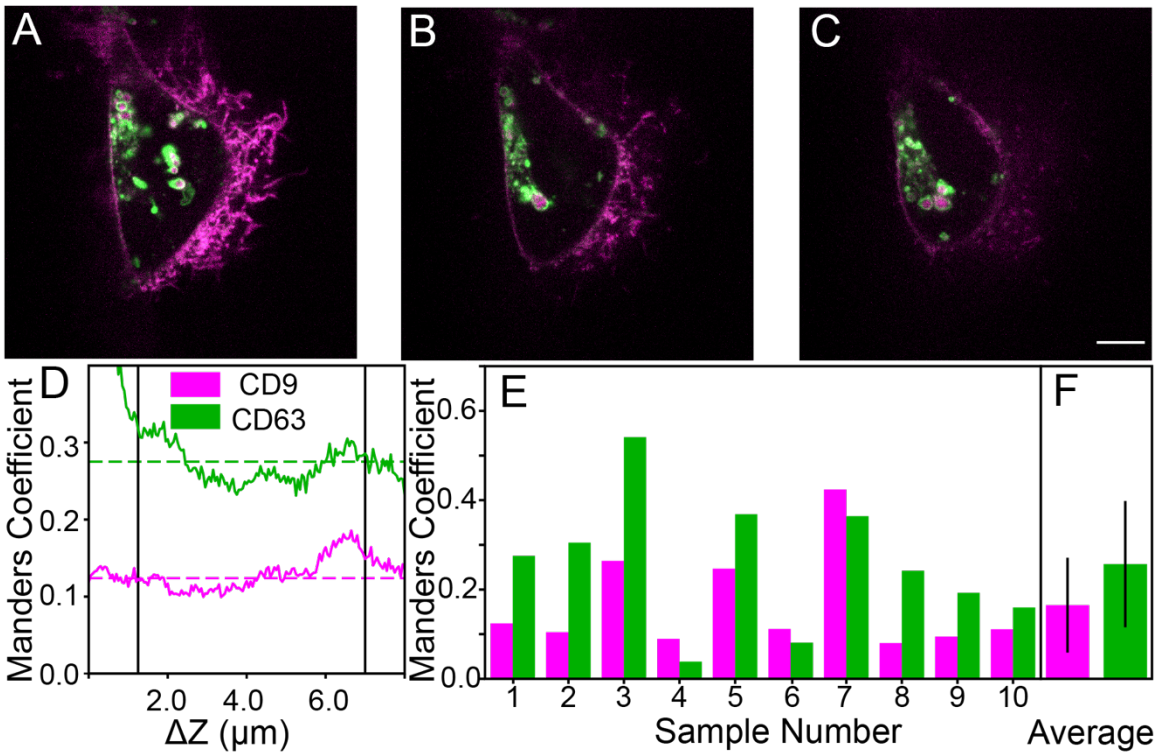

Figure 4.2. CD9 and CD63 show limited colocalization. Top: BM1 cell transfected with CD9-mCherry and CD63-GFP at (A) 1.25 μm, (B) 3.0 μm, and (C) 5.0 μm above the bottom plane of the cell. Scale bar 10 μm. The cell morphology varies, but the degree of colocalization between the proteins appears to remain limited. (D) The colocalization of the cell was calculated using the Manders coefficient for every medial z-plane (between black lines). The Manders coefficient for CD9 (magenta) and CD63 (green) does not vary significantly over the different medial z-planes of the cell (dotted green line shows average Manders coefficient for CD63, dotted pink line shows average for CD9). (E) The Manders coefficient was calculated for every cell transfected with both CD9 and CD63. (F) The average of the Manders coefficients were calculated for CD9 and CD63 (error bars are standard deviation).

To establish that the colocalization patterns were not due to overexpressing CD9 and CD63, we repeated the same analysis in cells with endogenous CD9 and CD63 immunostained with anti-CD9 and anti-CD63 antibodies (Figure S4.4B). Strikingly, we observed even less colocalization than we did with the transfected cells. Therefore, the low level of intracellular

colocalization between CD9 and CD63 was consistent regardless of whether the proteins were endogenously expressed or if the cells had been transfected with fluorescently labeled CD9 and CD63.

4.3.3 CD9 is Significantly Colocalized with the Cell Membrane while CD63 Exhibits Limited Colocalization

CD9 appeared to be primarily at the cell membrane which suggests that CD9 may be used as a marker for microvesicles. Visualization of the membrane and its potential colocalization with CD9 or CD63 would help determine if CD9 is truly colocalized with the cell membrane and if CD9 can be used as a marker for microvesicles. We thus co-transfected cells with CD9-mCherry and CD63-eGFP and stained the membrane with MemBrite 405/430 dye (Figure 4.3A). Qualitatively, we observed that CD9 was significantly colocalized with the membrane while CD63 was not. We further verified this by quantifying the colocalization of CD9 and CD63 with the cell membrane.

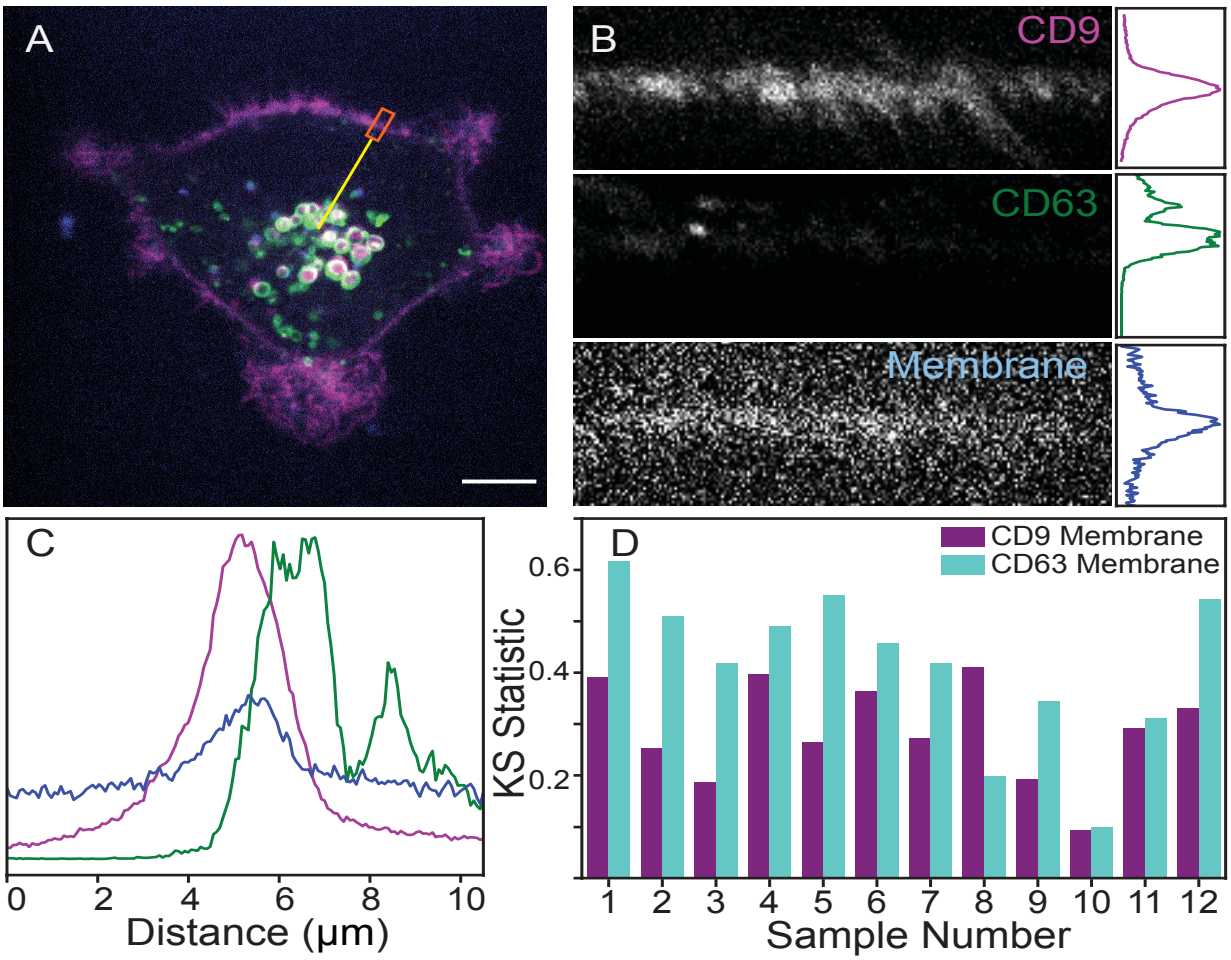

Figure 4.3. CD9 is more colocalized with the cellular membrane than CD63. (A) BM1 cell transfected with CD9-mCherry (magenta) and CD63-GFP (green), and stained with a membrane dye (blue). Scale bar: 10 μm. Radial line scans were drawn from the center of the cell to the membrane (the yellow line shows an example), and a segment of the line spanning the membrane (orange rectangle) was used to align the radial scans and study the colocalization between proteins and the membrane. (B) Radial line scans across the membrane for CD9, CD63, and the membrane (left). The intensities across all of the radial line scans were averaged (right). (C) The average intensities of the three channels from (B) superimposed. (D) The Kolmogorov-Smirnov test was calculated for regions of the membrane for 10 cells. The KS statistic for CD63 and the membrane was generally greater than the KS statistic for CD9 and the membrane, indicating that the CD9 and membrane have more similar distributions than CD63 and the membrane. Note: Larger KS statistic indicates less similar distributions.

We wanted to measure the colocalization of CD9 and CD63 with the membrane over the entire contour of the membrane. To do so, we drew radial scans from the cell centroid to the cell membrane to collect scans perpendicular to the cell membrane at every location along the

membrane contour (see yellow to white radial lines in Figure 4.3A-B, left). We centered the membrane in each line scan, so we were able to average the line scans from a given cell together to find the spatial distributions of CD9, CD63, and the cell membrane label across the membrane contour (Figure 4.3B-C). We used the Kolmogorov-Smirnov (KS) test, which is sensitive to both the location (i.e., mean value) and shape of different distributions,[37] to quantify the colocalization of CD9 and CD63 with the cell membrane for each cell. It is important to note that the KS test measures the difference between two distributions, not the similarity. When two distributions are very similar, the value of the KS coefficient is small; when two samples are very different, the KS coefficient is near 1. For every cell we studied, the KS coefficient of CD9 with the membrane was smaller than the KS coefficient of CD63 with the membrane. Since there was significant variability between cells, averaging of the KS statistics of the cell populations is less useful than applying this test to individual cells. This statistical result demonstrates that CD9 significantly colocalized with the cell membrane, in contrast to CD63, which did not.

4.3.4 CD63 Forms a Shell That Encapsulates CD9

We found a distinctive structure in which CD63 formed a shell that encapsulates CD9 in the vast majority of cells (Figure 4.4). Although the CD9 and CD63 signals appeared to be colocalized in 2D measurements, our 3D approach revealed that CD9 and CD63 were not colocalized but in close proximity. CD9 and CD63 occasionally appeared colocalized when the z-plane was at the top or bottom of the shell as a result of the finite (~800 nm) depth of the confocal slices. To verify that these shell-like structures are not an artifact of overexpression, we confirmed that the same structures are observed in endogenously-expressed protein immunostaining data (Figure S4.5).

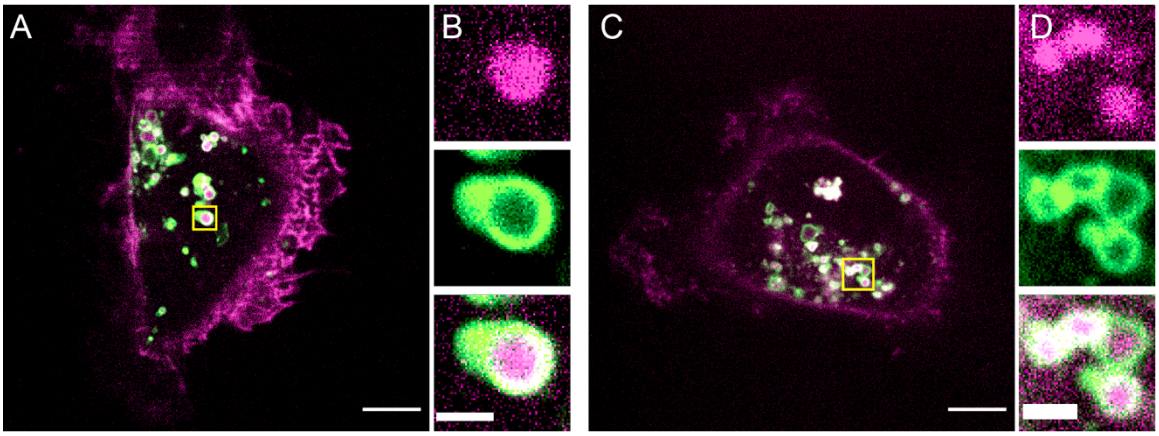

Figure 4.4. CD63 forms shell-like structures encasing CD9. (A), (C) BM1 cell transfected with CD9-mCherry and CD63-GFP. Scale bar: 10 μm. (B), (D) Expanded views of yellow boxes in (A), (C). Top: CD9, middle: CD63, bottom: composite. Scale bars: 2 μm.

4.3.5 CD63 is Contiguous with the Endoplasmic Reticulum While CD9 is Not

A possible explanation of the shell-like structures we observe is that they are multivesicular bodies (MVBs), which are late-stage endosomes that contain smaller vesicles. MVBs are formed from late endosomes near the endoplasmic reticulum (ER). When there is inward budding from the endosomal membrane, intralumenal vesicles (ILVs) are formed, thus making the late-stage endosome an MVB[18]. MVBs are a sorting mechanism in the cell; ILVs can be marked for degradation, transported to different areas of the cell, or even exported from the cell as exosomes[1,16–18,29]. We considered the possibility that the shell-like structures we observe are MVBs where CD63 is in the MVB-limiting membrane and CD9 is in ILVs within. CD63-associated EVs are known to be found in MVBs[18,38], but there have not been similar reports about CD9 localizing in MVBs.

Since late-stage endosomes and MVBs are known to frequently have contact sites with the ER[39], we sought to determine the spatial relationship with CD9, CD63, and the ER. We co-transfected cells with CD9-mCherry, CD63-eGFP, and BFP-KDEL, an ER biomarker[40] (Figure 4.5A). We observed holes or voids in the BFP-KDEL signal, and the shell-like structures were

frequently found near these holes (Figure 4.5B). The proximity of the shell-like structures to the ER suggests that they are part of the endosomal pathway. To study this further, we took line scans across the shell-like structures and ER directly adjacent to the CD63-coated shell and compared the distributions of CD9, CD63, and the ER marker (see Methods for details). The line scans shown in Figure 4.5C suggest that CD9 forms a central core that is surrounded by CD63 that in turn is surrounded by the ER.

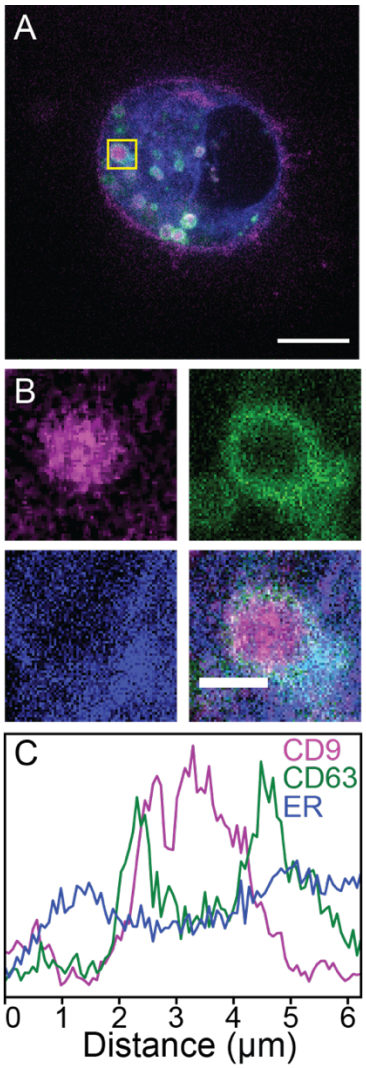

Figure 4.5. Shell-like structures are found in regions of sparse ER signal, and CD63 is in contact with the ER while CD9 is not. Figure 4.5 Continued (pg. 98).

Figure 4.5 Continued. (A) Cells were transfected with CD9-mCherry (magenta), CD63-GFP (green), and BFP-KDEL to label the ER (blue). Scale bar: 10 μm. (B) Zoom in on yellow box in (A), highlighting shell-like structures. Top left: CD9, top right: CD63, bottom left: ER, bottom right: composite. Scale bar: 2 μm. (C) Average intensities for 20 line scans through the center of the shell-like structure for CD9 (pink), CD63 (green), and ER (blue).

4.4 Discussion

CD9 and CD63 were previously reported to share a large degree of colocalization in *in vitro* studies[21,28,29]. For instance, Kowal *et al.* used antibody-coated beads to isolate EVs with different surface markers and used ultracentrifugation to identify different fractions and reported that CD9 and CD63 are found in the same fractions, albeit with varying expression levels[15]. In our own *in vitro* measurements, we observed 33-57% colocalization of CD9 and CD63. However, *in vitro* methods are not sufficiently precise to determine whether CD9 and CD63 can truly be used as biomarkers. There is a strong chance that distinctions between individual EVs, and thus EV subpopulations, is obscured due to EVs aggregating when they are collected or during centrifugation[24,25]. Additionally, *in vitro* methods cannot accurately determine an EV's origin.

To address these issues, Mathieu *et al.* recently imaged CD9 and CD63 *in situ* in HeLa cells. In that work, they observed that CD9 was localized primarily at the cell membrane and was occasionally found intracellularly[31]. In contrast, CD63 was found primarily intracellularly. They also observed that CD9 and CD63 transiently traffic through MVBs and the cell membrane[31]. They concluded that while CD9 and CD63 can be found in both exosomes and microvesicles, CD9 is primarily in microvesicles while CD63 is primarily in exosomes[31]. Our work complements and builds on Mathieu *et al*. Our studies are in triple negative breast cancer cells, so they provide information about the behavior of these markers in a second cell line. More importantly, our volumetric imaging allows us to dissect the nature of the *in situ* colocalization of CD9 and CD63.

Consistent with the findings from Mathieu *et al*., we observed that CD9 and CD63 had distinct spatial expression patterns. CD9 was primarily found at the edge of the cell, while CD63 was found primarily intracellularly. Furthermore, CD9 was highly associated with the cell membrane, while CD63 was not. This indicates that CD63 is primarily in exosomes, while CD9 is frequently found in microvesicles (Figure 4.6) in triple negative breast cancer cells, as in HeLa cells.

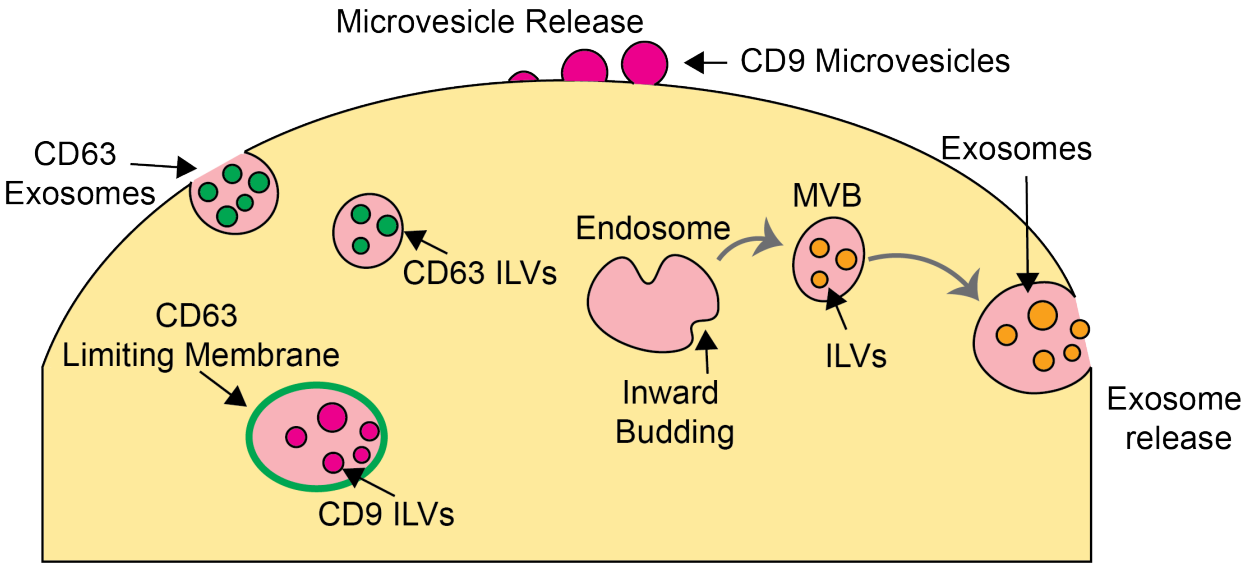

Figure 4.6. CD9 and CD63 are found in unique populations and structures. CD9 was enriched in the cell membrane and budded from the membrane, likely as microvesicles. Early endosomes stem from the Endoplasmic reticulum. When there is inward budding, interluminal vesicles (ILVs) are formed, and the overall structure is considered a late endosome or multivesicular body (MVB). When the MVB fuses with the membrane and releases the vesicles within, the released vesicles are considered exosomes. We observed puncta with CD63 in the cytoplasm, which were likely CD63-containing ILVs that are waiting to be exported as exosomes. The shell-like structures we observed were likely MVBs in which CD63 was enriched in the limiting membrane, and CD9-containing ILVs were inside the MVB. Note: CD63 and CD9 are found on the membrane of vesicles, not the interior, the coloring was chosen for clarity.

Our volumetric imaging revealed previously unobserved shell-like structures in which CD63 encapsulates CD9. In these shell-like structures, CD63 is contiguous with the ER, while

CD9 is not. Based on their structure and association with the ER, we believe these shell-like structures are MVBs in which CD63 is in the outer membrane and CD9 is in ILVs within the MVB (Figure 4.6). Notably, Mathieu *et al.* saw that CD9 and CD63 transiently colocalize in MVBs. However, they were using 2D imaging and thus did not have the ability to resolve the shell-like structures. In contrast, we can see that while CD9 and CD63 are in the same MVB, they are in different components of the structure. This indicates that they are likely trafficked differently from these shell-like structures.

Quantifying our imaging with the Manders coefficient, we conclude that there is 16-25% overlap in the CD9 and CD63 populations. This establishes statistically that CD9 and CD63 have limited colocalization. Moreover, it is important to note that the shell-like structures constitute a significant portion of the apparent colocalization between CD9 and CD63. The z-plane resolution is such that CD9 and CD63 at the tops and bottoms of the shell-like structures appear to be colocalized, when in reality they are not. Therefore, the Manders coefficient overestimates the true amount of colocalization. This makes the difference in the colocalization between the CD9 and CD63 populations that we observe *in situ* compared to reports of *in vitro* measurements[14,15,29] even more striking. Likewise, statistically comparing the spatial relationship between CD9 and CD63 with the cell membrane increased our confidence that CD9 is predominantly in microvesicles, while CD63 is not.

Observing EVs *in situ* prior to export provides key insights into distinct populations of EVs. This can be used to advance our understanding of EV origin and function. In the future, tracking EV markers in 3D over time[41], both intra- and extra-cellularly, could provide a deeper understanding of how EVs are formed and exported from the cell. Sufficiently precise tracking of

EV subpopulations could reveal differences in EV type and cargo that impact their ability to reprogram target cells, such as EVs that promote metastasis in cancer cells.

4.5 Methods

Cell Culture

MDA-MB-231 1833 (referred to as BM1) cells were obtained from Andy Minn[34], and all work was done within 18 passages of initially establishing the cells. Cells were cultured in DMEM with 10% fetal bovine serum, 50 U/ml penicillin and 50 U/ml streptomycin.

Preparation for NanoView Assay

BM1 cells were grown to 80% confluence in DMEM media with 10% fetal bovine serum, 50 U/ml penicillin and 50 U/ml streptomycin. Cells were then washed with PBS and incubated in serum-free media for 24 hours. The cell media was centrifuged at 300 g for 5 minutes to harvest the supernatant, containing EVs. The EV concentration was measured using NanoSight technology, and samples were diluted to a final concentration of 2.5e8/mL.

ExoView Tetraspanin Assay

Samples were run according to the manufacturer's instructions for the Human Tetraspanin Kit (EV-TETRA-C, NanoView Biosciences Inc.). In brief, samples were diluted 3 times in Solution A and 35 µLs were incubated on the ExoView chips overnight with capture antibodies against human CD81, CD63, and CD9. After sample incubation, chips were washed and stained for 1 hour with ExoView tetraspanin labeling antibodies that consist of (anti-CD81 CF555, anti-CD63 CF647, and anti-CD9 CF488). After staining the chips were washed, dried and imaged with the

R100 reader. NanoViewer Analysis software 2.9.1 was used to calculate the particle count and colocalization for each capture spot.

Transfection

Cells were plated at a ~2.75e5 concentration on 6 well plates 24 hours before transfection. Cells were transfected using a Lipofectamine 3000 kit following manufacturer's directions. 0.5 μg CD9-mCherry (Addgene plasmid #5013; http://n2t.net/addgene:55013; RRID:Addgene_55013) and CD63-eGFP (Addgene plasmid #62964; http://n2t.net/addgene:63964; RRID:Addgene_62964) was used unless noted otherwise. 2 μg BFP-KDEL (Addgene plasmid #49150; http://n2t.net/addgene:49150; RRID:Addgene 49150) DNA was used to label the ER. To dye the membrane, cells were incubated with the MemBrite pre-staining solution for 5 minutes at 37° C, then incubated with MemBrite Fix 405/430 (30092-T) for 5 minutes at 37° C. Cells were incubated with transfection reagents for 24 hours post transfection. They were plated on glass bottom Matek 35 mm cell sample chambers at ~50% confluence. Cells were incubated on these plates for ~24 hours. Imaging occurred ~48 hours post-transfection.

Immunofluorescence

Cells were plated on Matek 35 mm cell sample chambers at ~50% confluence 24 hours before imaging. Primary antibodies were incubated overnight with fixed and permeabilized cells at 4° C. The next morning, the cells were washed, and the secondary antibodies were added and incubated for one hour at room temperature. Antibodies used: CD9 primary: Thermo Fisher Scientific MA5-33125. CD9 secondary: Thermo Fisher Scientific A32733. CD63 conjugated primary and secondary: Thermo Fisher Scientific MA119602.

Imaging

Cells were plated on Matek 35 mm cell sample chambers at ~50% confluence 24 hours before imaging. Cells were rinsed with buffer, and then maintained in buffer through imaging at 37° C using a spinning disk confocal microscope (Nikon Ti2 inverted microscope with a Yokogawa CSU-W1 confocal scanner). EM-CCD detectors (Andor, iXon 888 Ultra) and suitable dichroic and bandpass filters (from Semrock) were used for multicolor fluorescent imaging. Sequences of images shifting the sample in the axial direction (termed Z-stacks) were taken by manually identifying the bottom and top of the cell then obtaining fluorescent images for each color channel at 50 nm intervals. An exposure time of 200 ms was used for all CD9/CD63 images. An exposure time of 400 ms was used for images with the ER marker BFP-KDEL and the membrane dye.

Manders Colocalization Analysis

This image analysis was done in Python, using the package numpy. Images were thresholded based on a manually determined cutoff and normalized so the sum of the pixel intensities was 1, making the images a probability density function rather than a matrix of fluorescence (photo-detection) counts. We then used the Manders test to compare the probability distributions. The Manders test compares the colocalization between two images (I_A, I_B)[35,36]. Two colocalization coefficients are calculated using the Manders test: M1 determines the fraction of I_A that is colocalized with I_B, and M2 determines the fraction of I_B that is colocalized with I_A.

$$M_1 = \frac{\sum I_{A_{i,coloc}}}{\sum I_{A_i}} \text{ where } I_{A_{i,coloc}} = I_{A_i} \text{ if } I_{B_i} > 0$$

$M_2 = \frac{\sum I_{Bcoloc}}{\sum I_B}$ where $I_{B_{i,coloc}} = I_{B_i}$ if $I_{A_i} > 0$

These two values allow quantifying the fraction of the total CD9 population colocalized with CD63, and the fraction of the total CD63 population colocalized with CD9. We expected these fractions to be different, making both of these quantities critical.

At the bottom of the cell (near the coverslip) and the top of the cell, the CD9 signal appeared across the entire area of the cell, which is consistent with an expression pattern we would expect if CD9 was associated with the cell membrane. This CD9 expression pattern confounded our ability to see whether CD9 and CD63 were colocalized at the top and bottom of the cell. Confocal slices have a finite depth of approximately 800 nm, so any CD63 within 800 nm of the cell surface would appear colocalized, even if the CD63 was just in close proximity. Clearly this was an artifact we wanted to avoid in our analysis. Therefore, we identified the top and bottom of the cells by identifying z-planes in which CD9 covered the entire area of the cell and excluded these z-planes from our colocalization analysis.

Membrane Line Scan Analysis and Kolmogorov-Smirnov Test

The membrane line scan analysis was performed in Python with the packages numpy and scipy. Each color channel was thresholded separately (based on a manually identified cutoff). The location of the membrane was identified, and the x and y coordinates of each point along the membrane was recorded as follows. First, the centroid of the cell was identified by hand. Drawing a line from the centroid of the cell to a point on the membrane established an azimuthal angle θ and distance $r(\theta)$ to the membrane. We drew a line segment from the cell centroid through the

point on the membrane so as to have an approximately equal distance within and beyond the cell membrane. The x and y coordinates of the points along this line were calculated as

$$r_{x,interior} = (r - n)cos(\theta) + center_x$$

$$r_{y,interior} = (r - n)sin(\theta) + center_y$$

$$r_{x,exterior} = (r + n)cos(\theta) + center_x$$

$$r_{y,exterior} = (r + n)sin(\theta) + center_y$$

We repeated this for all points along the contour of the cell membrane, giving an array of values radially traversing the membrane at a specific membrane location. We then averaged the different radial arrays together and normalized so the distribution summed to 1. This allowed producing a single distribution for the entire contour of the membrane for each channel. Normalizing the arrays allowed comparing the distributions even when the intensities of the different channels varied. To study the relationship between the different labels (CD9, CD63, and the membrane), we applied the Kolmogorov-Smirnov test for each sample. The Kolmogorov-Smirnov test compares the difference between two probability distributions[37]. The smaller the KS coefficient, the closer or more similar the distributions are. Larger values of the KS coefficient (i.e., closer to 1) mean that the distributions are more different from one another.

4.6 Supplemental Information

4.6.1 In vitro Studies of Extracellular Vesicles Secreted from the Cell Show a High Degree of CD9 and CD63 Co-localization

We used NanoView technology and quantified marker co-localization to verify whether or not EVs secreted from triple-negative breast cancer cells (BM1) have a large amount of co-localization between CD9 and CD63. NanoView captures EVs with a specific biomarker, in this case CD9, CD63, and CD81, on antibody coated chips, immunostains the EVs on each chip, and uses interferometric imaging to determine which other biomarkers (CD9, CD63, and CD81) are present on individual EVs[42–44] (Figure S4.1). This technology is able to detect individual EVs, and is specifically calibrated to detect CD9, CD63, and CD81[43]. On the chip that captured CD9, 69% of the EVs also contained CD63. Similarly, on the chip that captured CD63, ~37% of the EVs also contained CD9 (Figure S4.1).

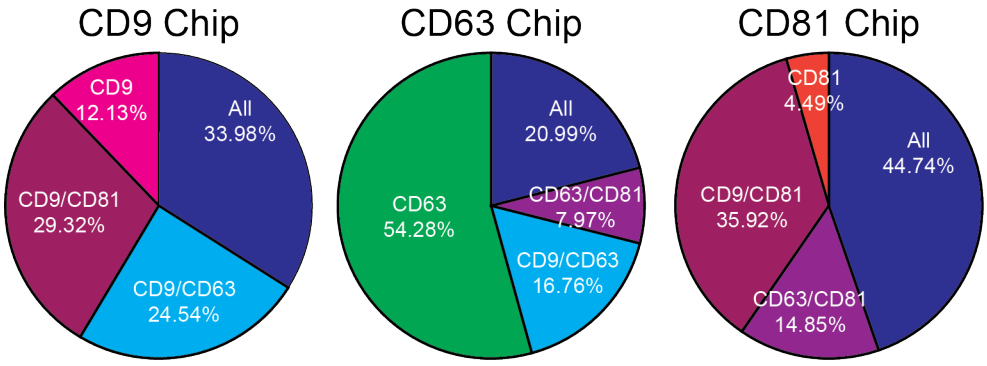

Figure S4.1. In vitro analysis of extracellular vesicles shows significant colocalization of CD9, CD63, and CD81. EVs captured by CD9 (left, N = 17,120), CD63 (middle, N = 5,694), and CD81 (right, N = 4,259) are labeled with other antibodies. Percentage of EVs containing different combinations of antibodies are calculated and shown in white text.

4.6.2 Observing Budding Extracellular Vesicles

There are multiple mechanisms through which EVs can be exported from the cell. We were able to observe the export of single CD9 and CD63 vesicles by identifying vesicles outside of, but close to, the cell membrane. However, a second mechanism of export is when vesicles bud directly from the cell membrane[1,19]. Both microvesicles and apoptotic bodies bud directly from the cell membrane; these two populations are differentiated primarily by their sizes[1]. Microvesicles are generally considered to be 100 nm -1 μm in diameter, while apoptotic bodies can be anywhere from 50 nm to 5 μm [1,19,23]. While the range of sizes are different, they do overlap.

CD63 is reported to be primarily in exosomes, which do not bud from the membrane[1,14]. Consistent with other reports, we did not find any examples of CD63 budding from the membrane. In contrast, CD9 is reported to be in microvesicles[1,19]. We found several examples of CD9 budding from the membrane, shown by vesicles forming from the membrane but not quite attached (see Figure S4.2). Since the sizes of microvesicles and apoptotic bodies are overlapping, we were unable to determine which we were observing. Nevertheless, we can confidently say that we observed CD9 budding from the cell membrane.

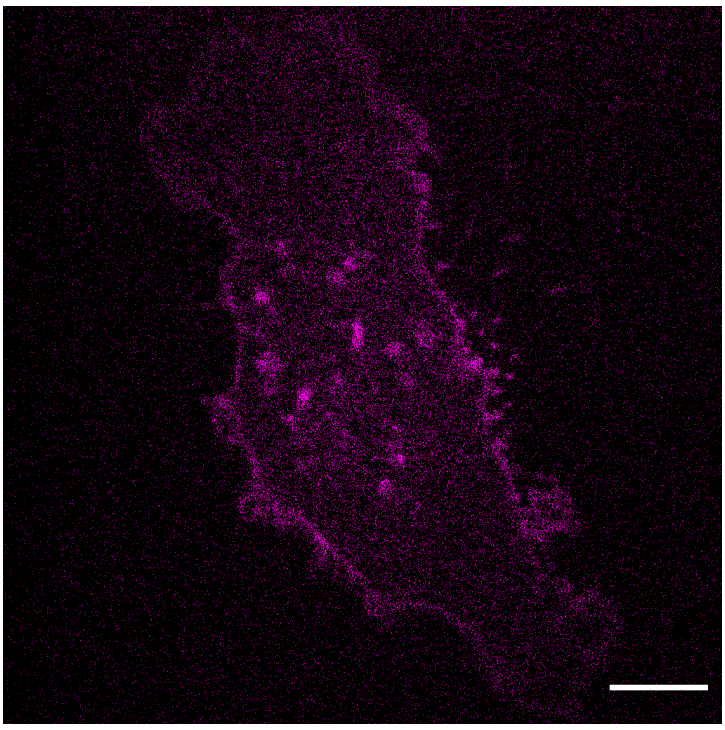

Figure S4.2. Evidence of CD9 budding. Cells were transfected with 0.5 μg CD9-mCherry DNA. White boxes indicate regions of CD9 budding. Scale bar: 10 μm.

4.6.3 Verifying the Spatial Distributions of CD9 and CD63

One concern we had while conducting our study was whether the spatial patterns of CD9 and CD63 we observed were due to the inherent overexpression of the proteins from transfection. We controlled for this concern in two ways. First, we varied the amount of DNA used to transfect the cells over an order of magnitude (0.2 μg – 2 μg). When doing this, we saw no difference in the spatial distribution of the proteins (Figure S4.3).

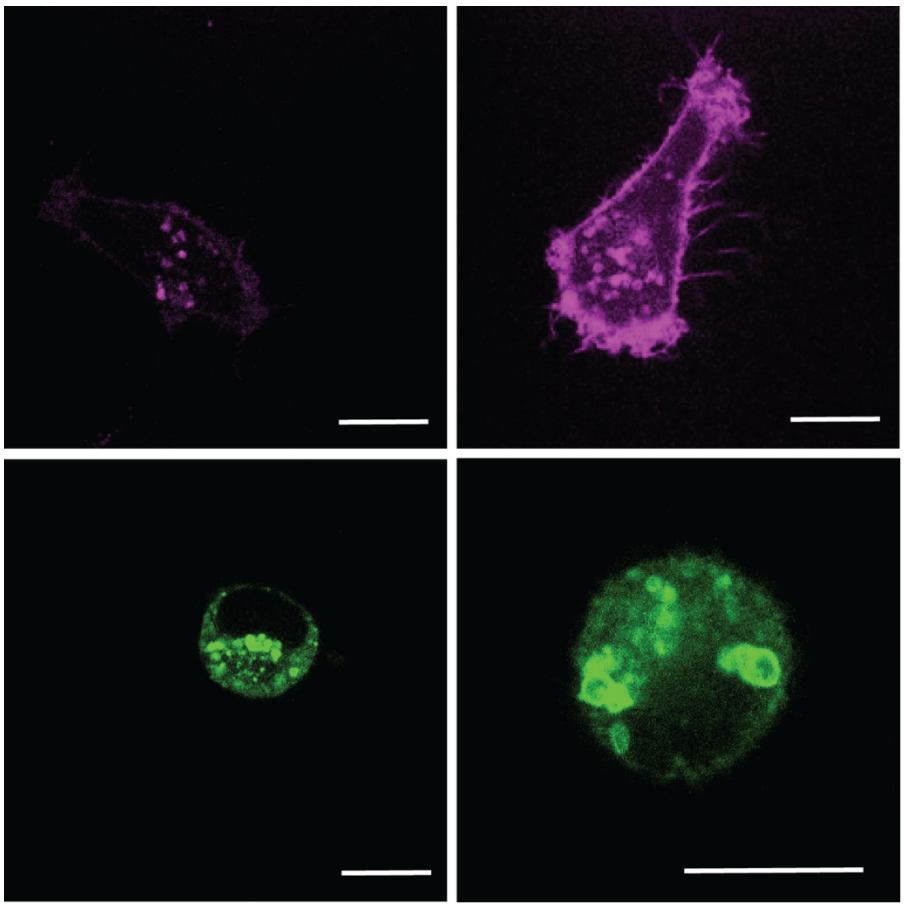

Figure S4.3. Cells transfected with different amounts of CD9-mCherry and CD63-GFP have similar spatial distributions. Top: BM1 cells transfected with 0.2 µg (left) and 2 µg (right) CD9-mCherry. Bottom: BM1 cells transfected with 0.2 µg (left) and 2 µg (right) CD63-GFP.

We immunostained CD9 and CD63 in BM1 cells to visualize the spatial distribution of the proteins at endogenous expression levels. The visual spatial distribution of the proteins matched what we observed in the transfected cells; CD9 was concentrated at the cell membrane, while CD63 was found primarily in the cytoplasm (Figure S4.4A).

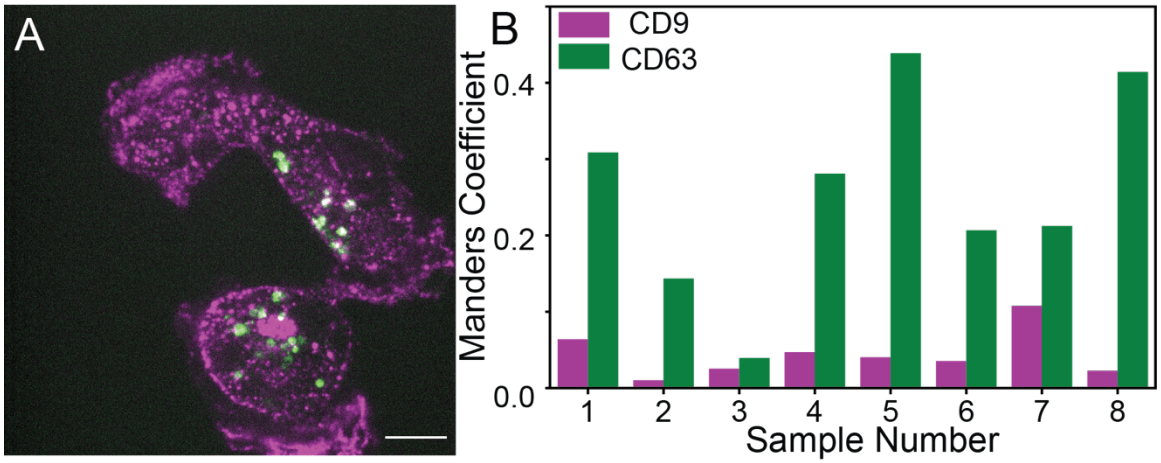

Figure S4.4 CD9 and CD63 are spatially distinct in immunostained cells. A: BM1 cells stained with CD9 (magenta) and CD63 (green) show that they two labels rarely overlap. B: Manders' coefficient for 8 samples was calculated, showing little overlap between CD9 and CD63.

In addition to visualizing the spatial distribution of immunostained cells, we quantified the co-localization of the two proteins by calculating the Manders coefficient, the same way we did in transfected cells. There was even less co-localization between CD9 and CD63 in the immunostained cells (Figure S4.4B). This confirmed that the separate spatial distribution of CD9 and CD63 was not due to overexpression of the proteins.

The last key observation we wanted to verify in cells with endogenous expression levels of CD9 and CD63 was to see whether the shell-like structures in which CD63 encapsulates CD9 we saw in transfected cells were present. We did observe these donut-like structures (Figure S4.5).

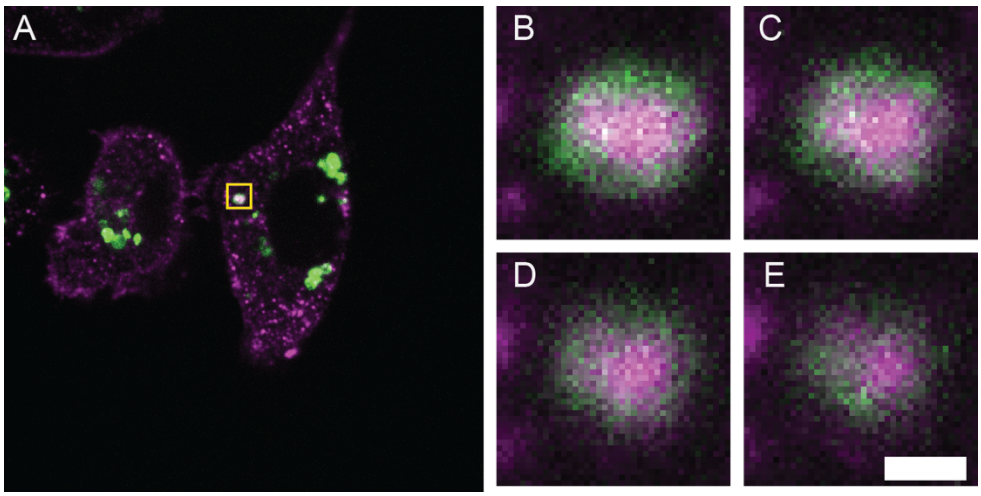

Figure S4.5. Immunostaining CD9 (magenta) and CD63 (green) reveals similar spatial distributions as transfecting CD9-mCherry and CD63-GFP. White box highlights a donut-like structures that are also observed in other cells. Scale bar: 10 µm.

Varying the transfection amounts of CD9 and CD63 and staining CD9 and CD63 to observe their endogenous expression levels, were essential controls to verify that the spatial distribution we observed was not due to over expression of the proteins. Replicating the analysis for the co-localization of CD9 and CD63 in the stained cells further reinforced that the lack of co-localization between the two proteins is accurate. Observing the same donut-like structure of CD9 and CD63 in the endogenously labeled cells also confirmed that we were not altering the spatial distribution of CD9 and CD63 when transfecting the cells.

4.7 Acknowledgements

This work was supported by NIH awards R01 CA184494 (to MRR) and R35 GM136381 (to ARD) and a Big Ideas grant from the University of Chicago (to NFS). Elizabeth White acknowledges support from the National Institute of Biomedical Imaging and Bioengineering Grant (5T32EB009412). We further thank Dr. Kristin Luther (NanoView Biosciences, Boston, MA) for helping with the NanoView experiments and analysis.

4.8 Chapter 4 References

1. van Niel, G., D'Angelo, G. & Raposo, G. Shedding light on the cell biology of extracellular vesicles. *Nat. Rev. Mol. Cell Biol.* **19**, 213–228 (2018).

2. Hoshino, A. *et al.* Tumour exosome integrins determine organotropic metastasis. *Nature* **527**, 329–335 (2015).

3. Peinado, H. *et al.* Melanoma exosomes educate bone marrow progenitor cells toward a pro-metastatic phenotype through MET. *Nat. Med.* **18**, 883–891 (2012).

4. Polanco, J. C., Li, C., Durisic, N., Sullivan, R. & Götz, J. Exosomes taken up by neurons hijack the endosomal pathway to spread to interconnected neurons. *Acta Neuropathol. Commun.* **6**, 10 (2018).

5. Saha, B., Momen-Heravi, F., Kodys, K. & Szabo, G. MicroRNA Cargo of Extracellular Vesicles from Alcohol-exposed Monocytes Signals Naive Monocytes to Differentiate into M2 Macrophages. *J. Biol. Chem.* **291**, 149–159 (2016).

6. Villarroya-Beltri, C., Baixauli, F., Gutiérrez-Vázquez, C., Sánchez-Madrid, F. & Mittelbrunn, M. Sorting it out: Regulation of exosome loading. *Semin. Cancer Biol.* **28**, 3–13 (2014).

7. Alexander, M. *et al.* Exosome-delivered microRNAs modulate the inflammatory response to endotoxin. *Nat. Commun.* **6**, 7321 (2015).

8. Wen, C. *et al.* Biological roles and potential applications of immune cell-derived extracellular vesicles. *J. Extracell. Vesicles* **6**, 1400370 (2017).

9. Ozawa, P. M. M. *et al.* Extracellular vesicles from triple-negative breast cancer cells promote proliferation and drug resistance in non-tumorigenic breast cells. *Breast Cancer Res. Treat.* **172**, 713–723 (2018).

10. Melo, S. A. *et al.* Glypican-1 identifies cancer exosomes and detects early pancreatic cancer. *Nature* **523**, 177–182 (2015).

11. Rabe, D. C. *et al.* Tumor Extracellular Vesicles Regulate Macrophage-Driven Metastasis through CCL5. *Cancers* **13**, 3459 (2021).

12. Conde-Vancells, J. *et al.* Characterization and comprehensive proteome profiling of exosomes secreted by hepatocytes. *J. Proteome Res.* **7**, 5157–5166 (2008).

13. Kavanagh, E. L. *et al.* Protein and chemotherapy profiling of extracellular vesicles harvested from therapeutic induced senescent triple negative breast cancer cells. *Oncogenesis* **6**, e388 (2017).

14. Bobrie, A., Colombo, M., Krumeich, S., Raposo, G. & Théry, C. Diverse subpopulations of vesicles secreted by different intracellular mechanisms are present in exosome preparations obtained by differential ultracentrifugation. *J. Extracell. Vesicles* **1**, (2012).

15. Kowal, J. *et al.* Proteomic comparison defines novel markers to characterize heterogeneous populations of extracellular vesicle subtypes. *Proc. Natl. Acad. Sci.* **113**, E968–E977 (2016).

16. Mathieu, M., Martin-Jaular, L., Lavieu, G. & Théry, C. Specificities of secretion and uptake of exosomes and other extracellular vesicles for cell-to-cell communication. *Nat. Cell Biol.* **21**, 9–17 (2019).

17. Garcia-Martin, R. *et al.* MicroRNA sequence codes for small extracellular vesicle release and cellular retention. *Nature* 1–6 (2021) doi:10.1038/s41586-021-04234-3.

18. Piper, R. C. & Katzmann, D. J. Biogenesis and function of multivesicular bodies. *Annu. Rev. Cell Dev. Biol.* **23**, 519–547 (2007).

19. Colombo, M., Raposo, G. & Théry, C. Biogenesis, secretion, and intercellular interactions of exosomes and other extracellular vesicles. *Annu. Rev. Cell Dev. Biol.* **30**, 255–289 (2014).

20. Clague, M. J. & Urbé, S. Multivesicular bodies. *Curr. Biol. CB* **18**, R402–R404 (2008).

21. Eden, E. R. The formation and function of ER-endosome membrane contact sites. *Biochim. Biophys. Acta* **1861**, 874–879 (2016).

22. Tricarico, C., Clancy, J. & D'Souza-Schorey, C. Biology and Biogenesis of Shed Microvesicles. *Small GTPases* **8**, 00–00 (2016).

23. Hartjes, T. A., Mytnyk, S., Jenster, G. W., van Steijn, V. & van Royen, M. E. Extracellular Vesicle Quantification and Characterization: Common Methods and Emerging Approaches. *Bioengineering* **6**, 7 (2019).

24. Tauro, B. J. *et al.* Comparison of ultracentrifugation, density gradient separation, and immunoaffinity capture methods for isolating human colon cancer cell line LIM1863-derived exosomes. *Methods San Diego Calif* **56**, 293–304 (2012).

25. Gould, S. J. & Raposo, G. As we wait: coping with an imperfect nomenclature for extracellular vesicles. *J. Extracell. Vesicles* **2**, (2013).

26. Andreu, Z. & Yáñez-Mó, M. Tetraspanins in Extracellular Vesicle Formation and Function. *Front. Immunol.* **5**, (2014).

27. Bobrie, A. *et al.* Rab27a supports exosome-dependent and -independent mechanisms that modify the tumor microenvironment and can promote tumor progression. *Cancer Res.* **72**, 4920–4930 (2012).

28. Ostrowski, M. *et al.* Rab27a and Rab27b control different steps of the exosome secretion pathway. *Nat. Cell Biol.* **12**, 19–30; sup pp 1-13 (2010).

29. Colombo, M. *et al.* Analysis of ESCRT functions in exosome biogenesis, composition and secretion highlights the heterogeneity of extracellular vesicles. *J. Cell Sci.* **126**, 5553–5565 (2013).

30. Baietti, M. F. *et al.* Syndecan-syntenin-ALIX regulates the biogenesis of exosomes. *Nat. Cell Biol.* **14**, 677–685 (2012).

31. Mathieu, M. *et al.* Specificities of exosome versus small ectosome secretion revealed by live intracellular tracking of CD63 and CD9. *Nat. Commun.* **12**, 4389 (2021).

32. Ram, S., Prabhat, P., Chao, J., Ward, E. S. & Ober, R. J. High accuracy 3D quantum dot tracking with multifocal plane microscopy for the study of fast intracellular dynamics in live cells. *Biophys. J.* **95**, 6025–6043 (2008).

33. Gan, Z., Ram, S., Ober, R. J. & Ward, E. S. Using multifocal plane microscopy to reveal novel trafficking processes in the recycling pathway. *J. Cell Sci.* **126**, 1176–1188 (2013).

34. Kang, Y. *et al.* A multigenic program mediating breast cancer metastasis to bone. *Cancer Cell* **3**, 537–549 (2003).

35. Manders, E. M. M., Verbeek, F. J. & Aten, J. A. Measurement of co-localization of objects in dual-colour confocal images. *J. Microsc.* **169**, 375–382 (1993).

36. Dunn, K. W., Kamocka, M. M. & McDonald, J. H. A practical guide to evaluating colocalization in biological microscopy. *Am. J. Physiol. Cell Physiol.* **300**, C723-742 (2011).

37. Jr, F. J. M. The Kolmogorov-Smirnov Test for Goodness of Fit. *J. Am. Stat. Assoc.* **46**, 68–78 (1951).

38. Escola, J. M. *et al.* Selective enrichment of tetraspan proteins on the internal vesicles of multivesicular endosomes and on exosomes secreted by human B-lymphocytes. *J. Biol. Chem.* **273**, 20121–20127 (1998).

39. King, C., Sengupta, P., Seo, A. Y. & Lippincott-Schwartz, J. ER membranes exhibit phase behavior at sites of organelle contact. *Proc. Natl. Acad. Sci. U. S. A.* **117**, 7225–7235 (2020).

40. Friedman, J. R. *et al.* ER tubules mark sites of mitochondrial division. *Science* **334**, 358–362 (2011).

41. Wang, X., Yi, H., Gdor, I., Hereld, M. & Scherer, N. F. Nanoscale Resolution 3D Snapshot Particle Tracking by Multifocal Microscopy. *Nano Lett.* **19**, 6781–6787 (2019).

42. Daaboul, G. G. *et al.* Digital Detection of Exosomes by Interferometric Imaging. *Sci. Rep.* **6**, 37246 (2016).

43. Daaboul, G. G. *et al.* Label-Free Optical Biosensors for Virus Detection and Characterization. *IEEE J. Sel. Top. Quantum Electron.* **18**, 1422–1433 (2012).

44. Théry, C. *et al.* Minimal information for studies of extracellular vesicles 2018 (MISEV2018): a position statement of the International Society for Extracellular Vesicles and update of the MISEV2014 guidelines. *J. Extracell. Vesicles* **7**, (2018).

CHAPTER 5

CONCLUSION AND FUTURE DIRECTIONS

5.1 Insights and Outlooks

In Chapter 2, I presented my research on how microscopic properties of the cortex affect macroscopic cortical flows in polarized *C. elegans* zygotes. I characterized actin filament assembly/disassembly dynamics, actin filament bundling behavior and bundle sizes, and the myosin gradient along the anterior/posterior axis and customized Cytosim simulations to reproduce these characteristics. These tightly constrained simulations accurately reproduced the patterns of flow observed *in vivo*, demonstrating that the microscopic properties of the cortex are sufficient to produce cortical flows. This was a significant accomplishment for several reasons. First, it demonstrates that the known microscopic details of the cortex are sufficient to explain the emergent flow. Second, it provides a way to compare simulations and experiments systematically and quantitatively. Furthermore, it provides a straightforward way to compare how different microscopic properties of the cortex affect macroscopic patterns of flow.

Once I demonstrated that our simulations accurately reproduced cortical flows, I focused on perturbing specific characteristics of the cortex in simulations and corresponding experiments. This allowed me to use my simulations to predict changes in flow patterns in response to perturbing microscopic characteristics. I altered the crosslinker density, actin nucleation rate, and actin elongation rate in simulations and quantified the effect these perturbations had on patterns of flow. I then completed corresponding perturbations in experiments and quantified the patterns of flow. My simulations predicted essential features in the patterns of flow observed in response to each perturbation. Taken together, my findings suggest that the crosslinker density, actin nucleation

rate, and actin elongation rate all affect force propagation and resistance to deformations in the cortex. Furthermore, it seems that these properties are optimized to produce a target flow rate in the cortex. There is a regime in which the cortical flows are faster but there is no tearing in the actin network, but this does not occur in wild type embryos. This suggests that there is a biological reason this flow rate occurs in the embryo. For instance, changes in cortical flows during maintenance phase can affect the distribution of essential proteins such as HMR-1, and the onset and efficiency of cytokinesis[1,2]. This can then lead to defects later in embryo development.

There are several further steps that could be taken to round out this project. A simple additional experiment would be to change the actin lifetime in simulations, and deplete cofilin, which controls actin disassembly, *in vivo*. This would complement the experiments discussed in Chapter 2 and provide additional nuance to understanding how actin turnover dynamics affect macroscopic flows.

I observed that altering the actin nucleation rate and elongation rate caused the flow to become less coherent and local velocity fluctuations, which corresponded to tearing in the actin network, to increase. Finding a way to quantify this breakdown in structure would be beneficial, both to distinguish perturbations from one another, and to compare simulations and experiments. My previous attempts to do so, such as quantifying the velocity correlation, fell short because of noise in the experimental data. One potential method to do this is to quantify the actin mesh size and how the mesh size changes over time[3]. If the mesh size was relatively constant over time, it would indicate that there were not major tearing events happening. If the mesh size changed over time, it would indicate that there was tearing events happening. This could be a suitable metric to quantify how fluctuations in the system arise in response to perturbing microscopic properties of the cortex.

My project lays the foundation for many possible future studies. One obvious question is: How easily can the framework of my simulations be adapted to model different patterns of flow that occur during *C. elegans* development? For instance, anisotropies in myosin activity cause flow during polarity establishment in one-cell embryos[4]. Chiral flows occur in the ABa and ABp cells in four-cell embryos[5]. Adjusting the patterns of myosin localization and the boundary conditions of the simulations can tune the simulations to represent different phases, and should produce different patterns of macroscopic flow. Additionally, the general approach of measuring microscopic properties of the cortex, reproducing them in simulations, and quantitatively comparing simulations and experiments could be applied to model systems other than *C. elegans*.

A separate area of research is to investigate the role that buckling of actin filaments plays in generating macroscopic flow. In preliminary simulations, I observed that decreasing the buckling of actin filaments decreases the maximum flow rate in the system. I hypothesize that the amount of buckling events, and the spatial distribution of buckling events, affect the flow rate in the system. One method to pursue this would be to use machine learning techniques, such as recurrent neural networks (RNNs), to use the pattern of buckling events to predict the macroscopic flow rate or dynamics of the system. It would be simple to use RNNs on simulations, since the orientation of actin filaments, and thus their buckling, is known. It would be more complex to use RNNS on experimental data because there is less accessible information about the microscopic details of the system, but in principle RNNs could be used on experimental data as well.

Finally, a challenging question to pursue is: What forms of microscopic contractility contribute to generating macroscopic flow? Symmetry breaking of two actin filaments is necessary to generate contractility in the cortex. Symmetry breaking can arise from buckling, pseudo-sarcomeric orientations of actin filaments, or filament sliding[6–13]. These have been observed in

simulations and *in vitro* experiments, but it is unclear whether they occur in an experimentally realistic system. Since my simulations are tightly grounded in experimental data, it would be interesting to determine what mechanisms of symmetry breaking occur in the system. It is highly likely that multiple forms of symmetry breaking occur, and it would be difficult to disentangle how each form of symmetry breaking contributes to generating flow. However, this framework of experimentally-grounded simulations provides a useful and interesting system in which to pursue this area of study.

In Chapter 4, I present my research using volumetric microscopy to image CD9 and CD63, two well-known extracellular vesicle (EV) biomarkers, in triple-negative breast cancer cells. I found that CD9 and CD63 are frequently co-localized *in vitro* after they have been exported from cells. In contrast, CD9 and CD63 have distinct spatial distributions, and have limited co-localization *in situ*. Furthermore, CD9 is highly co-localized with the cell membrane while CD63 is not. One notable finding was that I consistently observed features in which CD63 formed a shell that encapsulated CD9. These structures resemble multi-vesicular bodies (MVBs) and have not been previously reported. Overall, my findings demonstrate that volumetric imaging EV biomarkers *in situ*, prior to export from the cell, provides detailed information of EV subpopulations. Additionally, it demonstrates that CD9 and CD63 are potential biomarkers to distinguish subpopulations of EVs in triple-negative breast cancer cells.

There are several follow up experiments that could be used to enhance this project. First, similar studies could be repeated in different cell lines to determine if these findings are unique to triple-negative breast cancer cells, or common across different forms of cancer. Additionally, further investigating the structures in which CD63 encapsulates CD9 could clarify whether these structures are MVBs or not. For instance, Rabs, LAMPs, and endocytosed tracers are found in

MVBs[14]. Labeling cells with CD9, CD63, and one or more MVB markers and quantifying their colocalization could help determine if these structures are MVBs. Finally, it has been shown that the export of EVs is affected by whether the cells are grown on 2D plates or a 3D environment that mimics an extracellular matrix (such as Matrigel or collagen)[15]. Growing cells in a 3D environment and repeating the studies would help shed light on whether the extracellular environment affects the different subpopulations of the EV proteins.

My work and the work of Mathieu *et al*.[16] demonstrate the potential for microscopy to enhance research into EVs. One potential approach to pursue is to do time-lapse imaging of CD9 and CD63 to observe their intracellular transport and eventual export from the cell. Mathieu *et al*. used 2D imaging to investigate this in melanoma cells[16]. However, my work demonstrated that volumetric imaging provides a clearer picture of intracellular structures. Using imaging set ups such as multi-focal microscopy or 3D light sheet microscopy would make it possible to visualize and track CD9 and CD63 throughout the entire cell, not just a single z-plane[17,18]. This would be particularly useful for investigating the shell-like structures we observe. 3D time-lapse imaging would allow us to see whether the CD9 and CD63 signals travel together or separately; this would help determine if these structures are used to sort CD9 and CD63 separately, or package them together.

One of the broad motivations when beginning this project was to investigate if an EV's origin affects its function after it has been secreted. It is possible that exosomes (derived in the endocytic pathway) and microvesicles (which bud directly from the plasma membrane) can have distinct functions once another cell takes them up. Or, it is possible that subpopulations of EVs containing certain biomarkers have different functions. 3D imaging and tracking could provide key insights to this question. If cells were grown in the correct environment (a dense 3D

extracellular matrix or organoid structure) and imaged using 3D microscopy, it is theoretically possible to track an EV's trajectory within a cell, during export, and ideally after uptake into a neighboring cell. This could help demonstrate if an EV's origin or contents determine the EV's fate after it is taken up by a cell. For instance, if all microvesicles undergo similar sorting pathways, it would imply that an EV's origin is critical in determining its fate. In contrast, if exosomes and microvesicles containing a given protein, such as CD9, undergo similar sorting pathways, it would imply that an EV's contents are more important in determining its fate.

Throughout my thesis, I have focused on using microscopy and quantitative analysis to explore biological systems. In two very different projects, I demonstrated the power of using quantitative approaches to characterize and explore a biological system and uncovered unique insights that would not be accessible using more qualitative methods. Overall, my thesis motivates pairing experiments with quantitative analysis and simulations and provides suggestions and frameworks for others to use in future studies.

5.2 Chapter 5 References

1. Padmanabhan, A., Ong, H. T. & Zaidel-Bar, R. Non-junctional E-Cadherin Clusters Regulate the Actomyosin Cortex in the C. elegans Zygote. *Current Biology* **27**, 103–112 (2017).

2. Ding, W. Y. *et al.* Plastin increases cortical connectivity to facilitate robust polarization and timely cytokinesis. *J Cell Biol* **216**, 1371–1386 (2017).

3. Freedman, S. L., Hocky, G. M., Banerjee, S. & Dinner, A. R. Nonequilibrium phase diagrams for actomyosin networks. *Soft Matter* **14**, 7740–7747 (2018).

4. Mayer, M., Depken, M., Bois, J. S., Jülicher, F. & Grill, S. W. Anisotropies in cortical tension reveal the physical basis of polarizing cortical flows. *Nature* **467**, 617–621 (2010).

5. Pimpale, L. G., Middelkoop, T. C., Mietke, A. & Grill, S. W. Cell lineage-dependent chiral actomyosin flows drive cellular rearrangements in early Caenorhabditis elegans development. *eLife* **9**, e54930 (2020).

6. Lenz, M., Thoresen, T., Gardel, M. L. & Dinner, A. R. Contractile units in disordered actomyosin bundles arise from F-actin buckling. *Phys. Rev. Lett.* **108**, 238107 (2012).

7. Murrell, M. P. & Gardel, M. L. F-actin buckling coordinates contractility and severing in a biomimetic actomyosin cortex. *PNAS* **109**, 20820–20825 (2012).

8. Murrell, M., Oakes, P. W., Lenz, M. & Gardel, M. L. Forcing cells into shape: the mechanics of actomyosin contractility. *Nat. Rev. Mol. Cell Biol.* **16**, 486–498 (2015).

9. Stam, S. *et al.* Filament rigidity and connectivity tune the deformation modes of active biopolymer networks. *PNAS* **114**, E10037–E10045 (2017).

10. Weirich, K. L., Stam, S., Munro, E. & Gardel, M. L. Actin bundle architecture and mechanics regulate myosin II force generation. *Biophysical Journal* **120**, 1957–1970 (2021).

11. Ennomani, H. *et al.* Architecture and Connectivity Govern Actin Network Contractility. *Current Biology* **26**, 616–626 (2016).

12. Coravos, J. S. & Martin, A. C. Apical sarcomere-like actomyosin contracts nonmuscle Drosophila epithelial cells. *Dev Cell* **39**, 346–358 (2016).

13. Thoresen, T., Lenz, M. & Gardel, M. L. Reconstitution of contractile actomyosin bundles. *Biophys. J.* **100**, 2698–2705 (2011).

14. Piper, R. C. & Katzmann, D. J. Biogenesis and Function of Multivesicular Bodies. *Annu Rev Cell Dev Biol* **23**, 519–547 (2007).

15. Thippabhotla, S., Zhong, C. & He, M. 3D cell culture stimulates the secretion of in vivo like extracellular vesicles. *Sci Rep* **9**, 13012 (2019).

16. Mathieu, M. *et al.* Specificities of exosome versus small ectosome secretion revealed by live intracellular tracking of CD63 and CD9. *Nat Commun* **12**, 4389 (2021).

17. Wang, X., Yi, H., Gdor, I., Hereld, M. & Scherer, N. F. Nanoscale Resolution 3D Snapshot Particle Tracking by Multifocal Microscopy. *Nano Lett.* **19**, 6781–6787 (2019).

18. Gagliano, G., Nelson, T., Saliba, N., Vargas-Hernández, S. & Gustavsson, A.-K. Light Sheet Illumination for 3D Single-Molecule Super-Resolution Imaging of Neuronal Synapses. *Frontiers in Synaptic Neuroscience* **13**, (2021).

APPENDIX ADDITIONAL METHODS

A.1 Cytosim Simulations

Cytosim is a simulation suite designed by Francois Nedelec's group designed to simulate cytoskeletal dynamics. The Cytosim GitHub has many tutorials and examples of previous simulations. Furthermore, it is simple to customize Cytosim simulations and the GitHub provides resources and suggestions for how to do so. In this section, I lay out how I have used Cytosim in my thesis. I detail general practices for writing a configuration file, how to add a customized fiber class, preparing Cytosim to be used on midway, and running Cytosim simulations from midway. Table A1.1 contains a list of helpful links and resources for specific tasks.

Site	Link
Cytosim Basics	https://gitlab.com/f-nedelec/cytosim
Configuration File Introduction	https://gitlab.com/f-nedelec/cytosim/-/blob/master/doc/sim/config.md
Cytosim Report Function	https://gitlab.com/f-nedelec/cytosim/-/blob/master/doc/sim/report.md
Cytosim Parameter Scans	https://gitlab.com/f-nedelec/cytosim/-/blob/master/doc/tutorials/tuto_scans.md
Singularity Instillation	https://docs.sylabs.io/guides/3.0/user-guide/installation.html
Building a Container with Singularity	https://docs.sylabs.io/guides/3.0/user-guide/build_a_container.html

Table A1: Useful links and resources for using Cytosim. This includes resources for Cytosim directly, as well as resources for how to adapt Cytosim to be used on midway.

This code is available in my GitHub repository at: https://github.com/eldwhite/Cytosim-Customizations.git. Throughout this section, I will reference example files in this repository.

A.1.1 Configuration File

The configuration file defines the system space, components of the system, any events that occur in the system, and define how the simulations runs. For the Cytosim GitHub documentation, see Table A1, "Configuration File Introduction." In my GitHub repository, the file "config.cym" is an example configuration file. It is commented to differentiate the three steps described below.

Step 1: Define the system and its components.

In this section, the function "set" defines characteristics of the space itself, and the components within the space. For instance, the command "set simul system" can define the time step, viscosity, and temperature of the system. The properties of all components in the system (fibers, crosslinkers, motors) must be defined in this section.

Step 2: Add components and initialize the system

In this section, components are added to the system and the system is initialized. The function "new" adds a certain number of a given component to the system. To initialize the system, use the functions "run" and then specify a given number of timesteps to allow the system to run. In my simulations, I first add actin filaments that appear at a given rate and allow the system to initialize for 25 seconds to allow the network to reach the desired density. Next, I add crosslinkers and motors to the system and allow them to bind and unbind while the actin is held constant for five seconds. This method was used in example configuration files in Belmonte *et al.,* 2017[1].

Step 3: Run the simulation and report outputs

Once the simulation is initialized, it is time to run the simulation and record outputs of interest. As stated above, the function "run" will run the system for a given number of time steps. The function "report" will write specific output files. In general, I run a simulation for 1000 steps (1 second), then write the output files once per second. I then repeat that command for the number of seconds needed (generally 60 seconds for my simulations).

A.1.2 Scanning Parameters Using Configuration Files

There are many ways to systematically vary parameters in configuration files. My preference is to create a config.cym.tpl file that contains arrays of the parameter values I'm interested in sampling. I can then use the following commands:

```
python/run/preconfig.cym config.cym.tpl
python/collect/run%04i/config.cym config????.cym
```

The first will create files with these different parameters, and the second command will sort each configuration file into its on folder. In general, each configuration file should be in its own folder.

A.1.3 Adding Custom Fiber Class

It is relatively straightforward to add a custom object to Cytosim. In the "Frequently Asked Questions/Advanced Topics" page on the GitHub, they have an example questions "Is it possible to make a capping protein that attached to the plus end and halt polymerization of fibers?" This question lays out how to add a custom "Actor" class with a different function. Here, I explain how to add a custom fiber class using the same principles.

To create a custom fiber class, four files must be created: **new_fiber.h**, **new_fiber.cc**, **new_fiber_prop.h**, and **new_fiber_prop.cc**. These files should be in the *cytosim/src/sim/fibers* folder. The simplest method to do so is to copy the corresponding basic 'fiber' files and modify them as desired. In addition, the files **fiber_set.cc** and **makefile.inc** must be modified so they correctly reference the custom fiber class. These two files should be in the *cytosim/src/sim* folder.

See my GitHub repository for the files I used to create my custom fiber class used in Chapter 2, named "my_treadmilling_fiber." It contains the four files needed to define the new fiber, and the altered "fiber_set" and "makefile" files used to add the fiber to Cytosim.

A.1.4 Using Singularity to Package Cytosim

Cytosim requires a set of dependencies and must be compiled on a computer system before use. Setting the dependencies and compiling Cytosim for every session on midway is complicated and leads to many errors. Instead, the best approach is to use Singularity to build a container that holds Cytosim already compiled. Singularity provides full control over the environment; users can package software and libraries and compile systems such as Cytosim. Furthermore, a Singularity container can be used on any computer or device to ensure there are no differences when using Cytosim on different systems. RCC occasionally offers workshops on Singularity and can be a helpful resource when attempting to use Singularity.

To build a Singularity container, write a ".def" file which sets which packages are installed and compiled. Next, use Singularity to build a ".sif" file which is the actual container. In my GitHub repository, "cytosim.def" is an example definition file that builds a Singularity container with Cytosim compiled within it. There are several basic sections. In the "Files" section, the files (in this case files for my custom fiber class) are defined and moved into the root directory. In the

'Runscript' section, the basic operating system is defined, and the necessary packages are installed. See Table A1.2 for a list of the dependencies necessary to compile Cytosim. Next, Cytosim is cloned from the GitHub and the custom files are moved to their correct folders. Finally, the "make" command is used to compile Cytosim. "SINGULARITY_README.txt" explains how to build a container using this file.

Building the container must be done on a local computer, it cannot be done on midway. Once the container is built, it can be transferred to midway and run Cytosim through this container. In general, I keep a folder called "cytosim_image" that contains the ".def" file, ".sif" file, my files for my custom fiber class, and a READ ME file for ease. I maintain a copy of this on midway and my local computer so the versions of Cytosim are consistent.

wget
git
make
sudo
vim
make g++
zlib1g-dev
libblas-dev
liblapack-dev
libglew-dev
build-essential
manpages-dev
libpng-dev
xauth
libglu1-mesa-dev
mesa-common-dev
libgl1-mesa-dev
libgles1-mesa-dev

Table A2: Packages required to install Cytosim.

A.1.5 Running Cytosim Simulations on Midway

Runing simulations on midway via Singularity is quite simple. For best practices, each configuration file should be in its own folder. The outputs of the simulation will be saved in this same folder. To run simulations on midway, use the following command:

```
singularity exec /directory/cytosim.sif  /home/cytosim/bin/sim config.cym
```

To monitor the simulations while they are in progress, simply read the output files. The output for fiber_lengths is one of the simplest (and shortest) files, making it the easiest to monitor.

A.2 Using Quantitative Fluorescent Speckle Microscopy

Quantitative Fluorescent Speckle Microscopy (QFSM) is a software package developed by the Danuser lab. A detailed description of the algorithm is described in Ponti *et al*., 2003[2]. Mendoza *et al.,* 2012 provides detailed methods on how they used QFSM to quantify actin dynamics[3]. It includes a detailed section on how to use QFSM, including how to prepare images for analysis, the QFSM user interface, and a detailed description of all possible parameters, ranges, and suggestions for how to select ideal parameters. Since this paper describes QFSM in such detail, I will not repeat doing so here. Instead, I will explain some unique features and suggestions for processing data.

A.2.1 General Notes on Using QFSM

Very briefly, there are several key steps to using QFSM. Using the function movieSelector.GUI, files are uploaded by selecting the directory that contains all the image files, defining key parameters on image collection (such as the frame rate, pixel size, etc.), and selecting an output

folder. Then, QFSM prompts the following functions: Noise Model Calibration, Thresholding, Mask Refinement, Speckle Detection, and Flow Tracking. There are other functions available, but these five were the only ones I used.

In Noise Model Calibration, there is a prompt to "Select Region of Interest for Cropping." This region of interest should be an area of the image that does not have any signal from the data. For instance, I always chose a corner of the image in which the *C. elegans* zygote was not present. Running the Noise Model Calibration will output the Gaussian Ratio. This value will be between 1 and 3. In general, videos that have a Gaussian Ratio below 2 should not be used; the signal to noise ratio is not sufficiently high for QFSM to function properly. If the Gaussian Ratio is above 2, the signal to noise ratio is sufficient to be used. In general, I only considered videos in which this value was above 2.4.

It is important to note that the region of interest is very important for defining the Gaussian Ratio. This region must be sufficiently large for the background noise to be calculated. However, I have found that using very large areas can cause the Gaussian Ratio to increase. Additionally, this value is very sensitive to signal. It is critical to find an area of the video in which there is no signal from the actual data; I found that selecting an area close to the embryo could raise the Gaussian Ratio.

In the Flow Tracking step, the "template range" is defined. This corresponds to a minimum and maximum template size, or region in which to search for displacement of speckles between frames. If the data is spatially homogenous, the template size can be low[3]. For my data, I used a slightly higher template size to account for heterogeneity in sample density. While it is theoretically possible to set a range of template sizes to use, it is not practical. It drastically increases how long the algorithm will take to run, to the extent that I did not find it feasible.

A.1.2 Processing flow data from QFSM

Code and data used to process and analyze outputs from QFSM can be found at: https://github.com/eldwhite/PIV-Analysis.git

Running "Flow Tracking" will produce files flowN.mat, in which N corresponds to the frame number. The structure of these output files is not typical for PIV data. It is a 4xN matrix in which N corresponds to the number of speckles for which the displacement was calculated. The columns of the matrix correspond to: X Position of arrow base, Y Position of arrow base, X position of arrow head, Y position of arrow head.

Functionally, I find it simplest to transfer this to a matrix with the following information: X Position of arrow base, Y position of arrow base, X displacement, Y displacement, and frame. An example of how to do so is in the GitHub repository, under "convertQFSMData.mat". Other files in this repository show different methods of analyzing data once it has been converted to this format.

A.3 Appendix References

1. Belmonte, J. M., Leptin, M. & Nédélec, F. A theory that predicts behaviors of disordered cytoskeletal networks. *Molecular Systems Biology* **13**, 941 (2017).

2. Ponti, A., Vallotton, P., Salmon, W. C., Waterman-Storer, C. M. & Danuser, G. Computational Analysis of F-Actin Turnover in Cortical Actin Meshworks Using Fluorescent Speckle Microscopy. *Biophys J* **84**, 3336–3352 (2003).

3. Mendoza, M. C., Besson, S. & Danuser, G. Quantitative Fluorescent Speckle Microscopy (QFSM) to Measure Actin Dynamics. *Curr Protoc Cytom* **0 2**, Unit2.18 (2012).